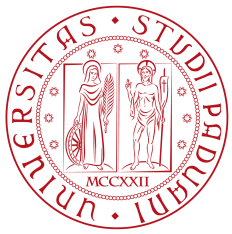

Università degli Studi di Padova

Dipartimento di Ingegneria Industriale

Corso di Laurea Magistrale in Ingegneria dell'energia elettrica

Development of a RFP conceptual reactor based on Single Helical Axis state equilibria

Sviluppo di un reattore RFP concettuale basato su equilibri Single Helical Axis

Relatore

Prof. Paolo Bettini

Università di Padova

Correlatore

Roberto Cavazzana

Consorzio RFX

Studente

Riccardo Casagrande

A mia nonna.

Abstract

The continuous growth of the worldwide demand for energy, combined with the depleting supplies of fossil fuels and the threat to the climate, has led the research to focus on alternative energy sources, over the last decades. A significant branch of this research is represented by controlled thermonuclear fusion and its leader experiment, the International Thermonuclear Experimental Reactor (ITER). ITER is based on the tokamak magnetic configuration, the best performing one in terms of energy confinement, at present. However, alternative configurations such Reversed Field Pinch (RFP) or Stellarator are actively studied, with a view to developing second generation fusion reactors, in the long term, and fusion-fission hybrid (FFH) reactors in the short to mid-term.

This thesis work aims at the development of a RFP machine able to reach the single-helicity condition, as a basis for a RFP neutron source. The study is carried out considering a modification of the largest reversed field pinch device presently in operation, the Reversed Field eXperiment (RFX-mod), situated in Padova.

Sommario

Il continuo aumento della domanda mondiale di energia, assieme alla riduzione della disponibilità di combustibili fossili e la minaccia climatica, ha portato la ricerca a focalizzarsi su fonti alternative di energia, negli ultimi decenni. Un importante ramo di questa ricerca è costituito dalla fusione termonucleare controllata e l'esperimento di punta che la rappresenta, ITER, basato sulla configurazione tokamak. Attualmente, la configurazione tokamak garantisce le migliori prestazioni in termini di confinamento energetico. Tuttavia, configurazioni alternative come RFP o Stellarator vengono studiate attivamente, nell'ottica di sviluppare reattori da fusione di seconda generazione, nel lungo termine, e reattori ibridi nel breve-medio termine.

Il lavoro svolto in questa tesi punta allo sviluppo di una macchina RFP capace di raggiungere le condizioni di singola elicità, come base per una sorgente RFP di neutroni. Lo studio è sviluppato considerando la modifica del più grande esperimento RFP attualmente operativo, il Reversed Field eXperiment (RFX-mod), situato a Padova.

Contents

Listing of figures

Listing of tables

1 Introduction

Fusion research has now been going on for over 50 years, leading to the development of several configurations for magnetic confinement machines. Experiments carried out with the different configurations ensured the achievement of a deep understanding of the plasma physics necessary to obtain thermonuclear fusion conditions. The most investigated magnetic configurations for confinement of fusion-relevant plasmas are the Tokamak, the Stellarator and the Reversed-field Pinch (fig. 1.1).

Some of the experimental tokamaks currently in operation are:

- Joint European Torus (JET), the largest operational tokamak and the baseline for ITER
- JT-60, which reached the highest value of fusion triple product
- ASDEX, the first tokamak with a x-point configuration
- Tore Supra, the record holder for plasma discharge duration
- DIII-D, which pioneered the active control for plasma MHD instabilities and the heating through neutral beam injection

The experimental results, combined with the development of theoretical aspects of plasma physics, has resulted in an international collaboration that aims to realize a magnetic fusion device that has been designed to prove the feasibility of fusion as a large-scale and carbon-free source of energy, the International Thermonuclear Experimental Reactor (ITER).

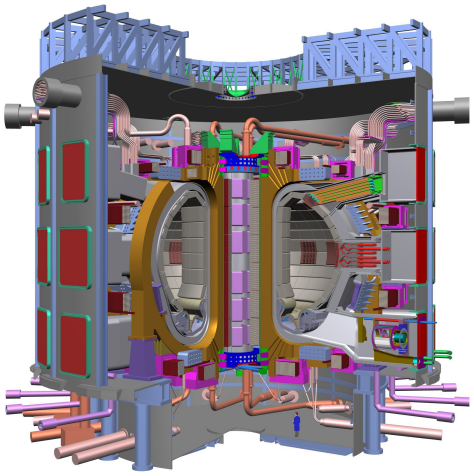

(a) Tokamak

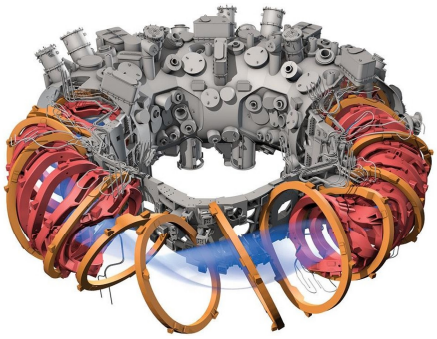

(b) Stellarator

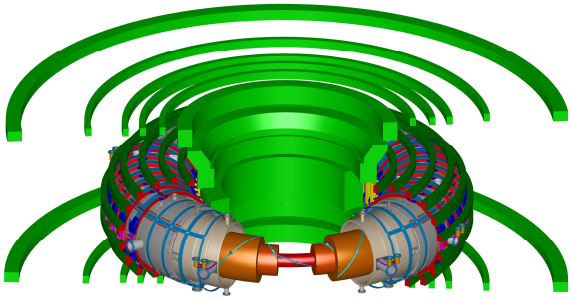

(c) RFP

Figure 1.1: Magnetic configurations for confinement of fusion-relevant plasmas

As already said, other magnetic configurations are still actively researched, to achieve a better understanding of plasma physics at various operating conditions, which can lead to the development of alternative reactors with an improved plasma confinement state, with respect to the tokamak configuration. Alternative researches are mainly based on Stellarator configurations, as Wendelstein 7-X built in Greifswald, Germany, or Reversed-field Pinch configurations, such as RFX-mod built in Padova, Italy.

In this thesis, the Reversed-field Pinch configuration will be considered to carry out a basic design of RFP reactors, based on the theoretical prediction that the RFP could exist in the chaos-free single-helicity condition (SHAx state), thus defining a possible baseline for future FFH or fusion reactors. The main feature of the RFP configuration is the potential capability

to achieve fusion conditions with ohmic heating only, hence reducing the size of the reactor, if any; in past, this feature was overcome by the saturation of MHD instabilities, resulting in poor confinement properties, with respect to the other configurations. This chaotic state, named multiple-helicity state, can evolve to a self-organised helical equilibrium called Single-helical axis state, characterised by a single (SHAx) or at least dominant (QSH) resonant mode. This, as already said, leads to a significant increase in confinement properties by removing, in fact, the mentioned drawbacks.

Eadem mutata resurgo.

Jakob Bernoulli

2

Single Helical Axis state

2.1 Reversed Field Pinch configuration

The principle of magnetic confinement in toroidal devices, is based on the gyro motion of charged particles around magnetic field lines (fig 2.1). Plasma magnetic confinement devel-

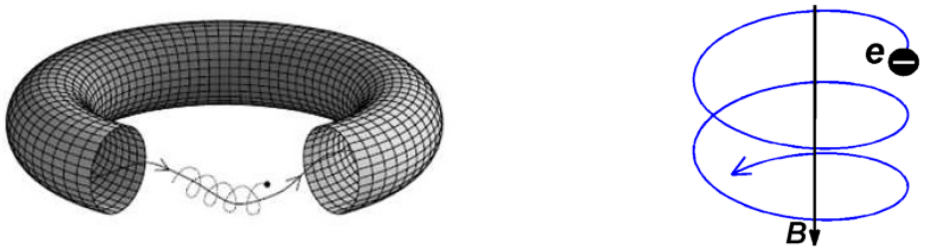

Figure 2.1: Gyro motion of charged particles

oped from the studies on the pinch effect, leading to the tokamak and RFP configurations in the 1950s and 1960s. Both tokamak and RFP devices achieve the pinch effect due to a current carrying plasma embedded in a magnetic field, but the RFP, unlike the tokamak, is characterized by axi-symmetric magnetic field toroidal and poloidal components of the same order of magnitude (fig. 2.2), with the toroidal component almost entirely generated by the current flowing in the plasma itself. The name Reversed Field Pinch derives from the fact that the toroidal field is slightly reversed in the outermost plasma region.

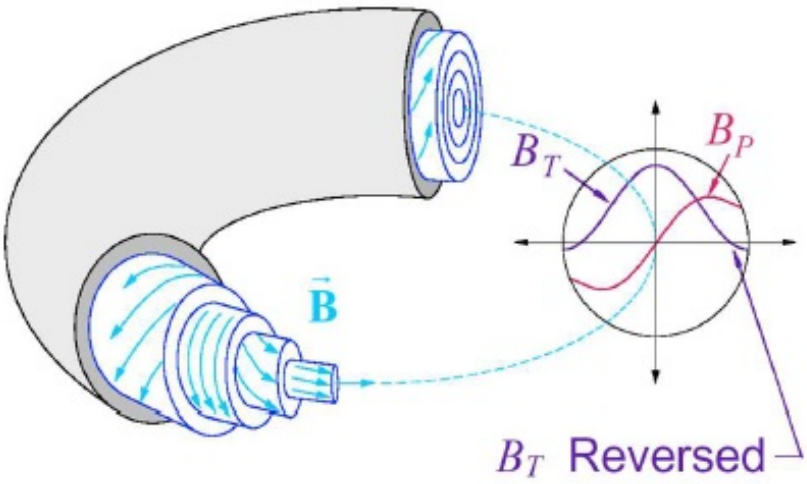

Figure 2.2: RFP magnetic field configuration

RFP devices performances have been limited so far, due to the saturation of MHD instabilities that were considered necessary for the dynamo process to develop; the dynamo process is fundamental for the magnetic field reversal, thus the sustainment of the configuration in time. Recently, the discovery of Single Helical Axis (SHAx) states in RFX-mod experiment, has led to the theoretical prediction that the magnetic field reversal can be sustained also in a chaos-free configuration, with the dynamo effect provided by a single MHD mode.

2.2 MH, QSH and SHAx states

2.2.1 Safety factor

It is common practice in plasma physics to speak of fluctuations in terms of their mode number content. Typically, m is used for the poloidal mode number (number of periods in one poloidal circumference) and n for the toroidal mode number (number of periods in one toroidal circumference).

The safety factor profile can be defined as:

$$q(r) = \frac{m}{n} \tag{2.1}$$

The average poloidal angle $\Delta\theta$ defined by a field line crossing a poloidal section after one toroidal transit, can be defined as *rotational transform* ι. The safety factor can also be defined

as:

$$q = \frac{2\pi}{\iota} \tag{2.2}$$

This means that q can also be meant as the number of turns of a magnetic field line in the poloidal direction, after a complete turn in the toroidal one. Considering a cylindrical approximation, the safety factor becomes:

$$q(r) = \frac{r}{R_0}\frac{B_\theta(r)}{B_z(r)} \tag{2.3}$$

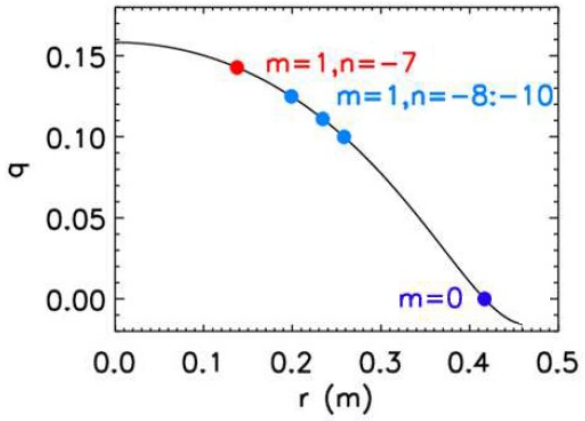

Figure 2.3: Safety factor profile in a cylindrical approximation

As can be seen from fig. 2.3, the safety factor assumes rational values for several flux surfaces; these flux surfaces are called rational, or resonant. Tearing modes around these surfaces, with the same m and n are unstable. Tearing modes are resistive modes responsible for the creation of magnetic islands; a magnetic island is a closed magnetic flux tube, bounded by a separatrix, isolating it from the rest of space. The primary significance of the islands is that heat can flow rapidly across them by following the field lines. As a result, magnetic islands represent a loss of confinement volume. Another observation from fig. 2.3 is that the small value of q at the edges of the plasma region, means that the magnetic field lines are almost poloidal, or completely poloidal on the reversal surface ($q = 0$); this results in the fact that all the $m = 0$ modes on the reversal surface are resonant.

2.2.2 MHD modes

The exploration of a wide range of plasma current levels in RFX-mod, thanks to an advanced feedback control system, made possible the experimental evaluation of regimes which clearly shows an evolution towards the SHAx state. At low plasma current values, below $800kA$, the configuration is characterized by a Multiple Helicity (MH) regime, where several resonant tearing modes, mostly in the $m = 0$, $m = 1$ spectra and various n modes, give rise to a chaotic plasma. The presence of several MHD modes resonating on different plasma layers, gives rise to overlapping magnetic islands, which results in a plasma with flat temperature profile (fig. 2.4).

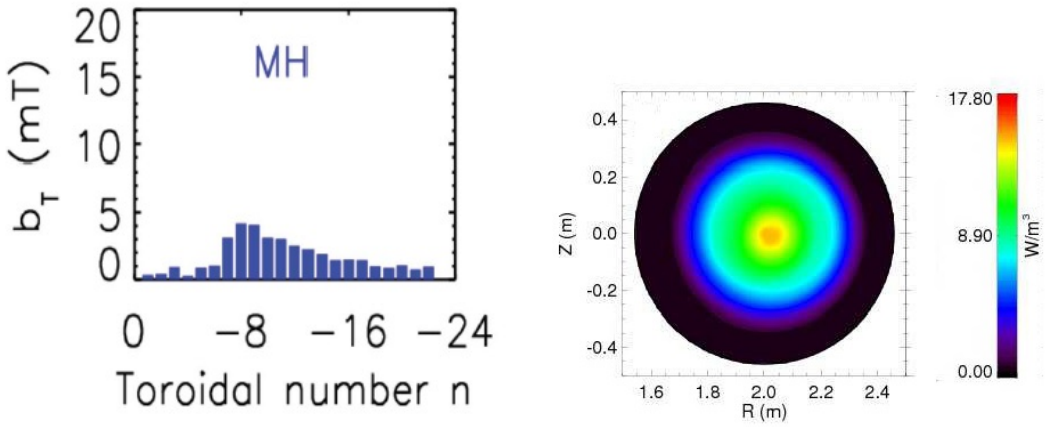

(a) MSH spectra

(b) Temperature map on the poloidal plane

Figure 2.4: Multiple Helicity regime

By increasing the plasma current, transient states towards the SHAx state are observed. These Quasi Single Helicity (QSH) states are characterized by a single dominant resonant mode, defined by a couple m, n, and several secondary modes with a much lower amplitude (fig. 2.5).

The chaotic structure reduces as the plasma current is increased, because the dominant mode becomes purer and purer. In RFX-mod, experimental results showed that above a threshold of 4% in the dominant mode normalized amplitude (with respect to the total magnetic field at the edge of the plasma), a topological change in the magnetic configuration is observed: the O-point of the dominant magnetic island becomes the only magnetic axis and a Single Helical Axis (SHAx) state is reached (fig. 2.6).

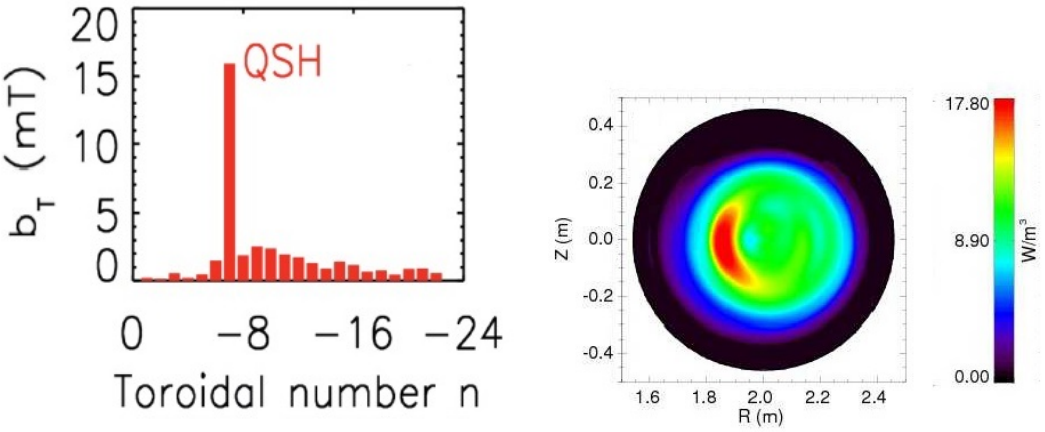

(a) MSH spectra

(b) Temperature map on the poloidal plane

Figure 2.5: Quasi Single Helical regime

With a sufficiently high plasma current, a SHAx stationary state could theoretically be reached. As seen, a SHAx state is an improved confinement state where the magnetic flux surfaces are nested and winded around a single helical axis. The single axis results from the merging of the axi-symmetric configuration magnetic axis and the X-point of the magnetic island correlated to the dominant mode. The SHAx equilibrium is characterized by strong temperature gradients (fig. 2.7) in the edge plasma region, thus indicating the creation of a strong internal transport barrier; this translates into improved plasma confinement and stability properties.

The spontaneous occurrence of the SHAx equilibrium with reduced magnetic fluctuations and strong transport barriers can lead to a new paradigm for the RFP. As the persistence of the SHAx states has been experimentally shown to increase with plasma current, the probability of achieving steady SHAx states in larger devices should be considered. These new results can lead into a reassessment of the RFP configuration as a low-external-field, ohmically heated approach to nuclear fusion; this configuration, exploiting both self-organization and technological simplicity with respect to the tokamak and stellarator configurations, could become a preferable solution for future FFH or fusion devices.

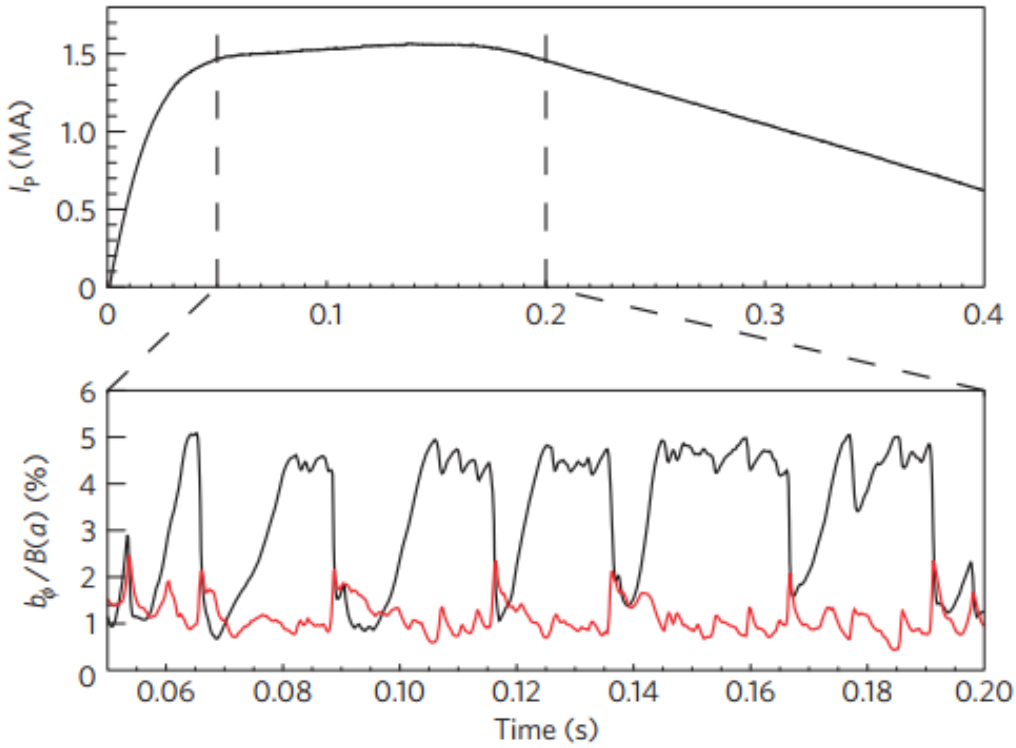

(a) SHAx states reached in a non-stationary way, in a 1.5 MA discharge

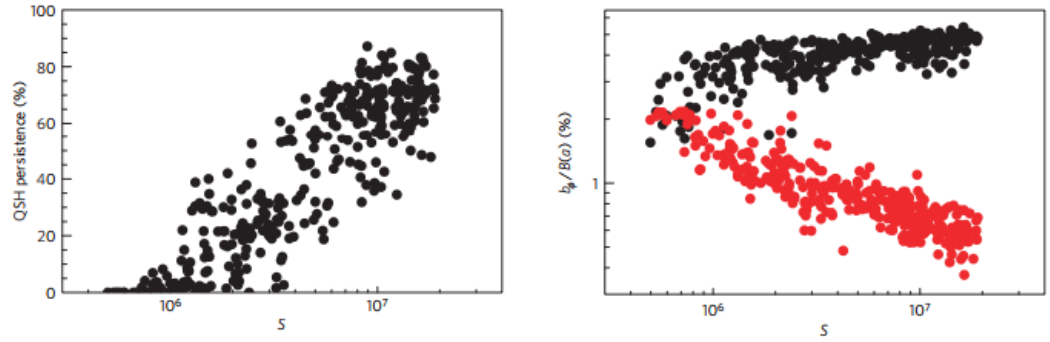

(b) QSH persistence and amplitudes of the dominant (black) and secondary (red) modes, versus the Lundquist number (correlated to the plasma temperature)

Figure 2.6: QSH features in RFX-mod

2.3 Dynamo process and toroidal field reversal

From MHD equations, combining Ohm's law, Ampere's law and Faraday's law, the following is obtained:

$$\frac{\partial \overline{B}}{\partial t} = \nabla \times (\overline{v} \times \overline{B}) + \frac{\eta}{\mu_0} \nabla^2 \overline{B} \tag{2.4}$$

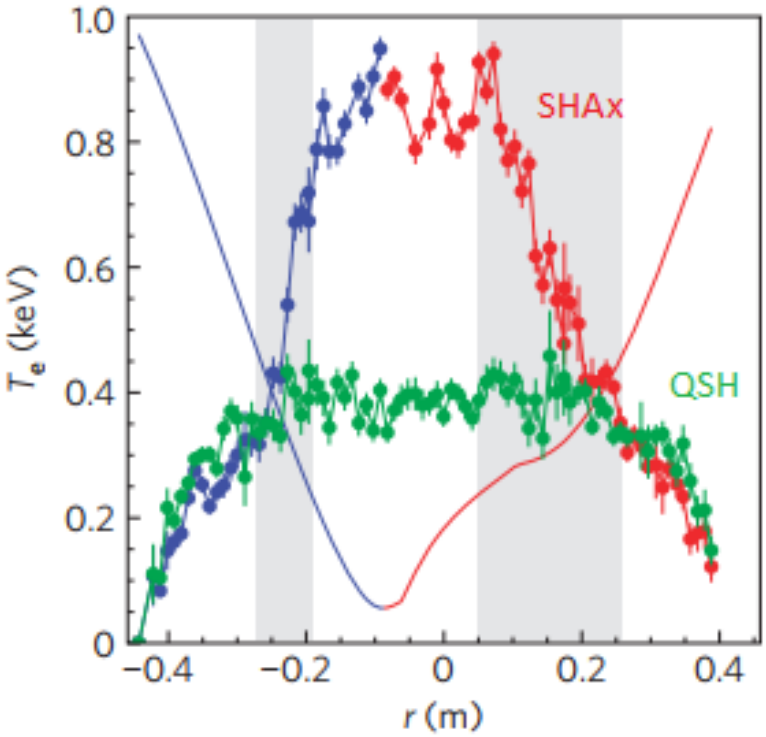

Figure 2.7: Temperature profile on a poloidal section for SHAx and QSH states

Two terms can be identified:

- Convection $\nabla \times (\overline{v} \times \overline{B})$
- Diffusion $\frac{\eta}{\mu_0} \nabla^2 \overline{B}$

If $\overline{v} = 0$ and the resistive term is non-null, the Reynolds magnetic number (defined as the ratio between the convection and the diffusion term) becomes null, hence the magnetic field follows a resistive diffusion equation.

The resistive diffusive time is defined as:

$$\tau_R = \frac{\mu_0 \cdot a^2}{\eta} \tag{2.5}$$

With a the plasma radius. Without a mechanism such the dynamo process sustaining the toroidal magnetic flux, the toroidal magnetic field would rapidly become constant and equal to the edge value, following the diffusive equation 2.4 (fig. 2.9).

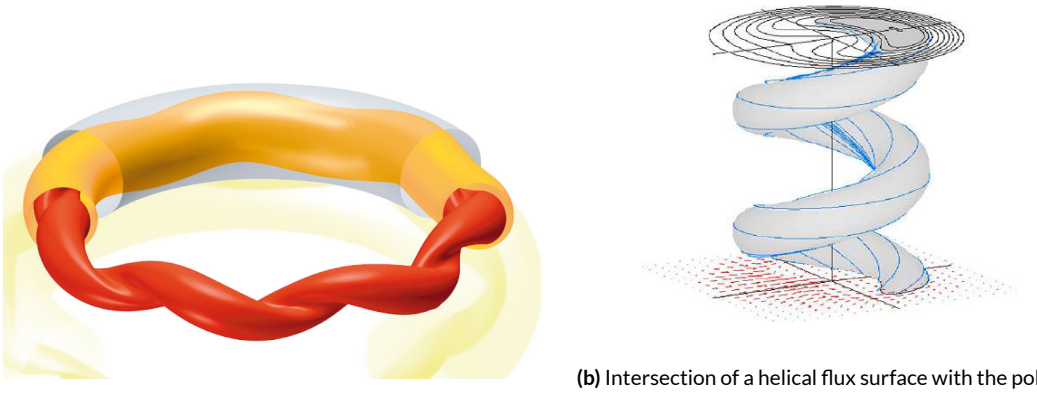

(a) SHAx 3D shape

(b) Intersection of a helical flux surface with the poloidal plane

Figure 2.8: Single Helical Axis state representation

The dynamo process is a fundamental component for the RFP stability, as it opposes the resistive diffusion.

Considering now the cylindrical approximation and stationary conditions, we can derive the current density profile using Ampere's law:

$$J_\theta = -\frac{1}{\mu_0}\frac{\partial B_\varphi}{\partial r} \tag{2.6}$$

$$J_\varphi = -\frac{1}{\mu_0 r}\frac{\partial (r B_\theta)}{\partial r} \tag{2.7}$$

On the reversal surface, the magnetic field is only poloidal; as a consequence, the current density must have only the toroidal component. The left-hand side of the 2.6 is equal to zero, hence, the toroidal field should reach its minimum at the reversal surface; but this contradicts the toroidal field reversal, meaning that a poloidal component of the current density is necessary, and it can't obviously be driven by the toroidal e.m.f. V_{loop}, as well as a $v \times B$ term (eq. 2.9) in the poloidal direction, since the magnetic field is only poloidal on the reversal surface. For this reason, the dynamo process is understood as a $v \times B$ term in the poloidal direction, generated by the interaction between the velocity and the perturbation fields; this is why the perturbation modes were considered necessary for the field reversal, theoretically limiting the RFP quality of confinement.

The standard explanation of the field reversal in RFP configurations comes from Taylor's relaxation theory, which considers a plasma as an isolated system, inside a cylindrical flux conservator, in a force-free equilibria with null velocity. The solution is described by the Bessel

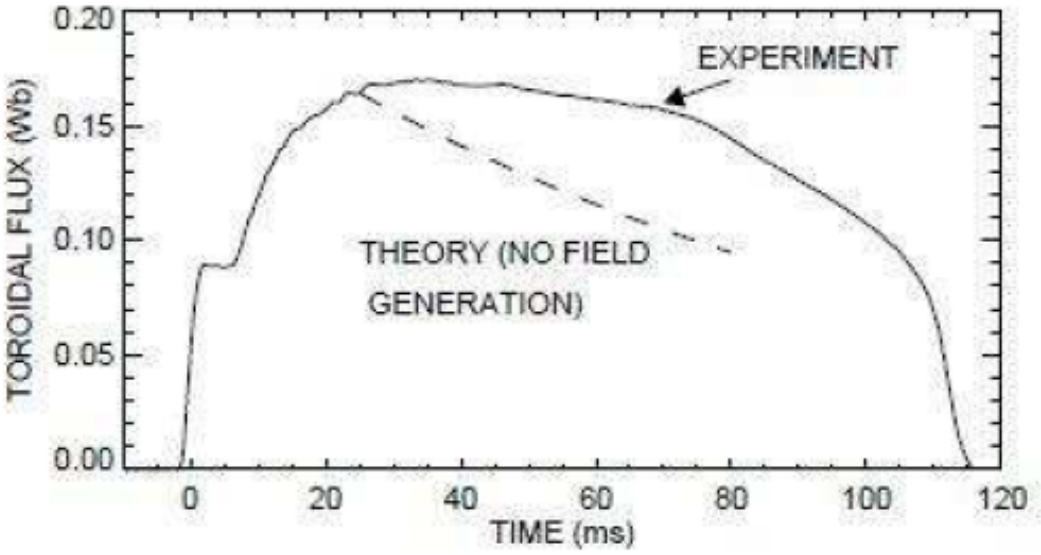

Figure 2.9: Toroidal flux as a function of time

Function Model (BFM), assuming $J = \sigma B$ with a uniform conductivity profile.

$$\begin{cases} B_r(r) = 0 \\ B_\theta(r) = B_0 J_1(\theta r) \\ B_\varphi(r) = B_0 J_0(\theta r) \end{cases}$$

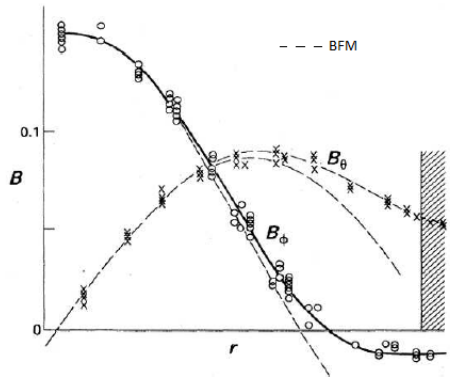

2.3.1 The wire model

The Taylor's relaxation theory doesn't really fit with experimental results because of several false assumptions; the two main hypothesis that disagree with the reality are the constant profile of σ and the achievement of the equilibrium with an axi-symmetric configuration. The conductivity is not constant over the plasma, but it strongly varies outside the reversal radius and the Cowling's theorem states that a reversed axi-symmetric equilibrium can not exist. Therefore, we must consider the dynamo process acting against the magnetic field diffusion,

thus breaking the axi-symmetry of the equilibrium system, in agreement with Cowling's theorem.

This can be done considering a new approach, described by the wire model. We consider a current carrying wire inside a cylinder, with coils wrapped on it that produce an axial magnetic field and act as a flux conserver (fig. 2.10a). If a current instability develops, i.e. a poloidal component is present in the wire current density, and if it has the same orientation of the external coils current, a mutual attractive force develops. The instability also brings an increase in the internal wire field, with a consequent reduction on the current in the cylinder; this process continues since the current in the cylinder reverses, leading to an equilibrium with a field reversal and a loss of axi-symmetry (fig. 2.10b), in accordance with experimental results and the Cowling's theorem.

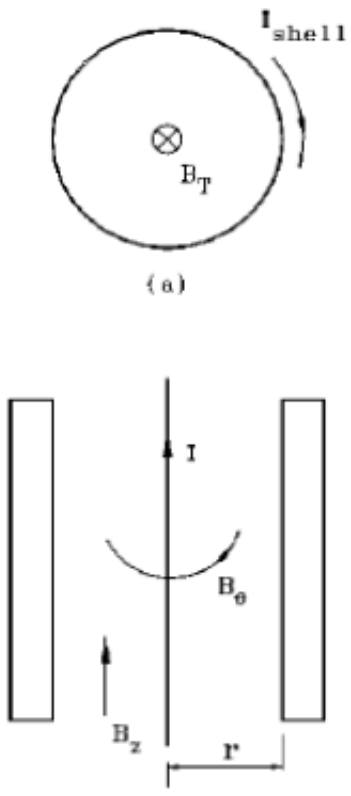

(a) Wire with an axial current component in a flux conserver

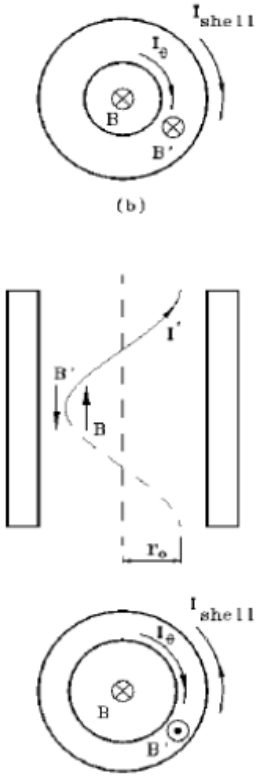

(b) Wire current instability and new equilibrium with reversed field

Figure 2.10: The wire model

Quello che noi ci immaginiamo, bisogna che sia o una delle cose già vedute, o un composto di cose o di parti delle cose altra volta vedute.

Galileo Galilei

3
RFX-mod

The Reverse Field eXperiment modified (RFX-mod), is a toroidal device designed and built in Padova for experiments on magnetically confined and ohmically heated plasma in the reversed field pinch configuration. RFX-mod is an evolution of the previous RFX machine, operational since 1991, and it is located in Padova, at the Istituto Gas Ionizzati inside the research area of CNR. RFX-mod is operational since 2004, under the management of Consorzio RFX, a research organization promoted by CNR, ENEA, Università di Padova, Acciaierie Venete S.p.A. and INFN, within the framework of the Euratom - ENEA Association.

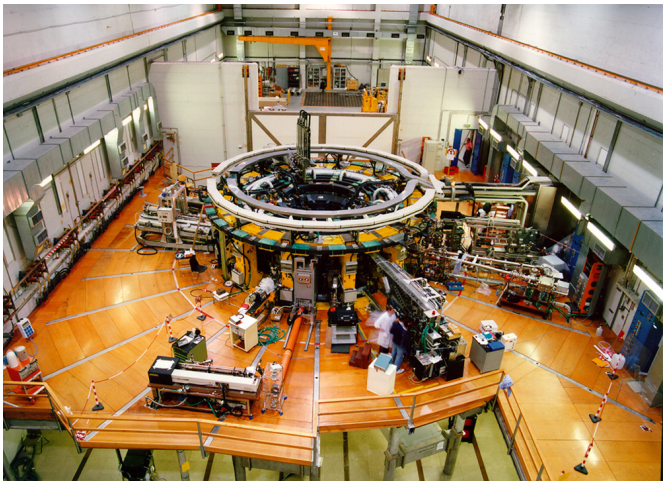

Figure 3.1: RFX-mod machine

The RFX-mod system consists of a load assembly, the power supply system, the control system, the diagnostics, a power substation and the auxiliary facilities. Since the objective of this thesis is to modify the load assembly in order to obtain the conditions for a stationary SHAx state, and the only way to do it is to scale the plasma major and minor radii and the magnet system, this last one and the circuital schemes will be analysed below.

3.1 RFX-mod magnet system

The RFP configuration requires the presence of both poloidal (B_P) and toroidal (B_T) magnetic field components. The toroidal component is produced by a toroidal field winding, whereas the poloidal component is produced by a poloidal field winding and the plasma itself. The B_P and B_T components are comparable in RFP devices, hence, given the same aspect ratio ξ and plasma current, the toroidal component is about one order of magnitude smaller than that of a tokamak device.

The RFX-mod magnet system consists of four windings (fig. 3.2):

- Ohmic heating coils
- Toroidal field coils
- Field shaping coils
- Saddle coils

3.1.1 Toroidal field winding

The toroidal field winding is responsible for the creation of an initial bias field at discharge break-down, and a reference negative field during the flat top phase, which establish the reversal conditions at plasma edge. The bias field reaches the maximum value at the beginning of the discharge, then decreases to zero as the plasma current rises. After the zero-crossing, the TF-winding current is reversed and sustained by the TF power supplies, establishing the reversed field value at the plasma boundary (fig. 3.3); it should be noted that, even without TF-windings, the dynamo would still ensure the magnetic field reversal, but the B_T value is controlled by the TF-coils in order to achieve better plasma discharges. The dynamo process also maintains an average positive value of the toroidal field in the inner plasma region.

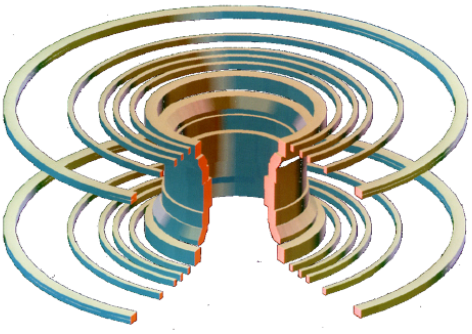

(a) Ohmic heating coils

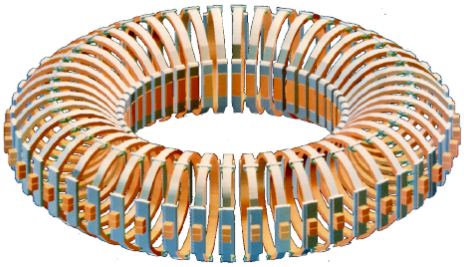

(b) Toroidal field coils

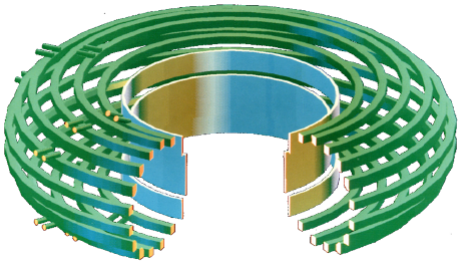

(c) Field shaping coils

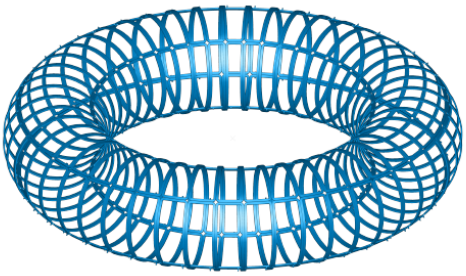

(d) Saddle coils

Figure 3.2: RFX-mod magnet system

In RFX-mod, the TF-winding consists of 48 coils, subdivided into 12 parallel sectors of 4 series coils, to achieve arrangement flexibility. The maximum bias field produced is $B_0 = 0.7T$ at plasma start-up, whereas the maximum reversed field at flat-top is $B_w = 0.44T$.

Table 3.1: TF-winding parameters

Number of coils	48
Number of turns per coil	8
Coil mean diameter	1.24 m
Maximum toroidal field	0.7 T
Maximum current	18.3 kA
Voltage to earth	3.5 kV
Voltage per turn	219 V

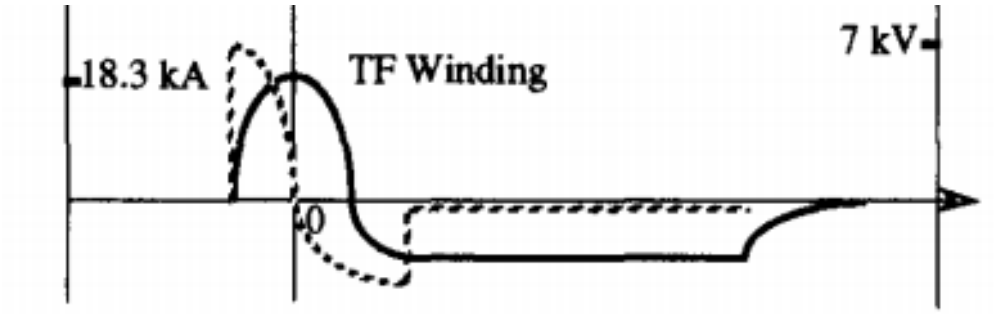

(a) Current and voltage profile during a discharge (starting at time t=0)

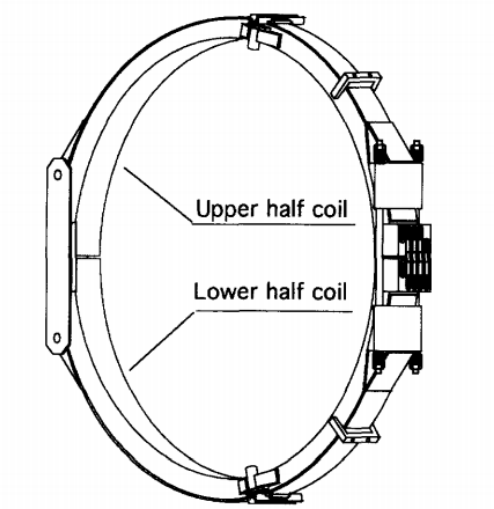

(b) Toroidal field coil

Figure 3.3: TF-winding features

3.1.2 Ohmic heating winding

The ohmic heating winding is part of the Poloidal Field (PF) coils. The OH-winding acts as the primary circuit of a transformer, where the secondary circuit is represented by the plasma; a rapid and large flux swing is required to induce a large e.m.f. in the plasma, leading to the break-down conditions. The plasma e.m.f. is commonly referred as loop voltage (V_{loop}). The plasma start-up in RFX-mod is carried out inducing a flux variation of $15Wb$, hence a maximum loop voltage of about $730V$; the OH-winding is first charged with the desired current value then, when the required flux is produced, the coils are short-circuited. At the beginning of the plasma pulse, the OH-winding is discharged on a transfer resistor (R_T) with a value that guarantees the voltage to earth to be within $\pm 17.5kV$. After a first flux swing with a time constant determined by the RL circuit, a power supply is connected to the OH-

winding to vary the current gradient; the flux variation is carried out continuously, with the longest plasma discharges achieved through a bipolar flux swing, hence with a current reversal. During the flat top, the flux is varied to compensate the plasma V_{loop}.

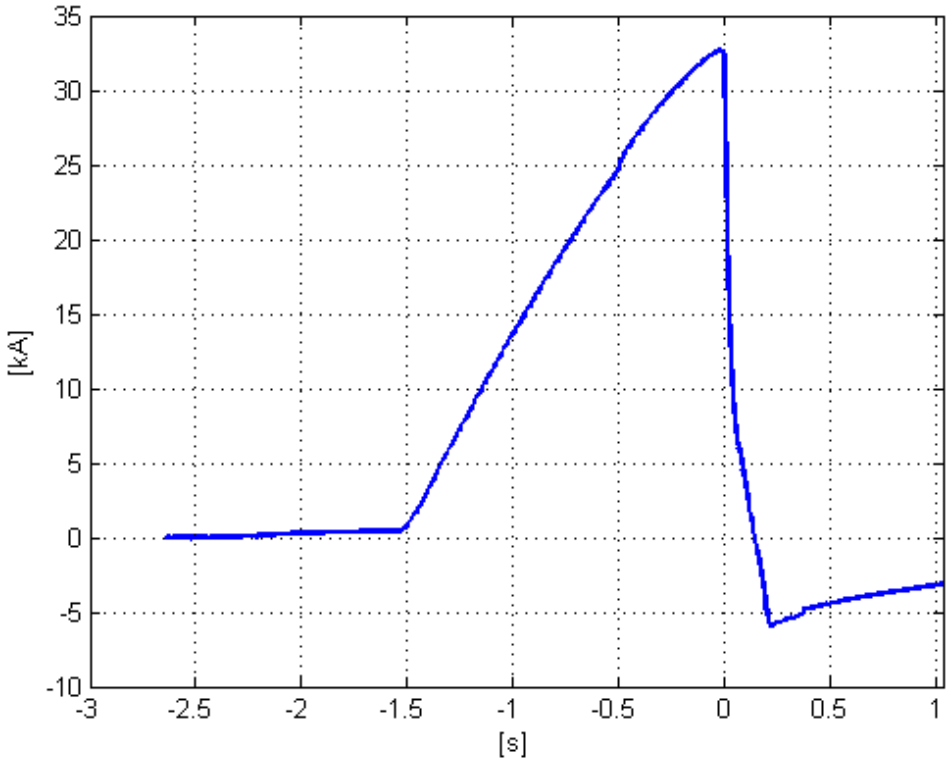

Figure 3.4: OH-winding current profile

The OH-winding consists of 200 turns, forming a total of 40 coils placed symmetrically above and below the equatorial plane. An optimization was carried out, considering the minimization of the stray field in the plasma region and the maximization of the flux linkage as objective functions. This led to the geometry displayed in fig. 3.5.

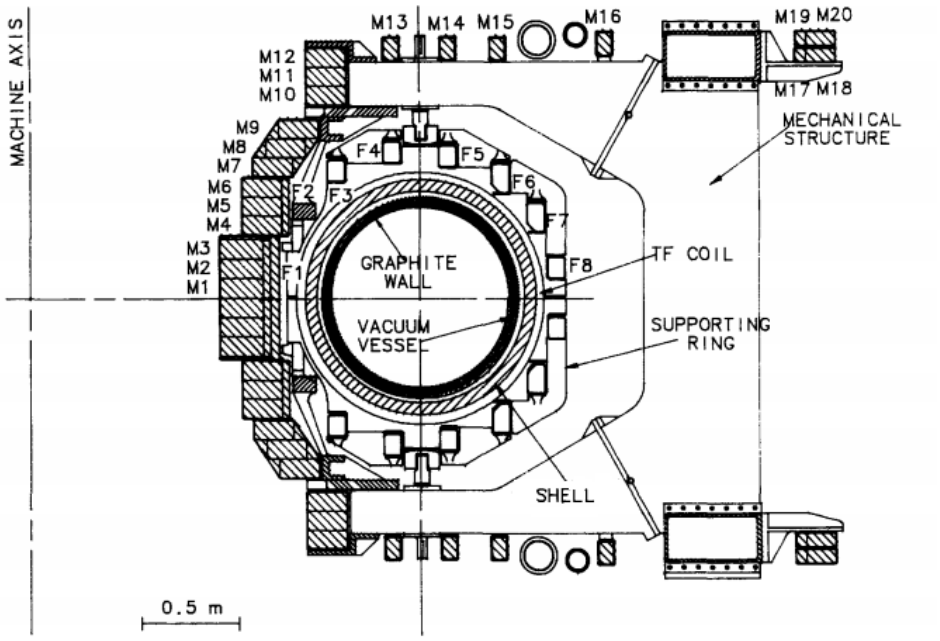

(a) RFX geometry, with OH-winding $M1 \div M20$

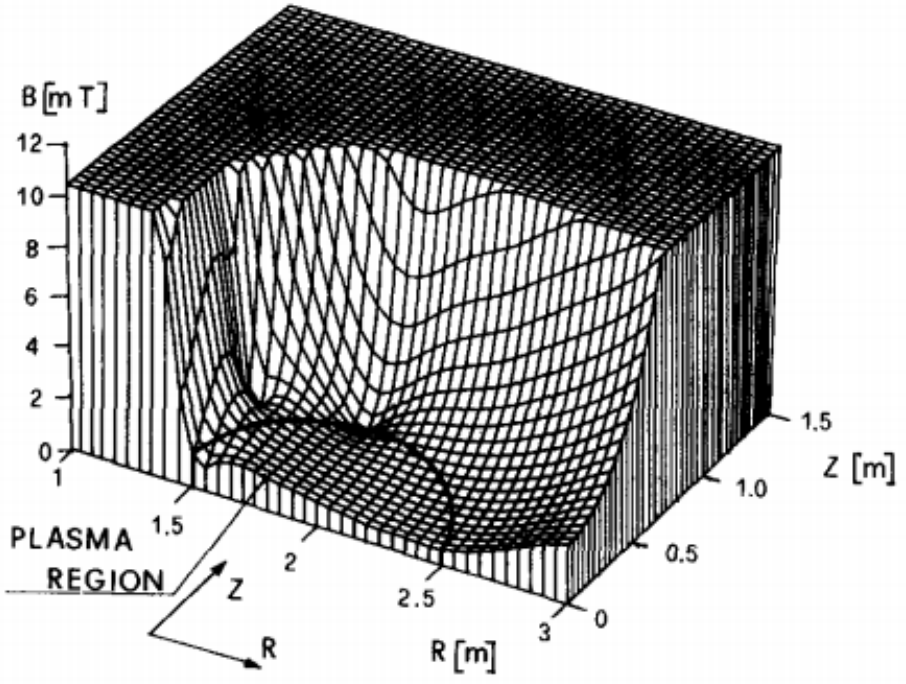

(b) Stray field in the plasma region

Figure 3.5: OH-winding features

Table 3.2: OH-winding parameters

Number of coils	40
Coils group	Number of turns per coil
$M1 \div M3$	8
$M4 \div M12$	6
$M13 \div M15$	4
$M16$	2
$M17 \& M19$	1
$M18 \& M20$	3
Voltage to ground	17.5 kV
Voltage between coil groups	35 kV

3.1.3 Field shaping winding

The field shaping winding is responsible for the control of the plasma equilibrium, through the application of a vertical field to counteract the outwards displacement of the plasma in the major radius direction. The field shaping winding acts together with a copper stabilizing shell, which was introduced in RFX-mod substituting the old aluminium shell; the copper shell has a magnetic field penetration time constant of $50ms$, which guarantee a fast control action from the FS-winding. More precisely, the FS-winding exploits three functions:

1. Compensation of the error field on the shell surface in the early stages of the discharge

2. Production of an equilibrium field to counteract the plasma displacement

3. Compensation of the plasma magnetomotive force

The FS-winding consists of 16 coils, with 24 turns each, placed symmetrically with respect to the equatorial plane. Each symmetric couple of coils (above and below the symmetry plane) is connected in series, to form 8 FS sectors independently controlled.

Table 3.3: FS-winding parameters

Number of coils	16
Number of turns per coil	24
Average current per turn	5.2 kA
Voltage per turn	730 V
Voltage between terminals	17.5 kV
Voltage to ground	17.5 kV

3.1.4 Saddle coils

RFX-mod is equipped with an advanced system for the local feedback control of MHD modes. The saddle coils system consists of 192 coils, arranged in groups of 4 in 48 toroidal positions. Each coil is independent and can produce a magnetic field up to $50mT$ DC or $3.5mT@100Hz$.

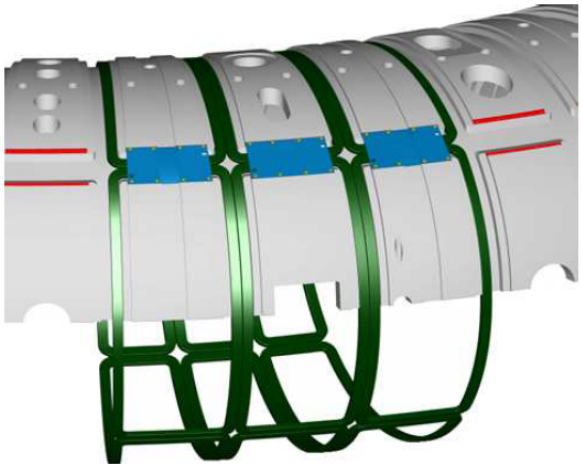

Figure 3.6: RFX-mod saddle coils

The algorithms for real-time control of the tearing modes that resulted in enhanced machine performances are the Virtual Shell scheme and the Clear Mode Control scheme; the introduction of the copper shell and the saddle coils, again with the improvement on the control algorithms and the power supply system, led to the enhancement of the peak plasma current and the quality of discharges (fig. 3.7), which permitted to experiment QSH and SHAx states.

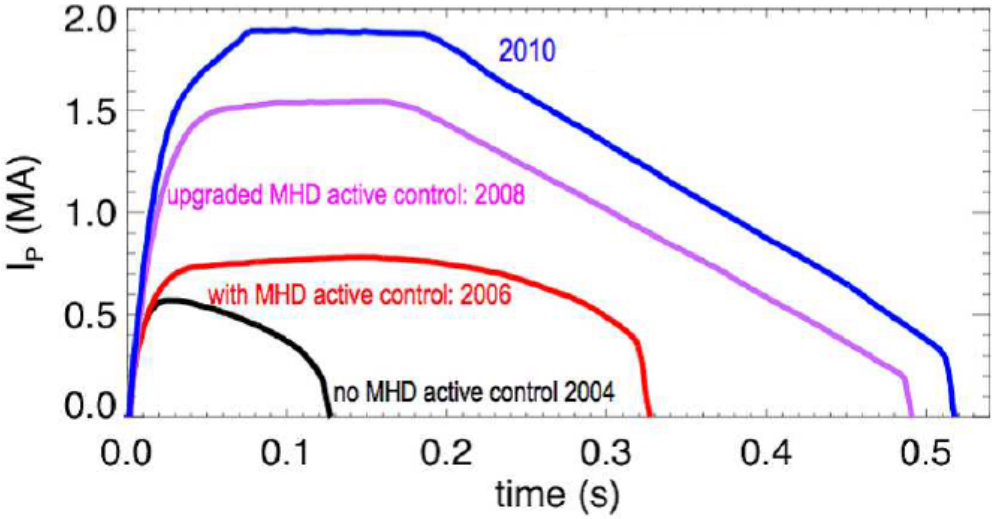

Figure 3.7: RFX-mod improvements on discharge quality

3.2 RFX-mod circuit

The RFX-mod circuit is composed of a poloidal field circuit and a toroidal field circuit. The poloidal field circuit is responsible for the plasma ignition and control, whereas the toroidal field circuit control the field reversal at the plasma edge.

3.2.1 Circuit operations

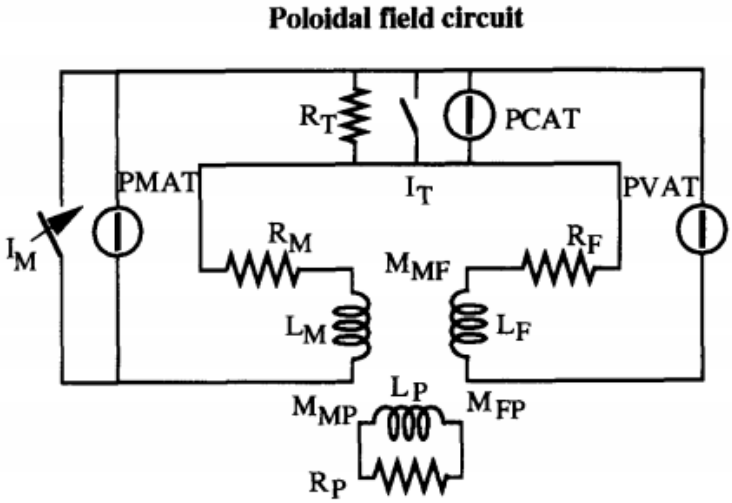

(a) PF circuit

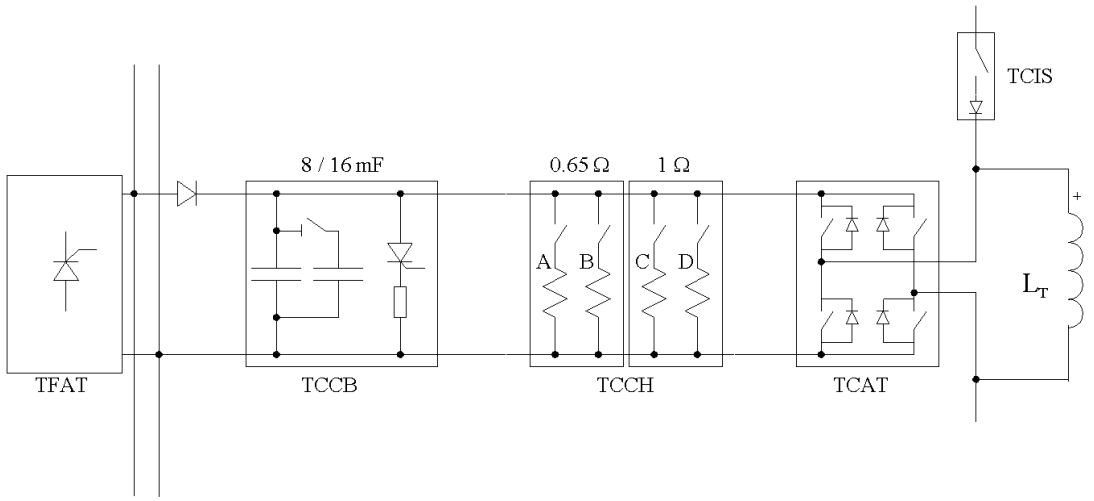

(b) TF circuit of one section

Figure 3.8: RFX-mod circuit

Referring to the circuital scheme in fig. 3.8, one can think of an operational sequence (fig. 3.9) divided in three parts:

1. Before the starting of the discharge, the OH-winding is brought to the operation flux by the power supply PMAT, then the PMAT is short-circuited. The 12 sectors of the TF-winding are connected in series and fed by the TFAT AC/DC converters, to reach the maximum value of the bias toroidal field.

2. At t=0, when the TF-winding field is maximum, the circuit breaker I_T is opened and the OH current starts to decrease rapidly by flowing through the transfer resistor R_T, inducing a flux variation, hence a V_{loop} high enough to ignite the plasma discharge. The current on each sector of the TF-winding is redirected to the capacitor bank (TCCB) through the free-wheeling diodes of the TCAT; the current decreases, and the derivative depends on the capacitors voltage, regulated by a chopper (TTCH). The TF-winding total current rises with the same profile of the plasma one, since it compensate the m.m.f.

3. When the plasma current reaches the flat top value, the PCAT power supply is turned on, to sustain the plasma current, by compensating the V_{loop}. PVAT power supply controls the FS current, to provide the proper equilibrium field.

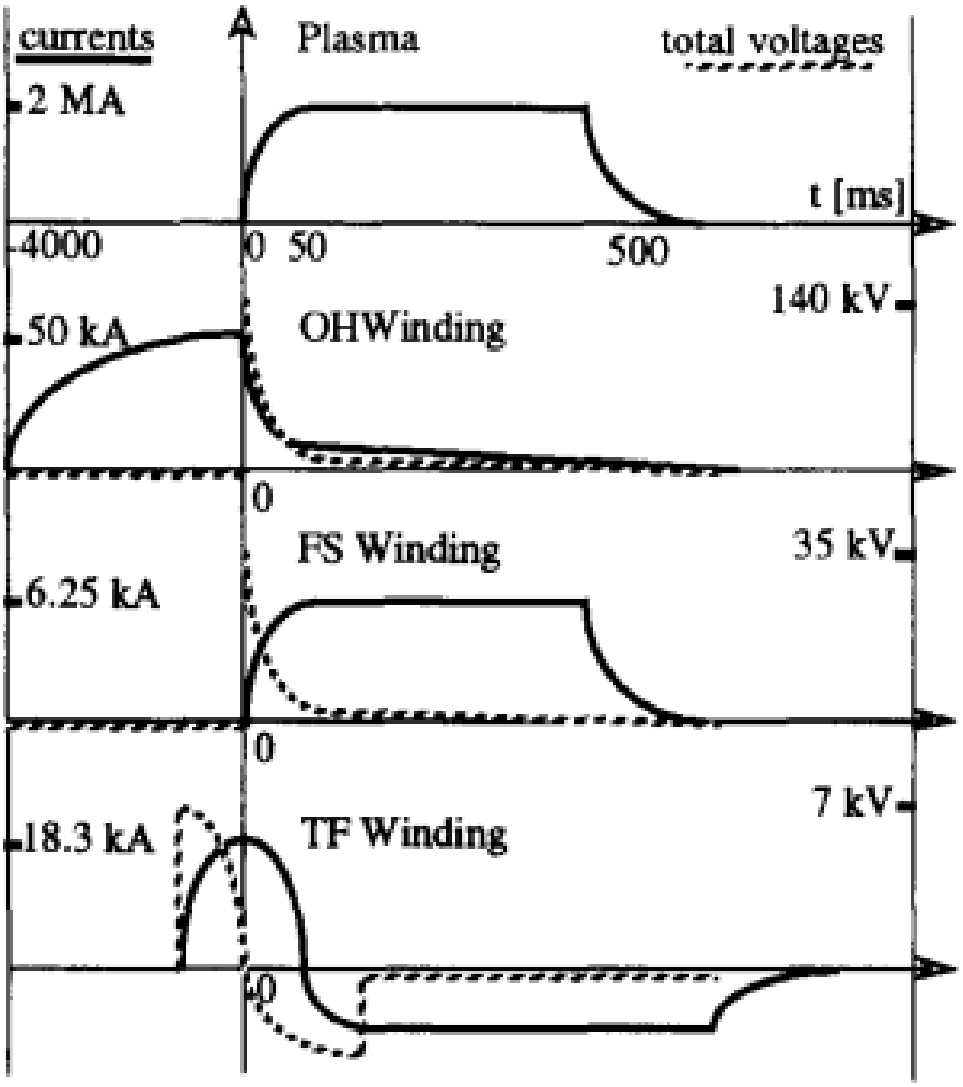

Figure 3.9: RFX-mod operation waveforms

If the TF-winding acts as a flux conserver, the plasma relaxation process that leads to the typical RFP field profile is spontaneously reached at sufficient high plasma currents; hence, the TF circuit acts to keep the total flux constant, as the plasma current generates an additional toroidal field component.

The OH-winding acts instead as the primary of a transformer, which induces an e.m.f. in the plasma (V_{loop}) through the variation of the concatenated flux (flux swing). From the circuital point of view, the plasma current dynamic can be described considering only the

coupling of the PF-circuit and the plasma circuit.

3.2.2 Poloidal field circuit

In RFX-mod, the PF circuit is defined by an octagonal circuit topology. The OH-coils and the FS-coils are connected to form four sectors, alternated with other four sectors consisting of the transfer resistors (PTRB) and the PCAT power supplies (fig. 3.10). Each node delimiting the edges of the sectors are grounded through an high impedance.

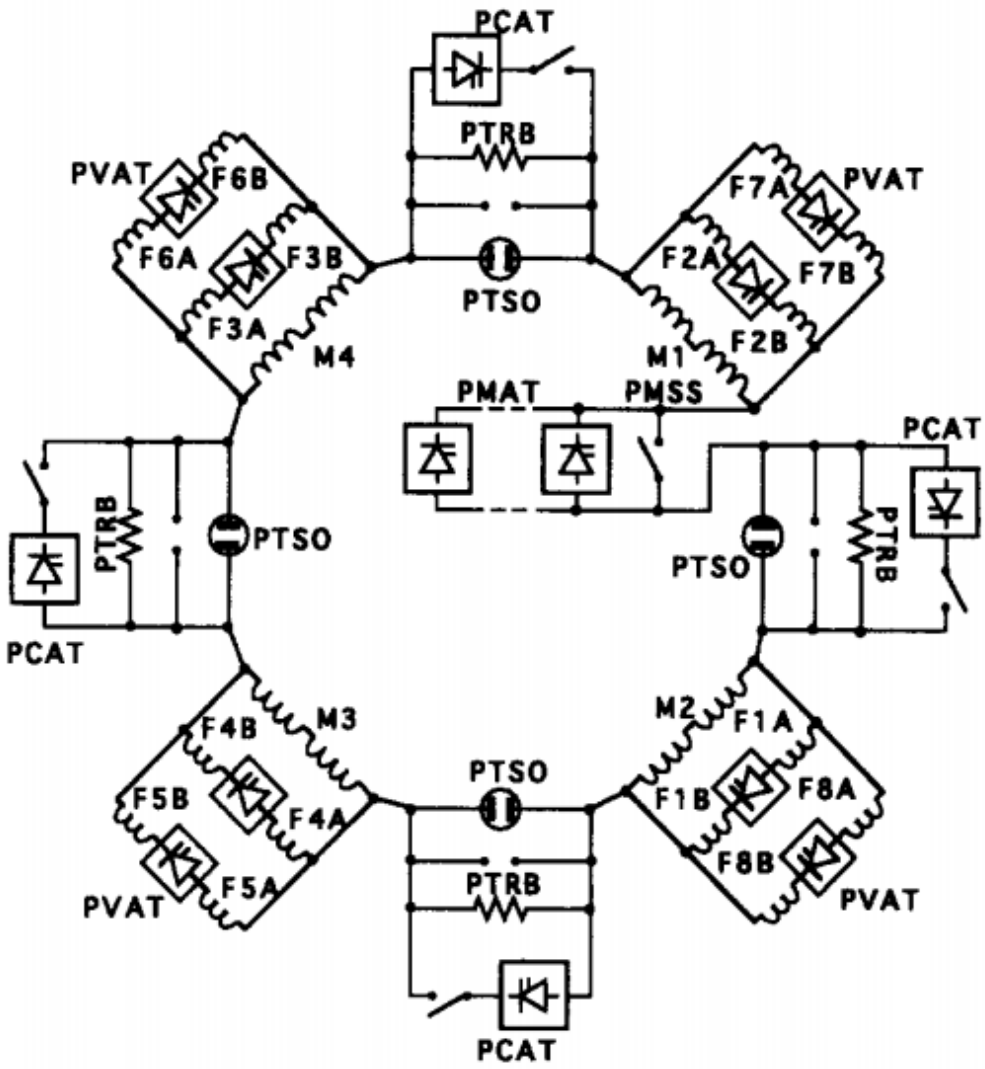

Figure 3.10: Scheme of the PF circuit

The scheme considers a subdivision of the PF-winding in four sectors, in order to limit

the voltage to ground; in fact, the total e.m.f. of the circuit is $140kV$, but being split into 4 sectors and with a proper redistribution of the windings, as in fig. 3.10, the voltages between the central point in an OH sector and earth are equal and kept within $\pm 17.5kV$.

Plurality ought never be posited without necessity.

William of Occam

4

Equivalent circuits

In this thesis, the circuit analysis is limited to the PF circuit, since the objective is to evaluate the maximum transferable energy from the ohmic heating winding to the plasma, for a set of different geometries.

As mentioned before, the PF circuit topology of RFX-mod is octagonal (fig. 4.1). The OH winding and the FS winding are subdivided in four sectors and connected in parallel; this configuration was studied to limit the voltage to ground and to ensure a homogeneous redistribution of the load. In fact, the winding redistribution has been designed to minimise the difference between the mutual coupling and the impedance of the four sectors. This design constraint permits to make a very useful assumption for the definition of an equivalent circuit.

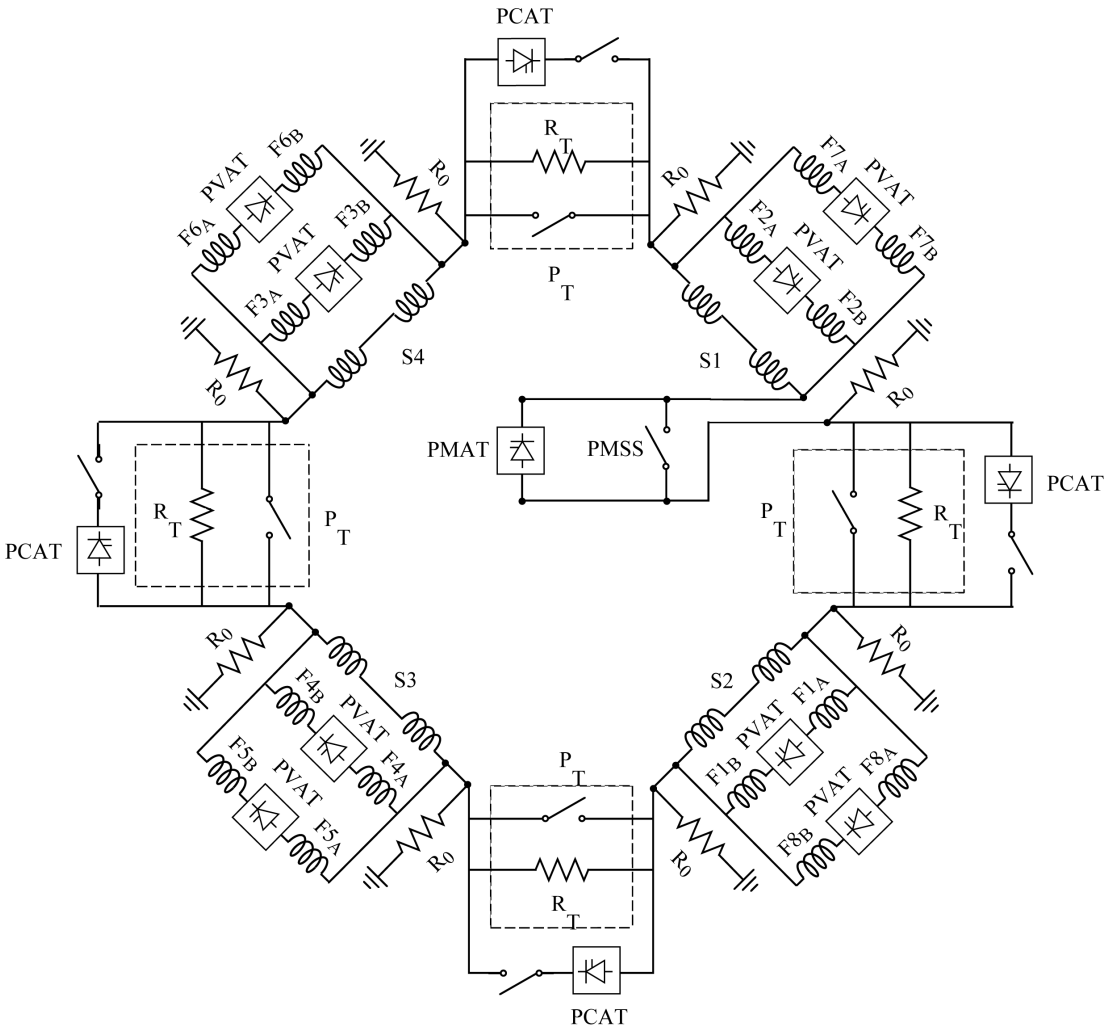

Figure 4.1: RFX-mod PF circuit

Since the RFX-mod PF circuit represents a great complexity for the analysis of current evolution and an excessive precision is not necessary at this stage, a simplified equivalent circuit is fundamental for an easy and rapid evaluation of a large set of configurations, especially when carrying out an optimization. Two equivalent circuits have therefore been developed, the second as a simplification of the first, to facilitate the evaluation of the time dependant OH winding and Plasma current profiles.

The first equivalent circuit represents a simplified version of the PF circuit of RFX-mod, and has been developed to compare the numerical solution with experimental results obtained from discharge campaigns. This comparison has made it possible to assess the accu-

racy and the stability of the numerical model with respect to the actual machine behaviour, thus defining a model to evaluate and predict the current profile of the plasma and in each of the four sectors, considering the parameters which define each experimental discharge.

Once the model has been validated, another equivalent circuit was developed by further simplifying the first scheme under certain hypothesis and design constraints, effectively reducing the circuit complexity at minimum. This second scheme has been used to readily evaluate the OH winding and plasma current profiles for a set of scaled configurations, to allow the tuning of sensitive parameters and the exploration of a number of geometries, thus identifying a list of feasible machines.

4.1 RFX-mod equivalent PF circuit

The RFX-mod PF circuit and the plasma can be represented as three inductively coupled circuits, as pictured in fig. 4.2.

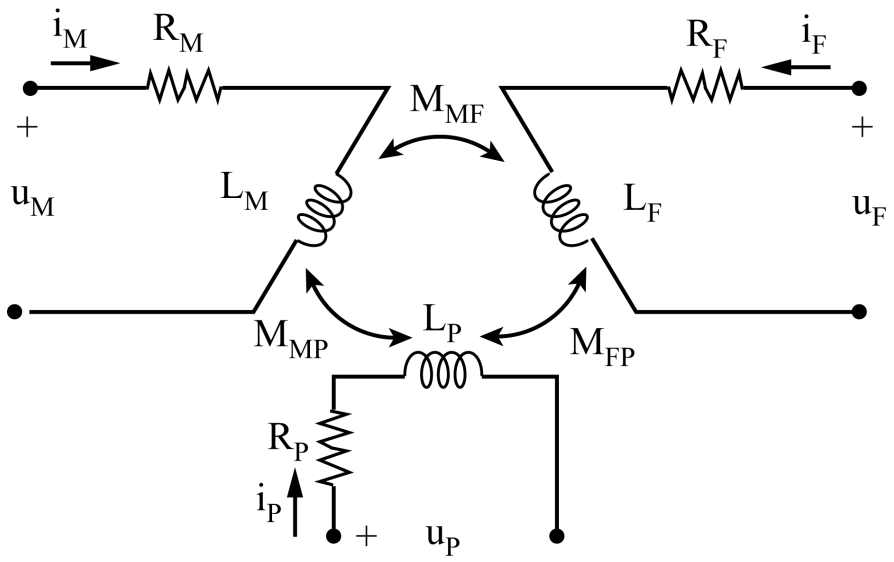

Figure 4.2: Equivalent electric network of RFX-mod

This description leads to the following system of equations:

$$\begin{cases} V_M = L_M \frac{di_M}{dt} + M_{MF} \frac{di_F}{dt} + M_{MP} \frac{di_P}{dt} + R_M i_M \\ V_F = M_{FM} \frac{di_M}{dt} + L_F \frac{di_F}{dt} + M_{FP} \frac{di_P}{dt} + R_F i_F \\ V_P = M_{PM} \frac{di_M}{dt} + M_{PF} \frac{di_F}{dt} + L_P \frac{di_P}{dt} + R_P i_P \end{cases} \tag{4.1}$$

4.1.1 Simplification of RFX-mod circuit

Now, considering the RFX-mod PF circuit design and characteristics, some simplifications can be made. To align the loads and to avoid excessive stress on the power supplies, the four sectors has been subdivided in order to guarantee a uniform impedance and mutual coupling; this translates into a minimum effort from the power supplies to compensate the unbalanced currents, and it also guarantee a quasi-uniform voltage to ground of the four sectors. Furthermore, the transfer resistances R_T, characterized by the same value, are consistent with the resistance values of the sectors. Hence, referring to the transfer resistance potential V_T and to the four sectors potentials $V_1, ..., V_4$, a first simplification can be carried out:

$$-V_T = V_1 = V_2 = V_3 = V_4 \tag{4.2}$$

If each one of the octants is considered to be subject to the same voltage, the four sectors inductances and the four transfer resistances can all be represented in parallel (fig.4.3). We can thus think about the RFX-mod circuit as a transformer, by considering the plasma acting as the secondary winding, and the PF-winding acting as the primary, with the FS winding providing the counter EMF, and the OH winding providing the magnetizing flux.

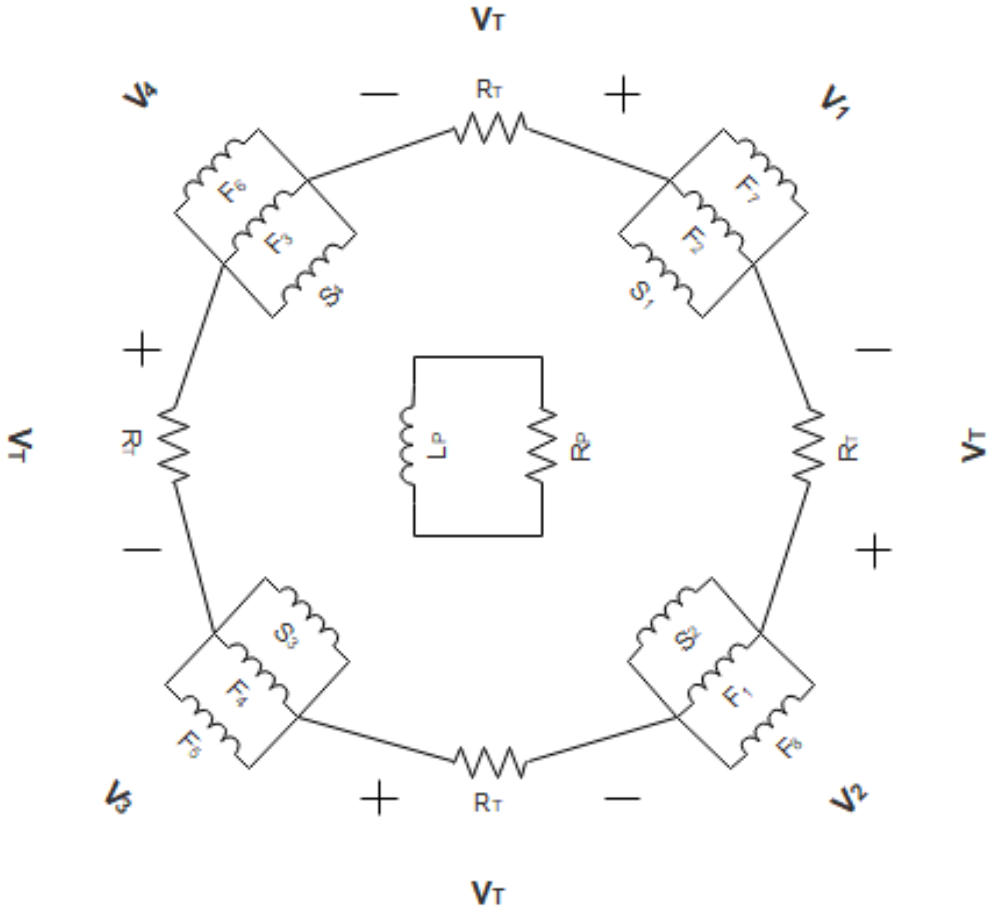

(a) RFX-mod equivalent plasma and PF winding circuit

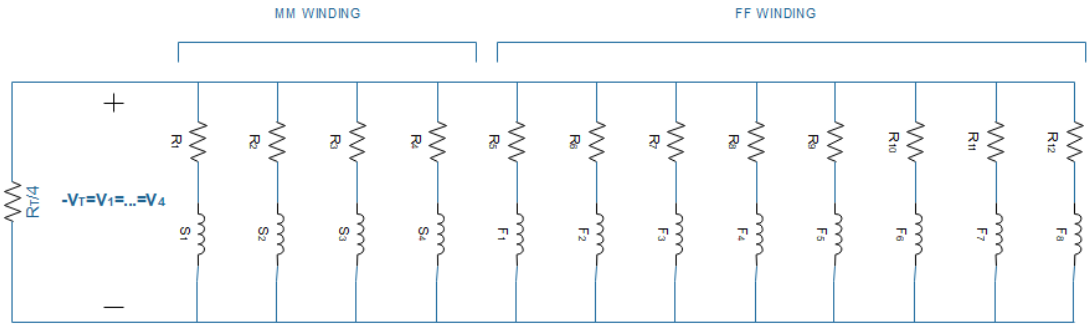

(b) RFX-mod PF winding simplified circuit

Figure 4.3: RFX-mod coupling circuits

As said, the voltage in each octant of the PF circuit can be considered the same and it can be written as:

$$V_{oct} = \frac{R_T}{4}(-\sum_{m=1}^{4} I_{Mm} - \sum_{n=1}^{8} I_{Fn}) \tag{4.3}$$

Which leads to:

$$V_M = [-V_{oct}, -V_{oct}, -V_{oct}, -V_{oct}]^T \tag{4.4}$$

Furthermore, the RFX-mod field shaping winding is designed to compensate the plasma magneto-motive force; hence, the total ampere-turns of the FS winding shall be equal and opposite to the plasma current at any given moment. Considering that, in RFX-mod, the number of coils of the field shaping winding is 48, this constraint shall be respected:

$$I_P = 48 \sum_{n=1}^{8} I_{Fn} \tag{4.5}$$

Hence, 4.3 becomes:

$$V_{oct} = \frac{R_T}{4}(-\sum_{m=1}^{4} I_{Mm} + \frac{1}{48} I_P) \tag{4.6}$$

4.1.2 Simplifications introduced by the control scheme

The current in each of the 48 FS coils is directly linked to the plasma current by means of a coefficients vector K, in order to provide a control on plasma displacement by applying a vertical magnetic field. More specifically, in RFX-mod the currents of the field shaping coils have to satisfy two requirements:

- Generation of a vertical uniform magnetic field inside the plasma volume, in order to control the position of the plasma centroid
- Compensation of the plasma magnetomotive force

Two current distributions on the field shaping coils must coexist, in order to satisfy the former requirements. There is a simple and practical way to obtain this current distribution, which can be carried out by dividing the problem into two parts:

1. Current distribution which produces a vertical field inside the plasma region, with sum of the coils and plasma currents equal to zero
2. Current distribution which produces a null field inside the plasma region, with non-zero sum of the coils and plasma currents

We assume to have an axisymmetric field geometry, with a cylindrical coordinate system, and the domain D corresponding to the plasma region poloidal cross section; since the poloidal field is generated by external currents, the current density J is zero in D. This means that, inside the domain D:

$$\nabla \times \overline{B} = 0 \tag{4.7}$$

By means of the field index $n(r, z)$, two linearly independent solutions for 4.7 can be derived. Assuming that $n * (r, z)$ can be approximated with a linear function along a radial segment (4.8), and that a uniform vertical field is required (4.9)

$$n * (r, z_0) = a \cdot r + b \tag{4.8}$$

$$B_z(r, z) = B_0 \tag{4.9}$$

The solutions, in terms of vector potential, can be written as:

$$A'_\Phi(r, z_0) = \frac{1}{r} \tag{4.10}$$

$$A''_\Phi(r, z_0) = \frac{B_0}{2} r \tag{4.11}$$

4.10 corresponds to a null magnetic field in the D domain, while 4.11 corresponds to a uniform vertical magnetic field in D. The general solution is a linear combination of 4.10 and 4.11:

$$A_\Phi(r, z_0) = c_1 A'_\Phi(r, z_0) + c_2 A''_\Phi(r, z_0) \tag{4.12}$$

The initial problem of finding the optimal current distribution on the coils, in order to have a vertical homogeneous field inside the D domain, can thus be rethought so the unknown term is the vector potential value on a line which defines a region with constant vertical magnetic field. If the vector potential has the same the value 4.11 along a line which defines a certain region, then the magnetic field inside that region will be vertical and homogeneous; on the other hand, if the vector potential has the same the value 4.10 along a line which defines a certain region, then the magnetic field inside of that region will be zero.

We thus have to find the set of currents related to a defined magnetic vector potential in a number of points. This problem translates into an algebraic system:

$$\begin{pmatrix} k_{11} & k_{12} & \dots & k_{18} \\ k_{21} & k_{22} & \dots & k_{28} \\ \vdots & \vdots & \ddots & \vdots \\ k_{n1} & k_{n2} & \dots & k_{n8} \end{pmatrix} \begin{pmatrix} I_{F1} \\ I_{F2} \\ \vdots \\ I_{F8} \end{pmatrix} = \begin{pmatrix} A_{\Phi 1} \\ A_{\Phi 2} \\ \vdots \\ A_{\Phi n} \end{pmatrix} \tag{4.13}$$

To have a regular solution inside the domain D, the number of points n of evaluation of the magnetic vector potential must be much higher than the number of the field shaping coils (8 in this case); $n \gg 8$ means that the solution will be evaluated with the least squares method.

The total magnetic vector potential is a linear combination of A' and A'', so the solution for 4.11 is one of the infinite solutions for the problem. In addition, this solution is typically not valid for magnetomotive force compensation. Hence, we need to find a solution considering 4.10, which results in a null field inside the domain D. Since this current distribution doesn't interfere with the vertical field, it can be scaled with a coefficient to have a total current (plasma + FF coils) equal to zero:

$$I_P = 48 \sum I'_F + k \cdot 48 \sum I''_F \tag{4.14}$$

Hence, the scaling coefficient for the magnetomotive force compensation will be:

$$k = \frac{I_P - 48 \sum I'_F}{48 \sum I''_F} \tag{4.15}$$

We can thus write the vector of FS currents as:

$$I_F = I'_F + k \cdot I''_F \tag{4.16}$$

The vector of coefficients which correlates the plasma current and the field shaping currents can thus be defined as the ratio between the FS currents defined in 4.16 and the flat-top plasma current:

$$\mathrm{K} = \frac{I_F}{I_P} \tag{4.17}$$

Given this, we can rewrite the system of equations defined in 4.1 by substituting the field shaping current with $I_F = K I_P$. The unknown terms now reduce to 2 (I_P and I_M), since

I_F can be obtained using the coefficient in 4.17.

$$\begin{cases} V_M = L_M \frac{di_M}{dt} + (M_{MF}K + M_{MP})\frac{di_P}{dt} + R_M i_M \\ V_{LOOP} = -R_P i_P = M_{PM}\frac{di_M}{dt} + (M_{PF}K + L_P)\frac{di_P}{dt} \end{cases} \tag{4.18}$$

in 4.18, plasma is considered as short-circuited, and the resistive voltage drop is referred as V_{LOOP}.

$$\begin{bmatrix} L_M & M_{MF}K + M_{MP} \\ M_{PM} & L_P + M_{PF}K \end{bmatrix} \begin{bmatrix} \frac{di_M}{dt} \\ \frac{di_P}{dt} \end{bmatrix} + \begin{bmatrix} R_M & 0 \\ 0 & 0 \end{bmatrix} \begin{bmatrix} i_M \\ i_P \end{bmatrix} = \begin{bmatrix} V_M \\ V_{LOOP} \end{bmatrix} \tag{4.19}$$

The inductance matrix is subdivided as follows:

$$\left[\begin{array}{c|c|c} L_M & M_{MF} & M_{MP} \\ \hline M_{FM} & L_F & M_{FP} \\ \hline M_{PM} & M_{PF} & L_P \end{array}\right] \tag{4.20}$$

Where:

- L_M is a 4×4 matrix
- M_{MF} is a 4×8 matrix
- M_{MP} is a 4×1 vector
- M_{MF} is a 8×4 matrix
- L_F is a 8×8 matrix
- M_{FP} is a 8×1 vector
- M_{PM} is a 1×4 vector
- M_{PF} is a 1×8 vector
- L_P is a scalar

Considering the reduced matrix in 4.19:

- L_M is a 4×4 matrix
- $M_{MF}K + M_{MP}$ is a 4×1 vector

- M_{PM} is a 1×4 vector
- $L_P + M_{PF}K$ is a scalar

Since V_M is defined as in 4.4, the voltage vector in 4.19 becomes the following:

$$\begin{bmatrix} V_M \\ V_{LOOP} \end{bmatrix} = \begin{bmatrix} -V_{oct} \\ -V_{oct} \\ -V_{oct} \\ -V_{oct} \\ V_{LOOP} \end{bmatrix} \tag{4.21}$$

Referring to eq. 4.6, the $-V_{oct}$ terms can be moved to the left-hand side and incorporated in the resistance matrix as following:

$$\begin{bmatrix} R \end{bmatrix} = \begin{bmatrix} R_M & 0 \\ 0 & 0 \end{bmatrix} + \frac{R_T}{4} \left[\begin{array}{cccc|c} 1 & 1 & 1 & 1 & -\frac{1}{48} \\ \hline 1 & 1 & 1 & 1 & -\frac{1}{48} \\ \hline 1 & 1 & 1 & 1 & -\frac{1}{48} \\ \hline 1 & 1 & 1 & 1 & -\frac{1}{48} \\ \hline 0 & 0 & 0 & 0 & 0 \end{array}\right] \tag{4.22}$$

Hence, the system of differential equations now becomes:

$$\overline{L}\dot{I} + \overline{R}I = V \tag{4.23}$$

With the matrix $\overline{R}$ described as in 4.22, $V = [0, 0, 0, 0, V_{LOOP}]^T$ and the initial conditions defined as a vector $I_0 = [I_{M0}, I_{M0}, I_{M0}, I_{M0}, 0]^T$.

4.2 Equivalent circuit for RFX-mod scaling

Once the validity of the RFX-mod equivalent circuit is established, another equivalent circuit for the analysis of multi-mega ampere machines needs to be defined, under the design constraints defined by possible operating scenarios. One of the most important points is that the machine should maintain the typical RFP configuration advantages, such as the compactness and the mechanical and electrical simplicity, with respect to the Tokamak and Stellarator configurations.

4.2.1 Simplifications due to design constraints

One of the characteristics of the new machine must be the possibility to work with a high duty cycle, hence a short dwell time. For steady-state or nearly steady-state operations, the choice for the ohmic heating coils needs to be based on superconductive materials; thus, a cryostat is required to maintain the superconductive OH winding below the critical temperature. The field shaping winding shall be maintained as close as possible to the vessel, in order to reduce the volume to be magnetised and to guarantee compactness; to fulfil these requirements, the choice needs to shift towards a copper winding, to avoid the cryostat loading gauge. This means that the FS winding cannot achieve both the MMF compensation and the control of the plasma position as in RFX-mod, but will be designed only for the application of a vertical field to control the plasma stability.

As said in the previous section, the FS winding in RFX-mod basically produces the counter EMF, other than the equilibrium field; this translates in the fact that the OH winding acts as the magnetizing winding of a transformer, being not directly influenced by the back EMF produced by the plasma. So, the ampere-turns compensation essentially reduces the flux (relative to the OH winding) needed to bring the plasma current to the desired value. So, not having a MMF compensation is quite a drawback, but also a necessary trade-off to guarantee the machine compactness when operating in quasi steady state conditions.

Without MMF compensation, the equivalent circuit to study the scaling of RFX-mod can be drastically simplified. In fact, if we consider the scheme without the FS winding and the transfer resistances, the four sectors S_1, S_2, S_3 and S_4 can be considered as a single winding coupled with the plasma. Thus, if the resistance of the OH winding is considered to be negligible, the system (fig. 4.4) can be described by a simple set of differential equations (eq. 4.24).

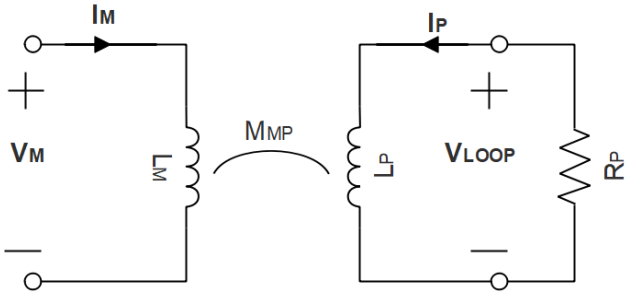

Figure 4.4: Simplified equivalent circuit for the scaling of RFX-mod

$$\begin{cases} V_M = L_M \frac{di_M}{dt} + M_{MP} \frac{di_P}{dt} \\ V_{LOOP} = M_{PM} \frac{di_M}{dt} + L_P \frac{di_P}{dt} \end{cases} \tag{4.24}$$

In matrix format:

$$\begin{bmatrix} L_M & M_{MP} \\ M_{PM} & L_P \end{bmatrix} \begin{bmatrix} \frac{di_M}{dt} \\ \frac{di_P}{dt} \end{bmatrix} = \begin{bmatrix} V_M \\ V_{LOOP} \end{bmatrix} \tag{4.25}$$

Of course this is not a very precise method to evaluate the current profile in a real configuration, but the objective is to define a simple model which can give informations about the achievable performances in terms of flux swing, electric field, flat-top duration and flat-top plasma current; these are the key parameters which will help to define the best configuration between several possible geometries. When a geometry will be defined, more accurate studies can be carried out to precisely define the electrical network and the power supply system, but since that point, a very simple model represent a good trade-off to obtain the desired informations.

The physicist's [and Engineer's, I must add] greatest tool is his waste basket.

Albert Einstein

5 Tools for the numerical simulations

The objective of this thesis is to link the geometric and electric parameters given as an input to the output functions that we want to evaluate and optimize, such the magnetic field and the current transients. To calculate the needed parameters, to obtain the output and to analyse the results, four tools are required:

- A tool to calculate the self and mutual inductances, given the windings geometric parameters
- A tool to compute the magnetic field, given the windings geometric and electric parameters
- A tool to solve the system of differential equations
- A tool to minimize the functions subject to constraints

The first two tools will be extensively described, as they have been fully developed in MATLAB starting from the reference articles, whereas the last two are MATLAB built-in functions, so they will be briefly outlined.

5.1 Tool for the inductance calculation

The system which describes the coupling between the poloidal circuits and the plasma, contains resistive and inductive parameters grouped in a resistance matrix R and an inductance

matrix L. The resistive terms are defined and part of the input, such as the transfer resistance R_T, or can be easily calculated, as the windings resistance. This second term can be neglected, if the considered conductors are superconductive. The inductive terms, instead, strongly influence the dynamic of the plasma current and the poloidal windings current, thus a precise tool is needed to evaluate the self and the mutual inductance for the set of poloidal coils. Since the position and the number of turns will be changed for each step of the optimization to minimize the constrained parameters, also the computational time is a crucial factor.

5.1.1 Inductance calculation of coaxial circular coils with rectangular cross section

For the calculation of the inductances of circular coils with rectangular cross section and uniform current density in air, integral formulations are preferred with respect to FEM analysis, because of their efficiency and accuracy.

Several integral formulations for the computation of auto and mutual inductances have been described throughout the years, using different approaches such as Bessel functions or elliptic integrals. The presented formulation has been compared with all the other methods developed until now, showing the best performances in terms of computational speed and stability (fig. 5.1), especially for geometries typical of superconductive coils.

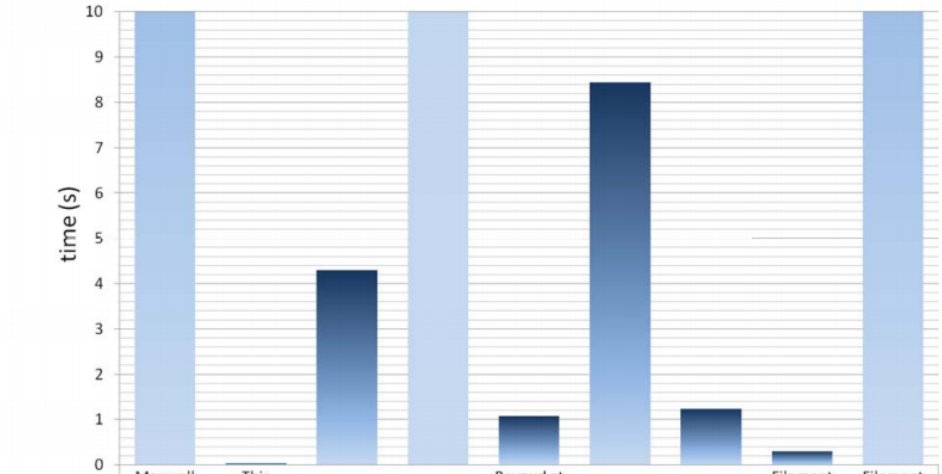

	Maxwell 16.0	This method	Babić et al.	Conway	Ravaud et al.	Hurley et al.	Ren et al.	Filament N=25	Filament N=400
M (μH)	3.958910	3.958910	3.958910	3.958910	3.958910	3.958909	3.958908	3.958882	3.958908
Time (s)	59	0.03	4.30	578.5	1.08	8.44	1.23	0.30	57.23
Times slower	1967	1	143	19283	36	281	41	10	1908

Figure 5.1: Comparison of accuracy and computational time

The mutual inductance is calculated by means of the expression:

$$M = \frac{\mu_0 N_1 N_2}{(R_2 - R_1)(Z_2 - Z_1)(R_4 - R_3)(Z_4 - Z_3)} Q \tag{5.1}$$

Where:

$$Q = \int_{\varphi=0}^{\pi} \int_{Z_1}^{Z_2} \int_{Z_3}^{Z_4} \int_{R_1}^{R_2} \int_{R_3}^{R_4} \frac{rR\cos(\varphi) dR dr dZ dz d\varphi}{\sqrt{r^2 + R^2 - 2Rr\cos(\varphi) + (z - Z)^2}} \tag{5.2}$$

With the coordinates defined as in fig. 5.2 and N_1, N_2 the number of turn of the two coils.

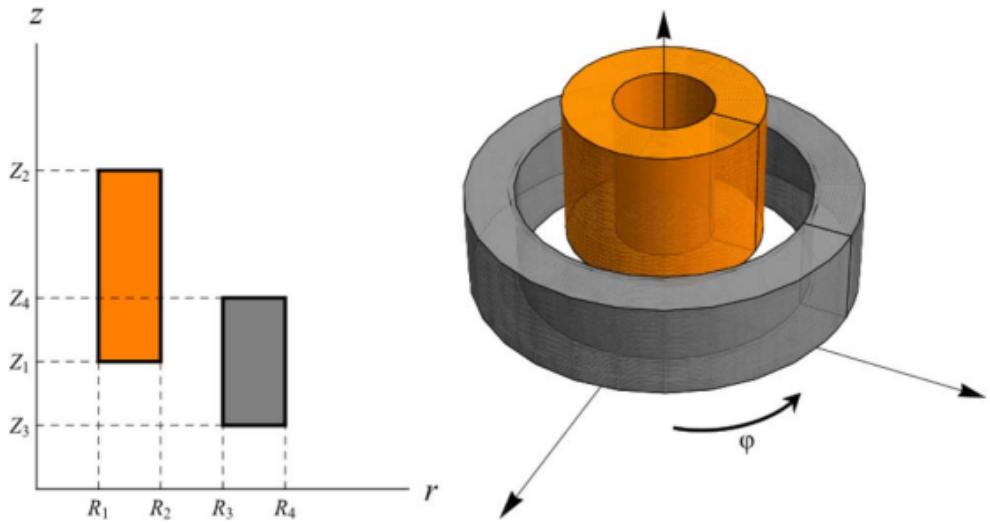

Figure 5.2: Reference system for coaxial coils

In the reference article, the expression of 5.2 is analytically integrated with respect to r,R,z,Z obtaining:

$$Q = \int_{\varphi=0}^{\pi} G[R_1, R_2, R_3, R_4, Z_1, Z_2, Z_3, Z_4, \varphi] \cos\varphi d\varphi \tag{5.3}$$

The expression for Q is quite complicated and will be described in the appendix, although, despite the complexity of the formula, this method allows the Q function using a one-dimensional integration; this results in high performances for the computational speed, as seen in fig. 5.1.

However, singularities are present in the Q function; this leads to the necessity of an analysis of the function, to make possible the calculation of auto-inductances and to evaluate Q stability.

5.1.2 Analysis of the Q function singularities

Q is a monotonically decreasing function with singularities in $\varphi = 0$ and $\varphi = \pi$; these singularities can be easily avoided by using a Gaussian quadrature method. However, the function becomes very unstable as it approaches the integration boundaries. A further paper describes a method to correct these instabilities but, since this solution considerably jeopardise the computation speed, a different approach is used to establish whether there is the necessity to perform this correction.

The Q function was evaluated for several test cases, and analysed in proximity of the singularities. As mentioned before, the function becomes highly unstable (fig.5.3).

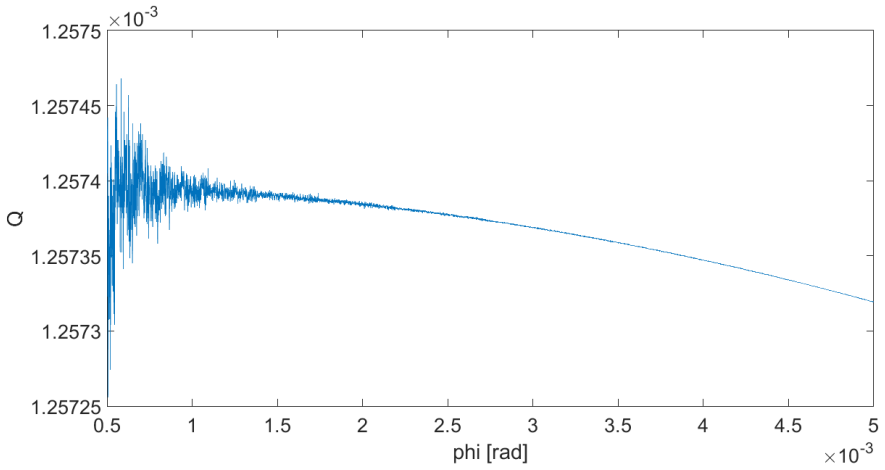

(a) Instability as approaching 0

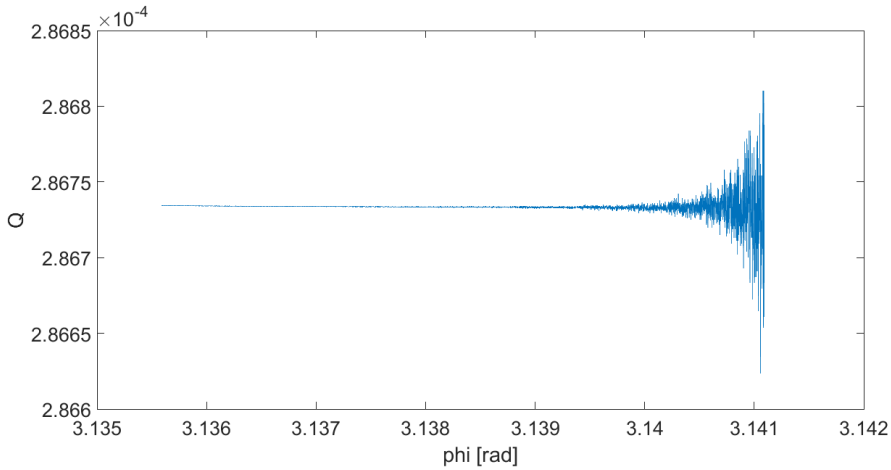

(b) Instability as approaching π

Figure 5.3: Q instabilities in proximity of the singularity points

The procedure to correct the instabilities is based on an iterative process, which is extensively described in the analysis reference article. The method basically consists of two processes:

- Evaluation of the exact value of the function Q at the integration boundaries Q_0 and Q_π
- Iterative process to find φ_0 and φ_π

φ_0 is defined as the value for which the function Q reaches the value Q_0 and falls below Q_0 for $\varphi > \varphi_0$, whereas φ_π is defined as the value for which the function Q reaches the value Q_π

and exceeds Q_π for $\varphi < \varphi_\pi$. Then, the function is interpolated by defining a set of evaluation points, multiples of φ_0 and φ_π. This process, represented in fig. 5.4 essentially reconstructs the function Q to preserve the decreasing trend compromised by numerical instabilities.

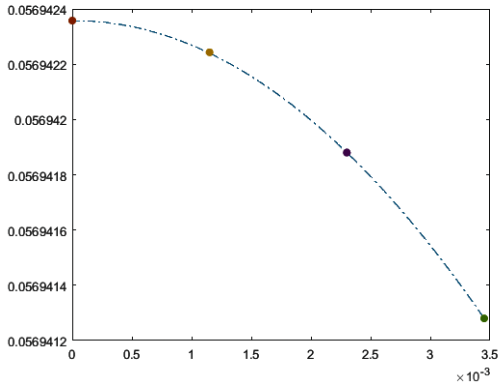

(a) Interpolation of the function in proximity of 0

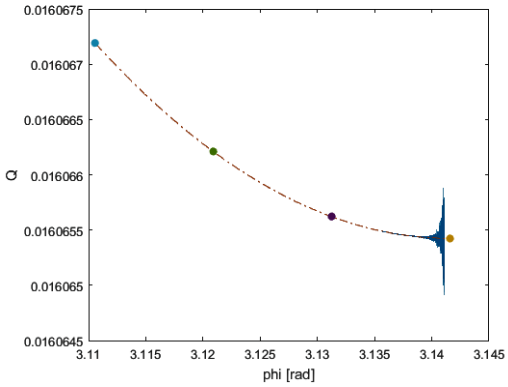

(b) Interpolation of the function in proximity of π

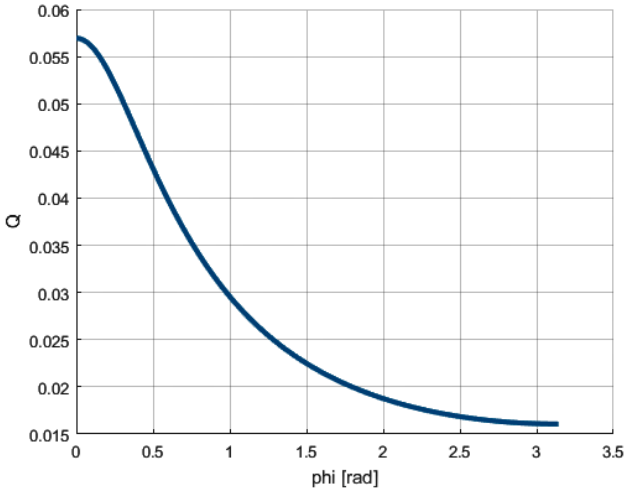

(c) Corrected function Q

Figure 5.4: Correction of Q instabilities

5.1.3 Method comparison

The validation of the algorithm has been carried out considering the benchmark values described in the reference article. The results were also compared with reference values from other methods of inductance calculation. A set of coils with different geometries was considered for the mutual inductance (5.1) and auto inductance (5.1) calculation.

With reference to the fig. 5.2, the parameters of the test coils are resumed in the following tables:

Table 5.1: Mutual inductance test

Case	R1	R2	R3	R4	Z1	Z2	Z3	Z4	N1	N2
1	100	200	300	400	100	200	300	400	100	100
2	500	1500	500	1500	0	1000	1001	2001	1	1
3	87.5	112.5	87.5	112.5	-42.5	-17.5	17.5	42.5	200	200
4	200	400	600	800	-100	100	-100	100	500	500
5	28.7	50.7	28.7	50.7	0	30.2	30.21	60.41	10	10
6	28.7	50.7	28.7	50.7	0	30.2	40	70.2	10	10
7	28.7	50.7	28.7	50.7	0	30.2	65	95.2	10	10
8	100	200	100	200	0	100	200	300	100	100
9	1200	1250	1000	1050	0	250	525	725	100	10

Table 5.2: Auto inductance test

Case	R1	R2	Z1	Z2	N1
1	1	1.5	0.25	-0.25	1
2	1	3	1	-1	1
3	1	4	3	-3	1
4	1	7	6	-6	1
5	1	9	4	-4	1

For the mutual inductances, the result of the comparison is represented in fig 5.5:

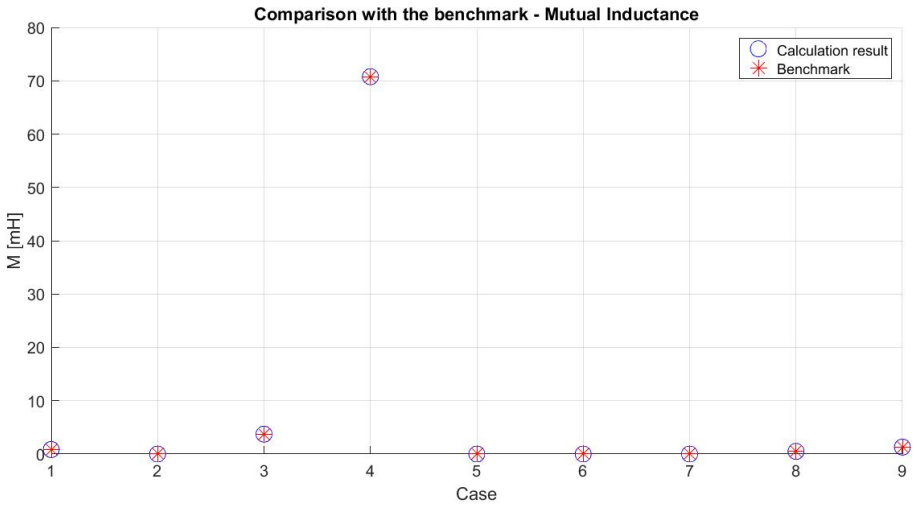

(a) Graphical comparison of the mutual inductances calculation results with the benchmark

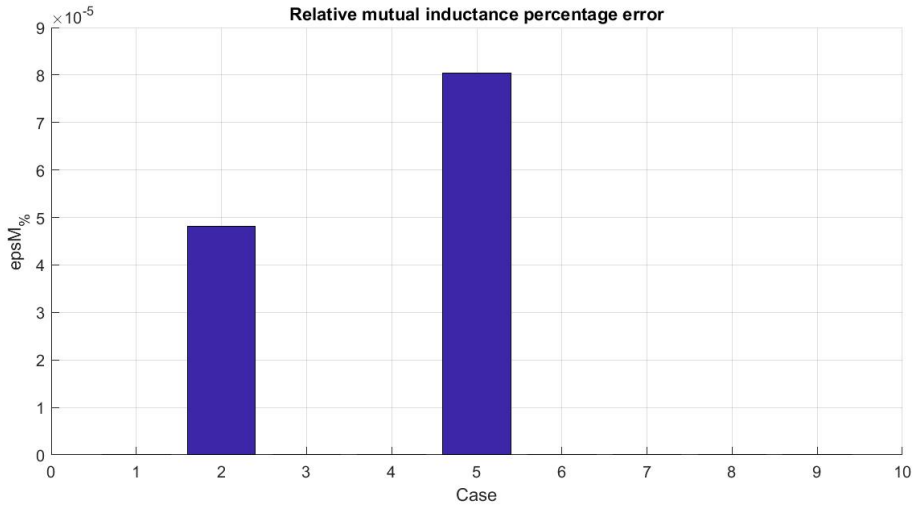

(b) Instability as approaching π

Figure 5.5: Relative percentage error of the mutual inductances calculation with respect to the benchmark

The result of the comparison for self inductances is represented in fig 5.6:

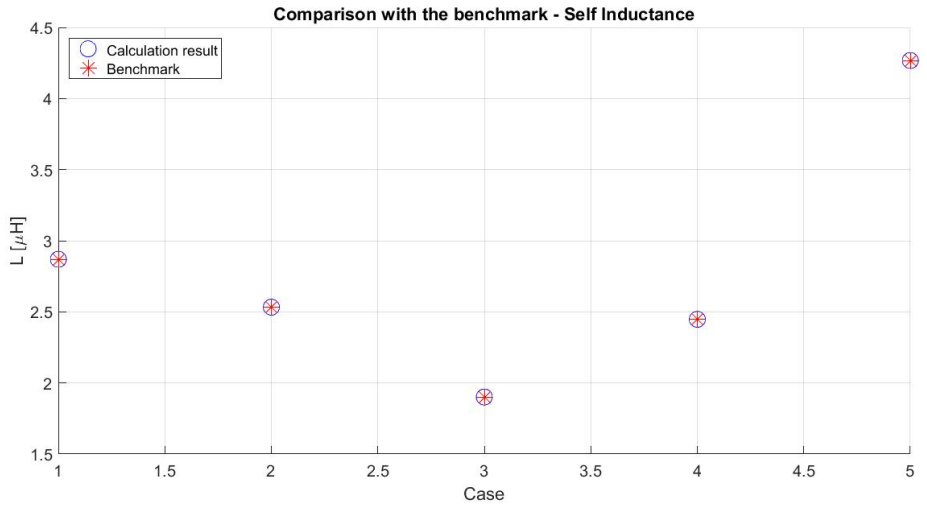

(a) Graphical comparison of the self inductances calculation results with the benchmark

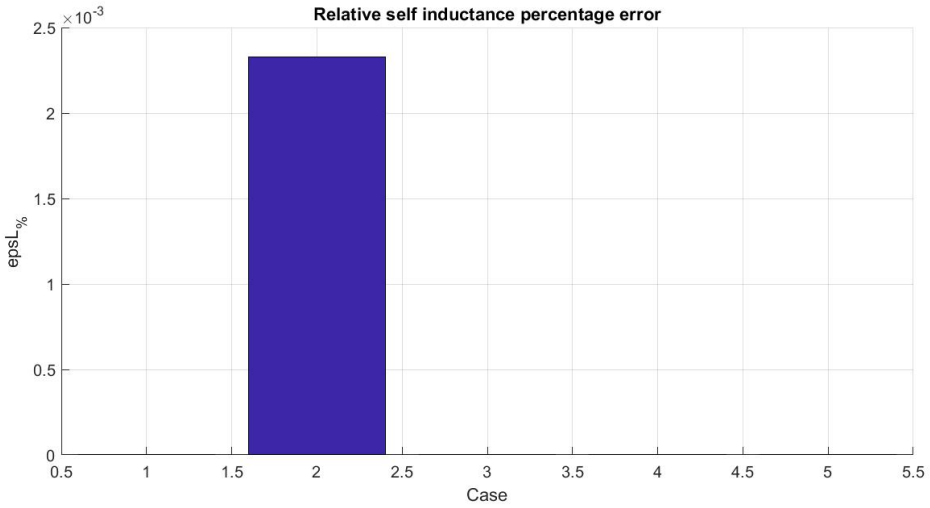

(b) Instability as approaching π

Figure 5.6: Relative percentage error of the self inductances calculation with respect to the benchmark

As one can see, the results are very accurate for a wide range of geometries. Hence, the precision and the computational speed of this method led to the choice of this algorithm for the inductance calculation in this thesis.

5.2 Tool for the magnetic field computation

RFX-mod is the largest operative RFP device, thus some of the components represent the current technological state of the art. Since this thesis is not intended to provide an advanced sizing of the machine, but aims to assess the feasibility of a multi-mega ampere RFP device, too detailed calculations would be pointless as this stage. Nevertheless, a bigger machine implies stronger error fields that need to be compensated via the field-shaping winding; a precise calculation of the error field can thus provide some design constraints for the power supplies and a baseline model for the control scheme.

Also, the use of superconductive windings is essential to sustain minutes-based discharges. A correct evaluation of the magnetic field at the most severely stressed coil surface and internal volume, which is often challenging due to the numerical instabilities in proximity of the source, is essential to ensure the magnetic field to stay within the critic value.

5.2.1 Benchmark for the magnetic field computational tool

When building a new computational tool, the necessity of a reference to evaluate the precision, highlights the need of a benchmark. This can be done by cross-referencing with experimental tests, solid analytic formulations, or already benchmarked numerical codes.

In this case, a benchmarked code has first been confronted with an analytical formulation, to ensure that no syntax errors are present. Then, the definitive algorithm has been compared with the references listed in the article, as well as with the benchmarked code, to evaluate the speed and precision in close proximity to the source.

The analytic formulation is based on the calculation of the magnetic field produced by a current-carrying filamentary circular loop using Biot-Savart law, with respect to the elliptic integrals of first and second order.

The solution with respect to elliptic integrals of the magnetic field, considering an axisymmetric geometry of the source, is:

$$B_r(r,z) = \frac{\mu_0 I}{2\pi r}\frac{z-z_c}{\sqrt{(r+r_c)^2+(z+z_c)^2}}[-K(k)+\frac{r_c^2+r^2+(z-z_c)^2}{(r_c-r)^2+(z-z_c)^2}E(k)] \quad (5.4)$$

$$B_z(r,z) = \frac{\mu_0 I}{2\pi}\frac{1}{\sqrt{(r+r_c)^2+(z+z_c)^2}}[K(k)+\frac{r_c^2-r^2-(z-z_c)^2}{(r_c-r)^2+(z-z_c)^2}E(k)] \quad (5.5)$$

Where:

- $k = \sqrt{\frac{4\alpha}{Q}}$
- $Q = (1+\alpha)^2 + \beta^2$
- $\alpha = \frac{r}{a}$

$K(k)$ and$E(k)$ are the complete elliptic integrals of the first and second kind, whereas I, r_c, z_c, a are the current in the wire, the coordinates of its centre and its radius; r, z are the coordinates of a generic point in space, where the field is to be computed.

The benchmarked code is based on this formulation, but it considers a discretization of the rectangular cross-section coil in a number of elements, thus allowing the precise calculation of the field produced by a solid winding, even in the proximity of the surface.

A first test considering a coil with a width of $1m$, a height of $1m$ and a m.m.f. of $10MA$ has been performed. The test was carried out by starting from an evaluation distance of $1m$ from the source, and progressively reducing it. In fig. 5.7, the maximum percentage error on the magnetic field is plotted against the axial distance from the evaluation point and the surface of the coil; one can see that, by approaching the source surface, the wire model becomes more and more imprecise, with respect to the benchmarked one.

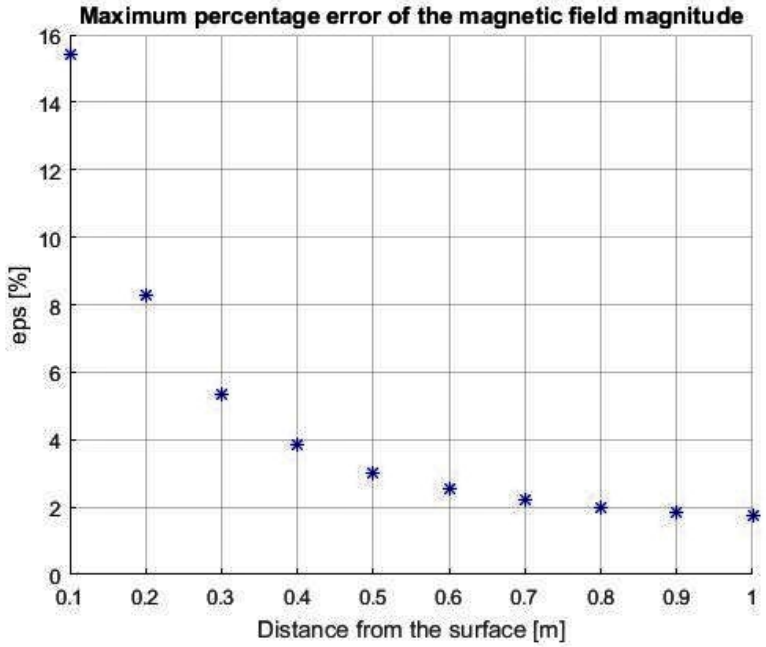

Figure 5.7: Comparison between the filamentary coil formulation and the discretized area formulation - percentage error

This can also be seen by comparing the magnetic field values at a distance from the source of $1m$ and $0.1m$ (fig. 5.8)

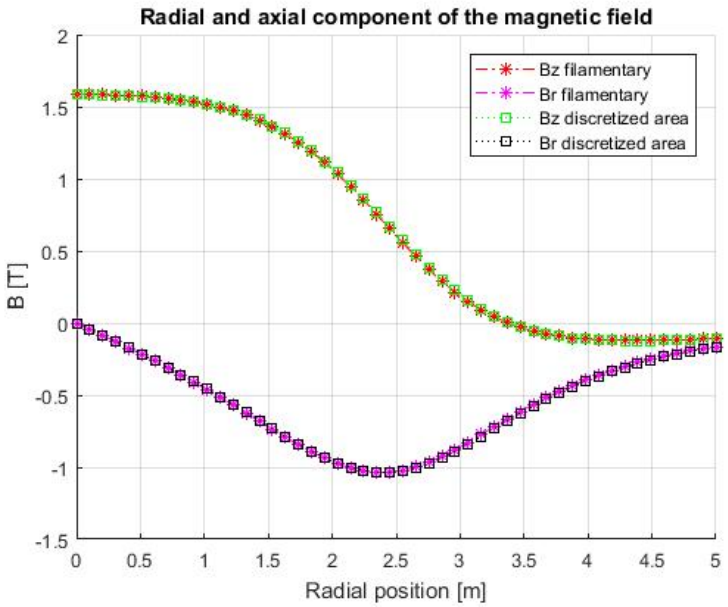

(a) axial distance from the source of $1m$

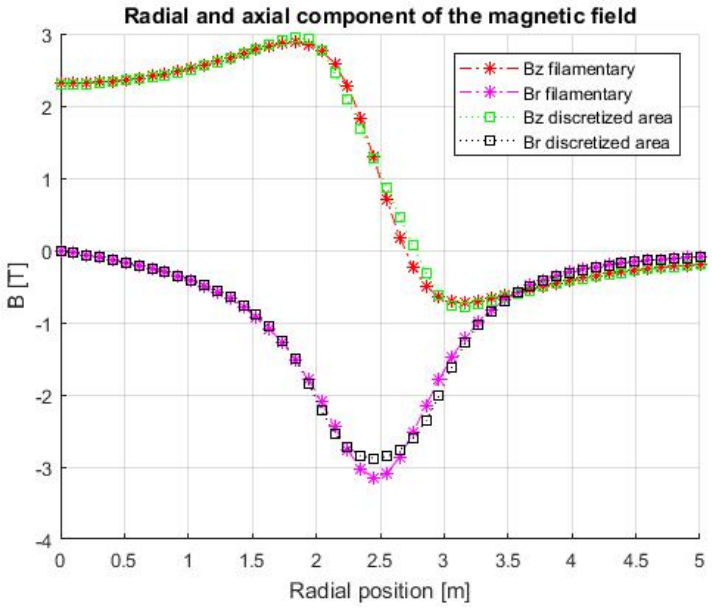

(b) axial distance from the source of $0.1m$

Figure 5.8: Comparison between the filamentary coil formulation and the discretized area formulation - magnetic field values

5.2.2 Algorithm for the computation of magnetic field produced by an arc segment of a conductor with rectangular cross section

This algorithm is based on an analytical exact formulation described by L.K. Urankar, rearranged to obtain a 1-D integrand along the φ coordinate (fig. 5.9).

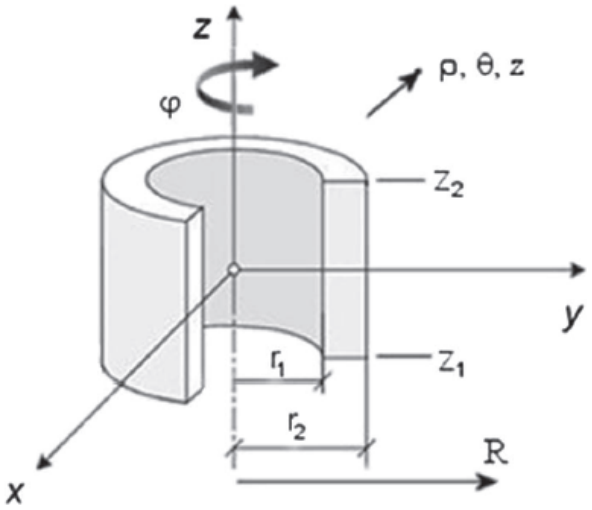

Figure 5.9: Local cylindrical coordinate system

Considering a local cylindrical coordinate system, analytical integrations can be carried out along the R and Z direction, obtaining analytic formulations for the magnetic field components along the three Cartesian directions:

$$Bx = \frac{J\mu_0}{4\pi} \int_{\varphi 1}^{\varphi 2} L_{xy} \cdot \cos(\varphi) d\varphi \tag{5.6}$$

$$By = -\frac{J\mu_0}{4\pi} \int_{\varphi 1}^{\varphi 2} L_{xy} \cdot \sin(\varphi) d\varphi \tag{5.7}$$

$$Bz = -\frac{J\mu_0}{4\pi} \int_{\varphi 1}^{\varphi 2} (L_z + \frac{1}{2} T_1 \cdot \ln(M) + f \cdot R_A) d\varphi \tag{5.8}$$

The terms in 5.6, 5.7, 5.8 will be described in the appendix but, essentially, by knowing the geometric parameters of the conductor and the current density, the magnetic field along the three directions can be calculated. The method present singularities for field points lying on the z-axis, but this can be simply corrected by switching to well-known formulations of the

magnetic field along the z-axis, for axi-symmetric configurations. Other singularities occur when the field is evaluated on the surface, along the φ coordinate; these singularities don't occur in our case, because the magnetic field will be evaluated on a poloidal plane, in fact by exploiting the axi-symmetry, but they can be eliminated by using an adaptive integration, such as the Gauss-Kronrod quadrature. This approach could be used in a second phase, if 3-D computation of fields will be required.

The algorithm presents several advantages:

- Possibility to compute the magnetic field produced both by solenoids with rectangular cross section, and arc-segments of conductors with rectangular cross section
- 3-D calculation of the magnetic field
- Fast and precise computation of the magnetic field, particularly on the surface of the source
- Precise computation of the magnetic field with unfavourable aspect ratios

The first two features allow the study of the magnetic field in a large number of applications, even when limiting to the fusion devices; for example, this tool can be used for the study of the magnetic field produced by poloidal coils, toroidal coils of various shapes and also the complex coils used in Stellarator devices.

The last two features become necessary when the magnetic study is performed on superconductive coils; in fact, a precise evaluation of the field is required in proximity of the sources, to ensure the values to keep within the critical field, and superconductive coils often have very unfavourable aspect ratios.

Since the new conceptual machine will be necessarily based on superconductive windings, due to the duration of the operations, this tool represent an optimal choice for the study of magnetic fields.

5.2.3 Confrontation with test case and with the discretized area formulation tool

A first comparison was made with a test case described in the reference article: an arc of solenoid with an high aspect ratio of 500 is considered. Geometric parameters of the coil are resumed in tab. 5.3.

Table 5.3: Test case

External radius [m]	1
Internal radius [m]	0.5
Height [m]	0.001
Total current [kA]	700
Arc section	$\frac{\pi}{2}$
Evaluation path	radial
ρ [m]	$0 \div 1$
θ	0
z [m]	-0.0005

The magnetic field, evaluated along a radial path at the bottom face of the coil, for the reference case and the implemented code (fig. 5.10), shows a great accordance of results.

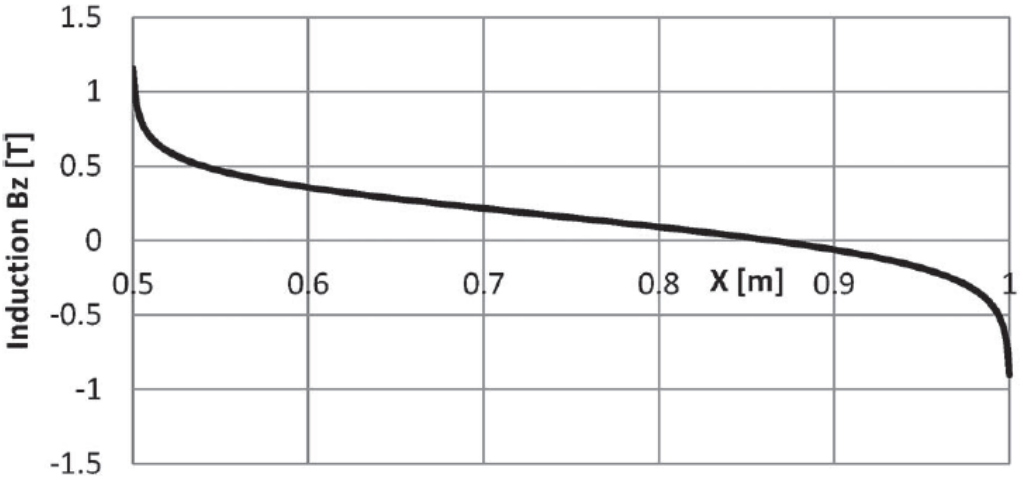

(a) Magnetic field B_z in reference case

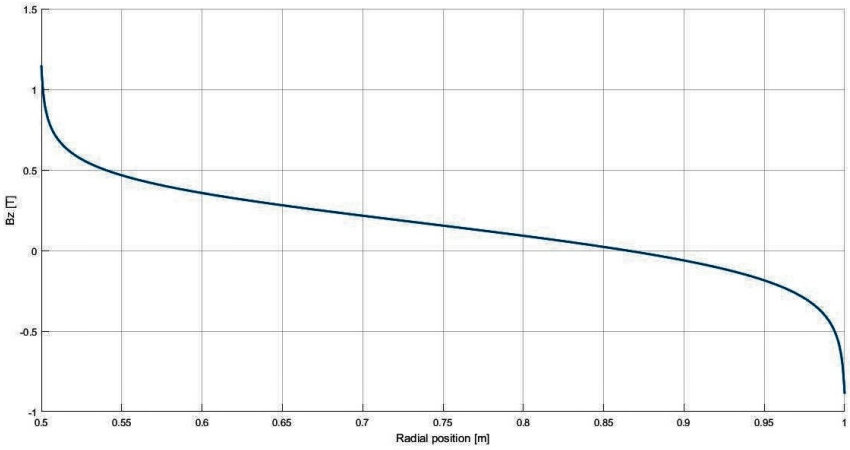

(b) Magnetic field B_z in implemented code

Figure 5.10: Comparison for the reference test case

A second test was carried out, comparing the new implemented code and the code referring to the discretization of the magnetic field source. For this test, a path along the z direction on the internal surface of the coil was taken into consideration. The same coil as the one in the first test is considered, but in this case being a complete solenoid (tab. 5.4)

Table 5.4: Test case 2

External radius [m]	1
Internal radius [m]	0.5
Height [m]	0.001
Total current [kA]	700
Arc section	2π
Evaluation path	vertical
ρ [m]	0.5
θ	0
z [m]	$-0.0005 \div 0.0005$

Moving away from the surface of the coil of $2cm$ and progressively approaching the source (considering an evaluation over a vertical path of the same height), shows how imprecise the solution with the discretized area formulation becomes, with respect to the new algorithm. The maximum percentage error on the modulus of the magnetic field, as the evaluation line approaches the coil surface, is represented in fig. 5.11.

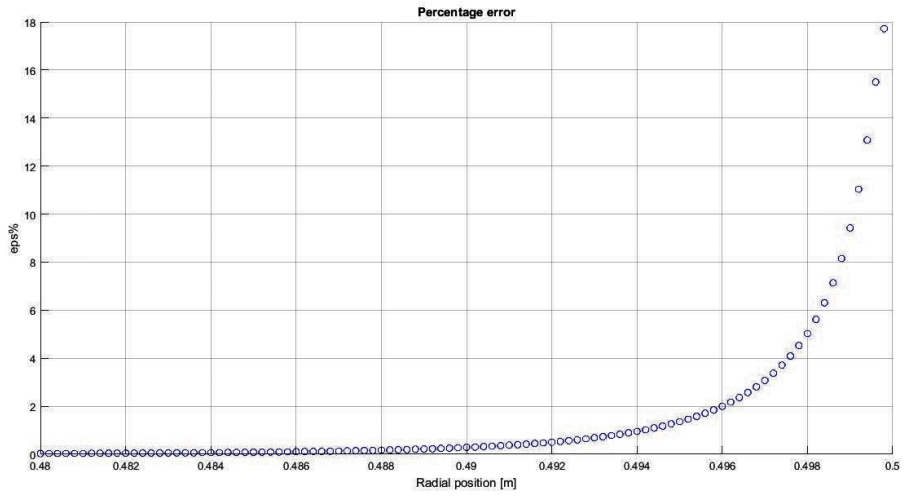

Figure 5.11: Percentage error between the algorithms, as approaching the field source

The difference between the results given by the two methods, can be better visualized in fig. 5.12 and 5.12.

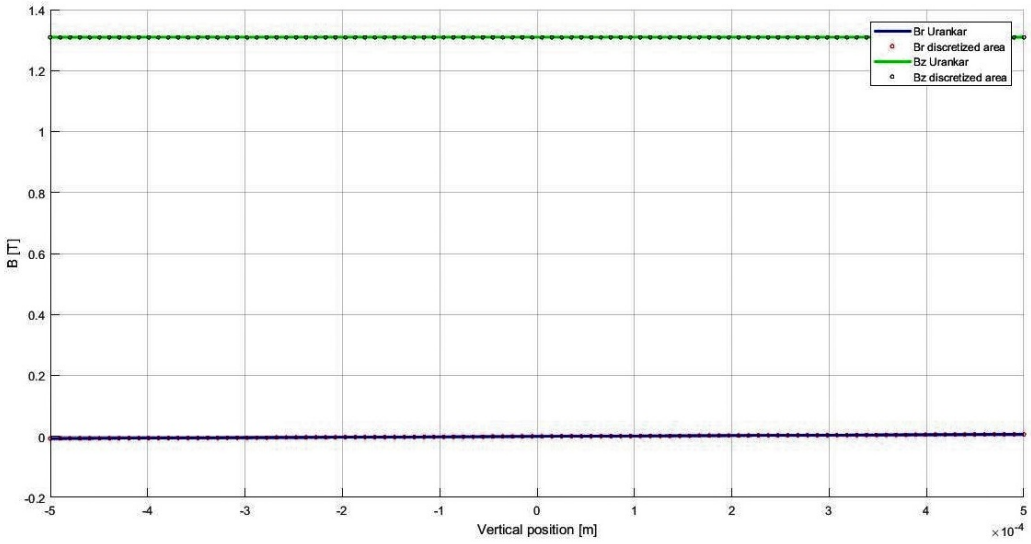

(a) B_r and B_z components comparison at $2cm$ from the surface of the coil

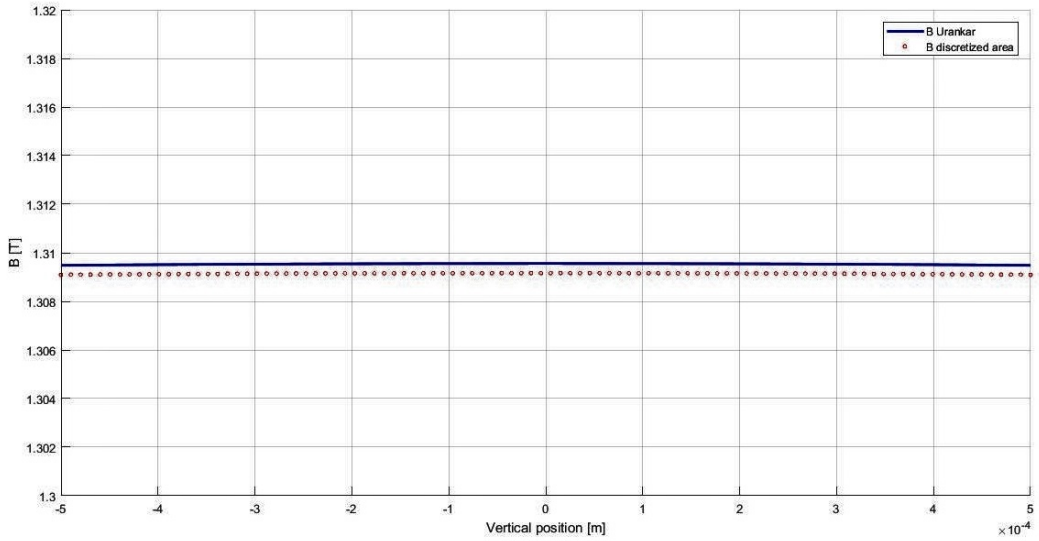

(b) B comparison at $2cm$ from the surface of the coil

Figure 5.12: Comparison between the algorithms at $2cm$ from the magnetic field source

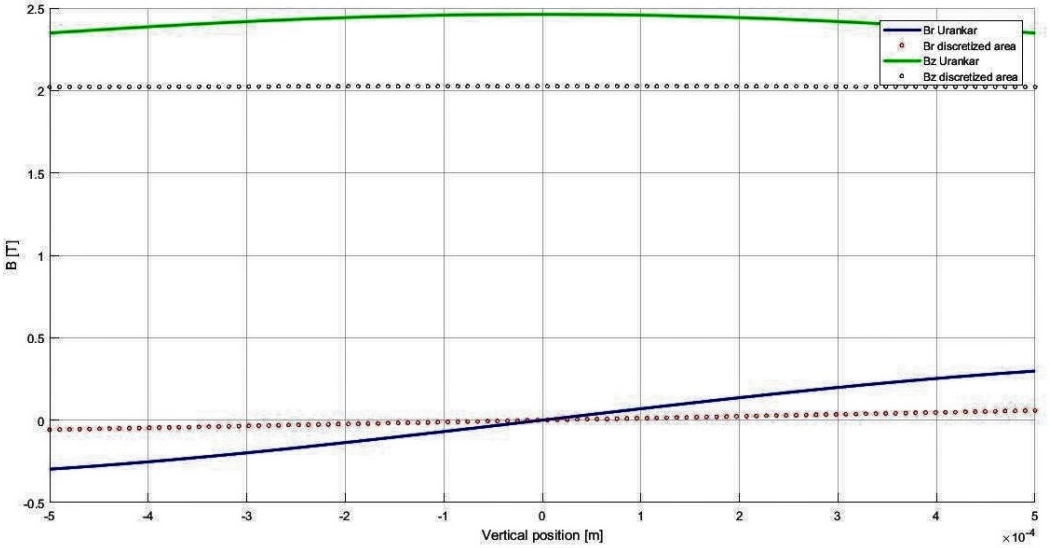

(a) B_r and B_z components comparison on the surface of the coil

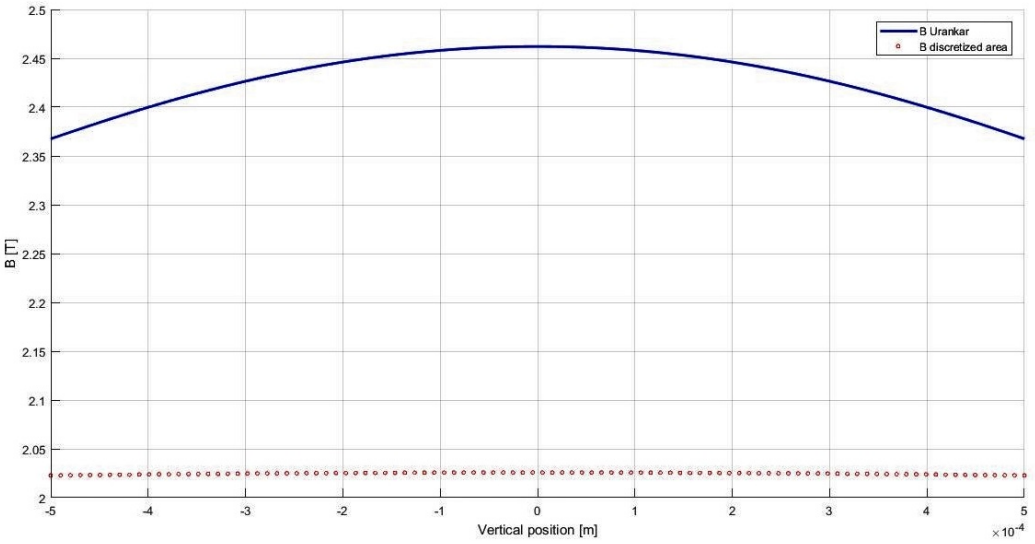

(b) B comparison on the surface of the coil

Figure 5.13: Comparison between the algorithms on the magnetic field source

A third test was made to point out a problem of the tool based on the area discretization, when dealing with coils with large cross-sections. For this test, the computational time is part of the reasoning, hence, also a performance evaluation of the new code was carried out, by establishing the number of points for the Gauss quadrature that guarantee a good stability of the solution. The geometric parameters for the considered coil are resumed in tab. 5.5.

Table 5.5: Test case 3

External radius [m]	5.5
Internal radius [m]	4.5
Height [m]	1
Total current [MA]	10
Arc section	2π
Evaluation path	radial
ρ [m]	$4 \div 6$
θ	0
z [m]	0

By looking at figure 5.14, one can say that the solution surely starts to stabilize after 100 integration points, when the field evaluation points lay on the source surface.

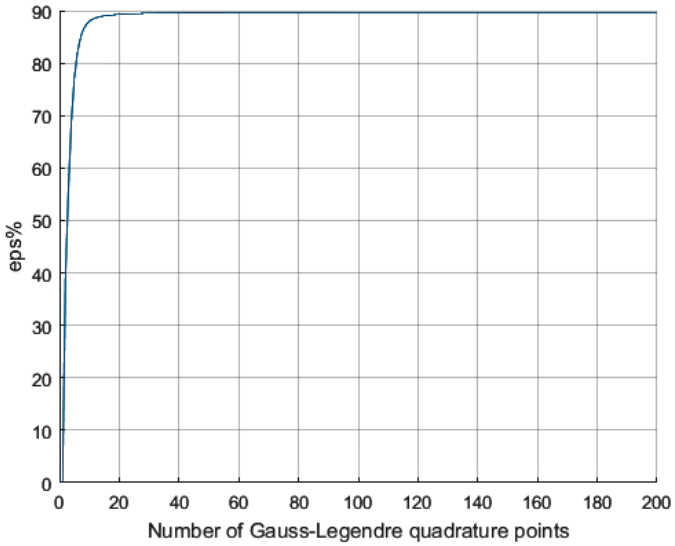

Figure 5.14: Percentage error between the initial solution and the solution with n quadrature points

By taking a closer look (fig. 5.15), we can see that the function is still growing, but the increase of the integration points from 100 to 200, brings a relative percentage variation of just 0.01%. Since the computational time significantly increase from 100 to 200 points, and since this change would bring a negligible effect, the number of quadrature points will be fixed to 100 for the following considerations.

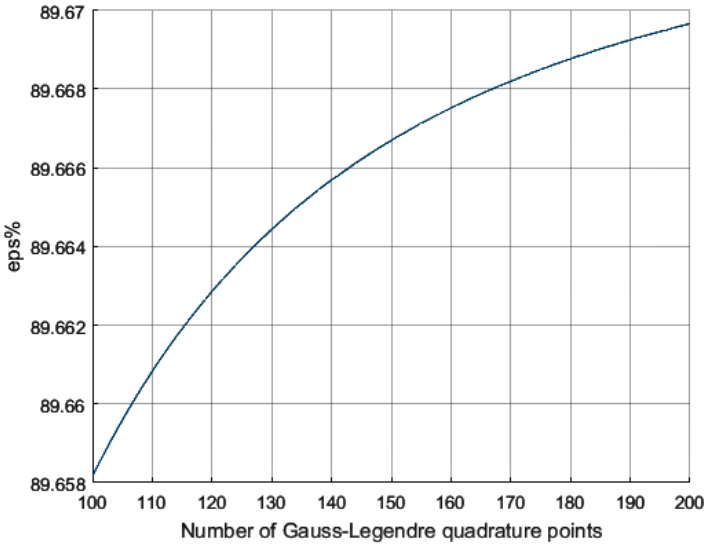

Figure 5.15: Detail of figure 5.14

The algorithm based on Urankar's formulation with 100 integration points, and the algorithm based on the discretized source by a 10×10 grid, led to the following average computational times:

- Urankar approach: $t_{AVG} = 0.055s$
- Discretized area approach: $t_{AVG} = 0.025s$

The second approach is faster, but it lacks on accuracy and stability. In fact, fig. 5.16 shows ten peaks of the solution with the discretized area approach, relative to the boundaries of the discretization grid.

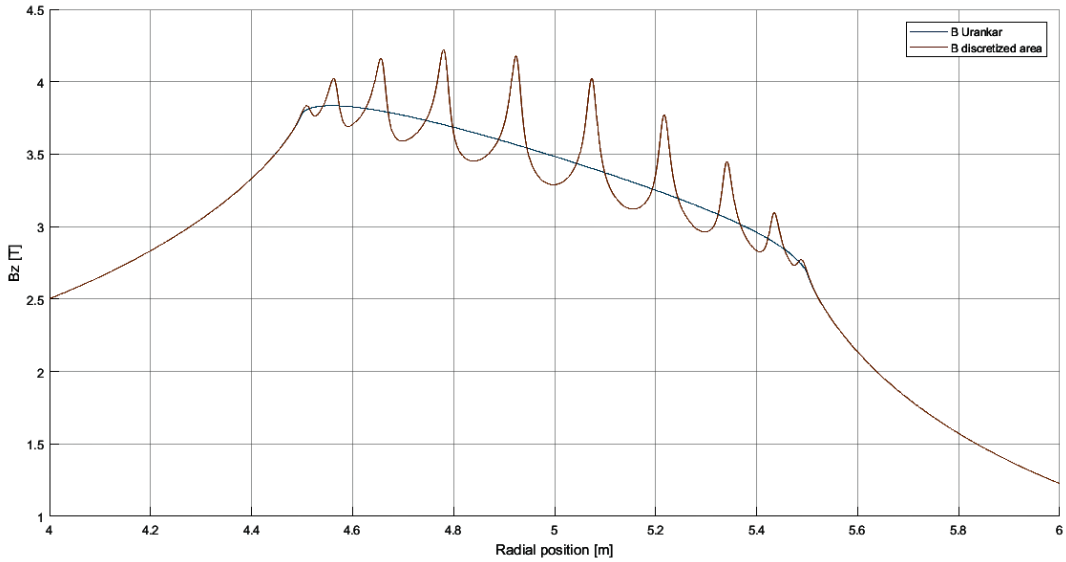

Figure 5.16: Comparison between Urankar and discretized area approaches

To make a correct comparison, the discretization grid for the second approach must be denser; by using a 50×50 grid, the following results are obtained:

- Urankar approach: $t_{AVG} = 0.04s$

- Discretized area approach: $t_{AVG} = 0.55s$

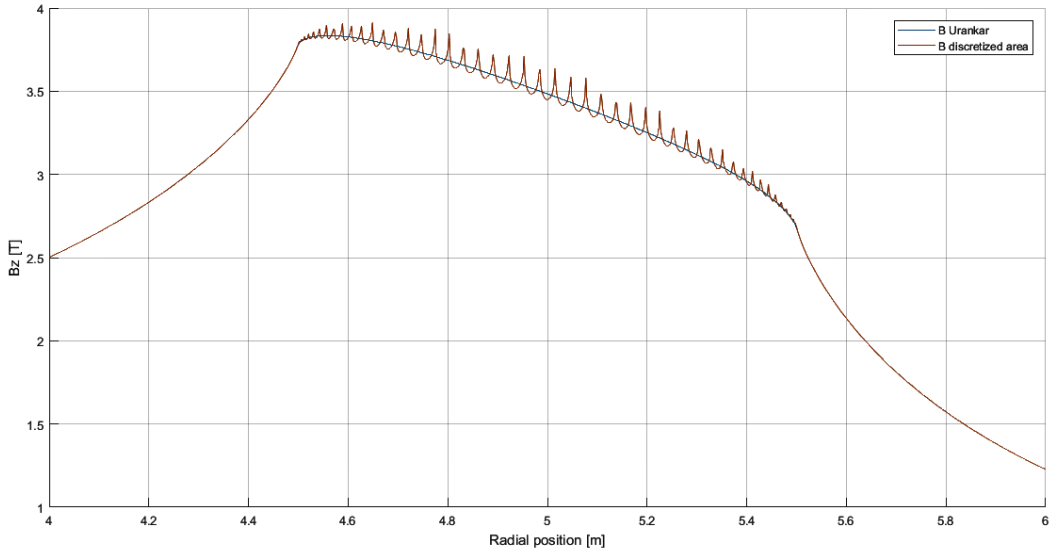

Figure 5.17: Comparison between Urankar and discretized area approaches with a denser grid

As one can see from fig. 5.17, the oscillations are still compromising the precision of the second approach, and the computational time has increased by more than 2000%; this leads to an unacceptable solution in terms of precision and time, with respect to the Urankar approach.

With these tests, we have proven the reliability and efficiency of the new algorithm, hence justifying its choice.

5.3 Tools to solve the differential algebraic equation

The differential algebraic equations defined in 4 have different characteristics, thus they can be solved with different methods.

The system 4.25 contains other two time-dependent variables, V_{LOOP} and V_M; if we consider V_{LOOP} as a constant term and V_M to have constant but different values over three intervals, we can simply solve the system of differential equations by splitting it into three time-intervals. In this case, the derivatives of the currents i_M and iP can be considered linear or constant functions, depending on the relevant interval. The solution will be further described in the next chapter.

Regarding the RFX-mod equivalent circuit 4.3, a set of MATLAB built in functions were used to solve the system of first order differential equations described in 4.18.

5.3.1 ODE solver for RFX-mod equivalent circuit

The tool used to solve the differential algebraic equations describing the RFX-mod equivalent circuit is the MATLAB ODE suit, which contains a number of different solvers useful for both stiff and non-stiff systems. The formulas implemented in these algorithms are the so called "Numerical Integration Formulas", a modification of the backward differentiation formulas. The NDF's are more efficient than the BDF's, considering the achievement of the same A-stability. During the differentiation, the step-size is changed to achieve both efficiency and the required tolerance.

5.4 Tool for the optimization

For the scaling of RFX-mod, two objective functions to be minimized have been defined: the stray field in the plasma area and the maximum field in the central solenoid. These functions have to be minimized, following the criteria described in the next chapter. The tool utilised for this purpose was *patternsearch*, a built-in MATLAB function; this algorithm is based on direct search, a method for solving optimization problems that does not require any information about the gradient of the objective function. A direct search algorithm searches a set of points around the current point, looking for one where the value of the objective function is lower than the value at the current point.

The *patternsearch* algorithm begins at the externally defined initial point. At the first iteration, the direct search algorithm builds a mesh around the initial point, and polls the mesh points by evaluating their objective function. The poll stops as soon as the direct search algorithm finds a mesh point whose fitness value is smaller than that of the current point. After a successful poll, the algorithm expands the current mesh size and polls the mesh points again. When none of the mesh points has a smaller objective function value than the previous one, the algorithm does not change the current point at the next iteration. Instead, it contracts the mesh size and polls again the mesh points in a smaller mesh. The *patternsearch* performs 60 iterations before stopping. In our case, a boundary was defined to avoid overlapping of the coils: for bounds, *patternsearch* modifies poll points to be feasible, meaning to satisfy all bounds.

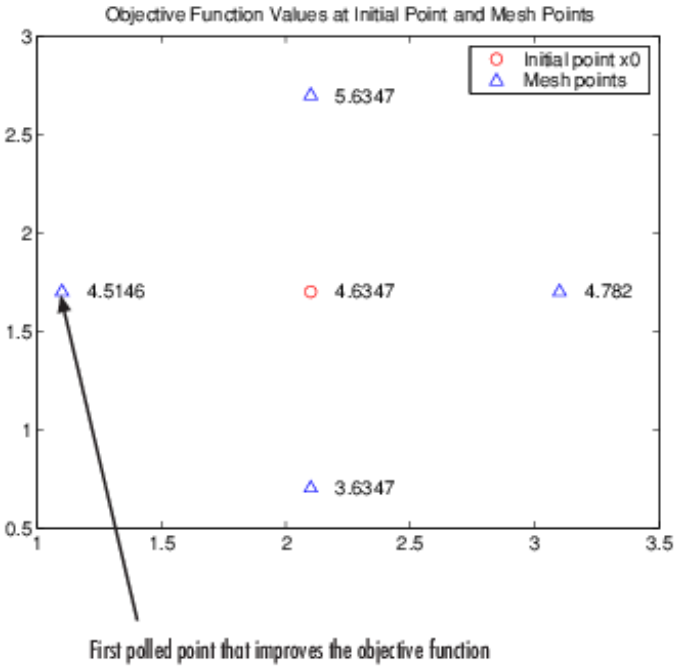

(a) Successful poll

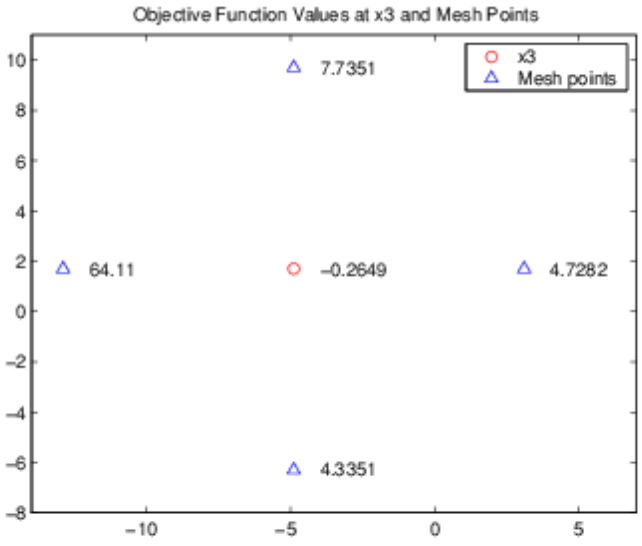

(b) Unsuccessful poll

Figure 5.18: Example of successful and unsuccessful polls

The poll algorithm used for this optimization was a Mesh Adaptive Search (MADS). A MADS poll uses newly generated pseudorandom mesh vectors at each iteration. The vectors are randomly shuffled components from the columns of a random lower-triangular matrix. Unsuccessful polls contract the mesh by a factor of 4, whereas successful polls expand the mesh by a factor of 4. When there is a successful poll, $patternsearch$ starts at the successful point and polls again. This extra poll uses the same mesh vectors, expanded by a factor of 4. The extra poll looks again along the same directions that were just successful.

A truly good book teaches me better than to read it. I must soon lay it down, and commence living on its hint. What I began by reading, I must finish by acting.

Henry David Thoreau

6 Conceptual Design

Once described the problem, some other assumptions and considerations have to be made to define the initial conditions and the sources in equations 4.18 and 4.24.

As seen in 4, the RFX-mod problem and the scaling problem can be treated in two substantially different ways.

6.1 RFX-mod numerical simulations

As previously described, the RFX-mod discharge operations, concerning the PF circuit, can be subdivided into four phases:

1. Charge of the magnetizing winding in order to achieve the desired flux swing
2. Discharge of the magnetizing winding through a transfer resistance (Ramp-up phase)
3. Compensation of the plasma voltage drop through a flux variation imposed by external power supplies (Flat-top phase)
4. Extinction of the plasma discharge through the controlled reduction of the magnetizing winding current (Ramp-down phase)

Since the control of the Flat-top phase is not a subject of this thesis, only the second and the fourth phases will be taken into consideration; in fact, the experimental data considered refers to a free evolution of the system PF winding-Plasma: a flux swing is provided by discharging the OH winding through a transfer resistance, then the system is left to freely evolve.

6.1.1 Initial conditions

We can recall the system of DAEs which describe the RFX-mod equivalent circuit:

$$\begin{bmatrix} L_M & M_{MF}K + M_{MP} \\ M_{PM} & L_P + M_{PF}K \end{bmatrix} \begin{bmatrix} \frac{di_{M1}}{dt} \\ \frac{di_{M2}}{dt} \\ \frac{di_{M3}}{dt} \\ \frac{di_{M4}}{dt} \\ \frac{di_P}{dt} \end{bmatrix} + \begin{bmatrix} R \end{bmatrix} \begin{bmatrix} i_{M1} \\ i_{M2} \\ i_{M3} \\ i_{M4} \\ i_P \end{bmatrix} = \begin{bmatrix} 0 \\ 0 \\ 0 \\ 0 \\ V_{LOOP} \end{bmatrix} \tag{6.1}$$

Where the matrix R is defined as:

$$\begin{bmatrix} R \end{bmatrix} = \begin{bmatrix} R_{M1} & 0 & 0 & 0 & 0 \\ 0 & R_{M2} & 0 & 0 & 0 \\ 0 & 0 & R_{M3} & 0 & 0 \\ 0 & 0 & 0 & R_{M4} & 0 \\ 0 & 0 & 0 & 0 & 0 \end{bmatrix} + \frac{R_T}{4} \left[\begin{array}{cccc|c} 1 & 1 & 1 & 1 & -\frac{1}{48} \\ \hline 1 & 1 & 1 & 1 & -\frac{1}{48} \\ \hline 1 & 1 & 1 & 1 & -\frac{1}{48} \\ \hline 1 & 1 & 1 & 1 & -\frac{1}{48} \\ \hline 0 & 0 & 0 & 0 & 0 \end{array}\right] \tag{6.2}$$

The initial conditions to be defined are thus relative to the OH winding currents and the plasma current. For the experimental discharge considered, the initial current in the four sectors of the magnetizing winding is 40 kA. On the other hand, the initial plasma current is obviously 0. Hence, the initial conditions to be considered are:

$$\begin{bmatrix} i_{M1} \\ i_{M2} \\ i_{M3} \\ i_{M4} \\ i_P \end{bmatrix} = \begin{bmatrix} 40000 \\ 40000 \\ 40000 \\ 40000 \\ 0 \end{bmatrix} \tag{6.3}$$

6.1.2 Sources

As it can be seen in eq. 4.22 and eq. 6.2 , the sources referring to the OH winding have been moved to the left-hand side and incorporated in the R matrix. Hence, the OH winding voltage sources are not required to be defined, thanks to the structure of this particular problem.

The only source that has to be defined is the plasma voltage drop V_{LOOP}, which is not exactly a source, but it represent the plasma resistive voltage drop, defined by the product $R_P(i_P) \cdot i_P$. R_P is time dependent, because it is function of the plasma temperature, hence the plasma current. Experimental results in RFX-mod have shown that the trend of V_{LOOP} during the Ramp-up phase is very difficult to predict, since it depends on many environmental factors and also on the machine conditioning. Also during the Flat-top phase, the V_{LOOP} can be subject to consistent variations from one discharge to the other. A common assumption in the current transient analysis for RFX-mod discharges, is the one that considers the plasma voltage drop to be constant throughout the whole duration of the discharge, apart from the final part of the Ramp-down phase. Since the part of the discharge that we will be evaluating is the Ramp-up phase and part of the Ramp-down, and since the Ramp-up duration is extremely brief with respect to the whole current evolution, the constant V_{LOOP} assumption is a solid one, as it will be seen in the next chapter.

The V_{LOOP} value has been extrapolated from experimental results, considering the mode of a large set of discharge data. The voltage drop considered is $V_{LOOP} = -20$V, hence, the right-hand side of 6.1 can be rewritten as:

$$\begin{bmatrix} 0 \\ 0 \\ 0 \\ 0 \\ V_{LOOP} \end{bmatrix} = \begin{bmatrix} 0 \\ 0 \\ 0 \\ 0 \\ -20 \end{bmatrix} \tag{6.4}$$

6.1.3 Modelling of RFX-mod

RFX-mod has been modelled by taking advantage of the axisymmetry of the configuration, thus by considering a poloidal cross section of the machine. Another consideration that lighten the computational cost is that the PF-winding configuration is symmetric with respect to the radial axis, and that the symmetric coils are connected in series. Given this, the computational costs that derive from the calculation of the inductances and the magnetic field can be consistently reduced.

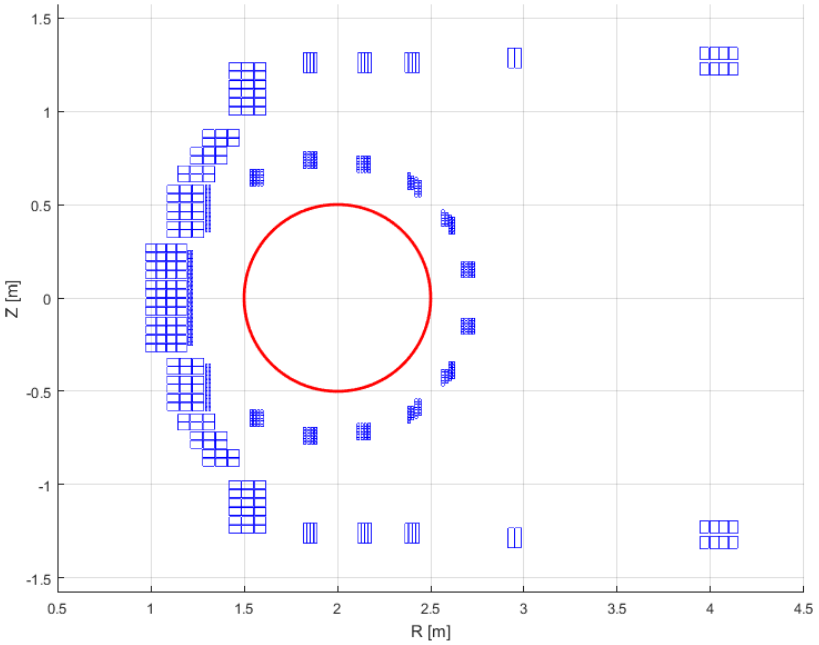

(a) Representation of RFX-mod

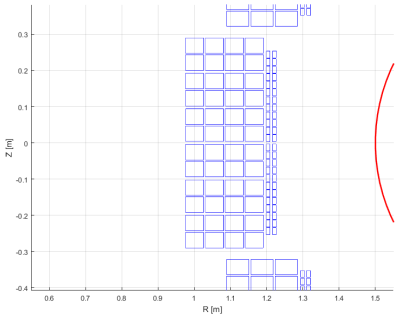

(b) Detail of the OH and FS windings representation

Figure 6.1: RFX-mod geometry representation

As it can be seen in fig. 6.1, each coil of the OH and FS winding has been represented to improve the precision of the inductances and the magnetic field calculations.

Hence, for the calculation of the self and mutual inductances, each single coil has been considered. Then, the terms relative to each section have been summed, leading to the inductance matrix described in 6.1. For the calculation of the plasma mutual inductances, a single conductor in the position of the plasma centroid has been considered.

The same has been done for the calculation of the magnetic field, so the contribution of each coil has been summed to obtain the total magnetic field in a set of points. These calculations have been used to determine the flux map of the OH winding and the FS winding. As it can be seen in fig. 6.2, the OH winding is well-coupled with the plasma, since the magnetic flux is practically null inside the plasma area. In the other figure, the magnetic flux relative to the FS winding is represented; it can be noted that this field is vertical, since a radial force to re-establish an equilibrium position for the plasma is needed.

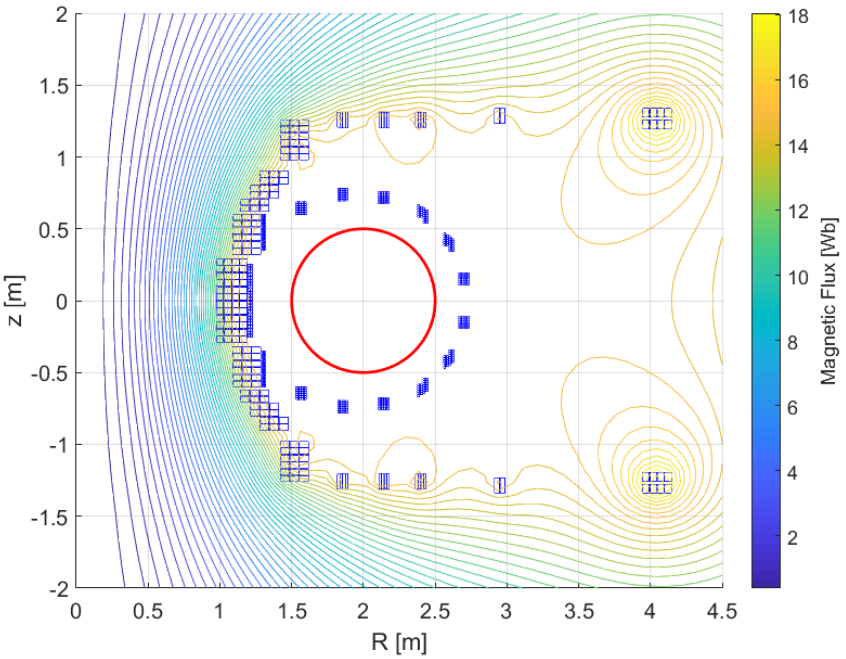

(a) OH winding flux map

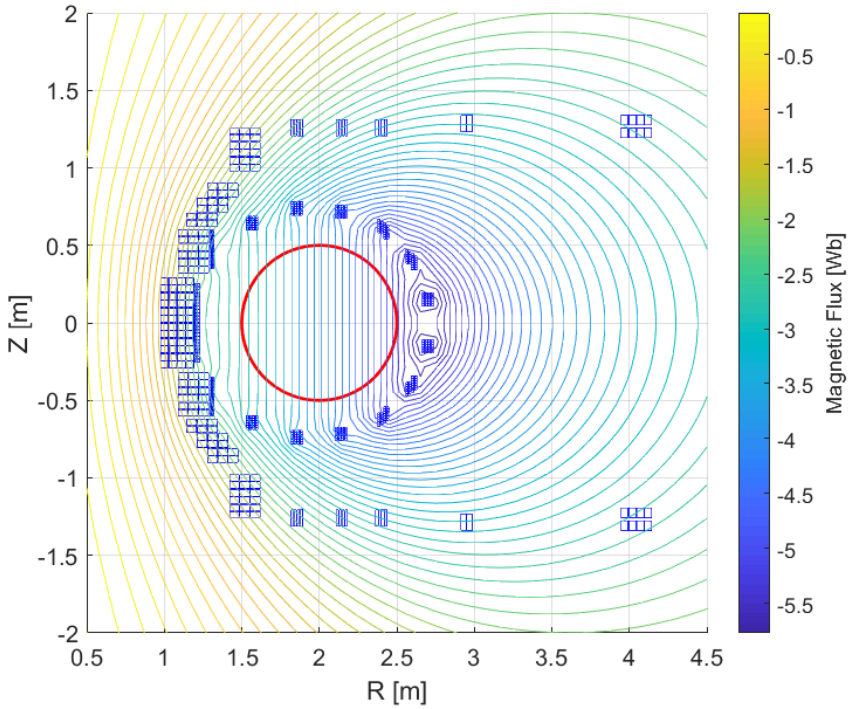

(b) FS winding flux map

Figure 6.2: RFX-mod flux map

6.1.4 Comparison with experimental results

The following experimental discharge has been considered for this evaluation:

- $i_{M0} = 40kA$
- $i_{P\,F-T} = 1.45MA$

With the initial conditions and the sources defined as in the previous sections, we obtained the following results for the Plasma current I_P and the OH winding current I_M:

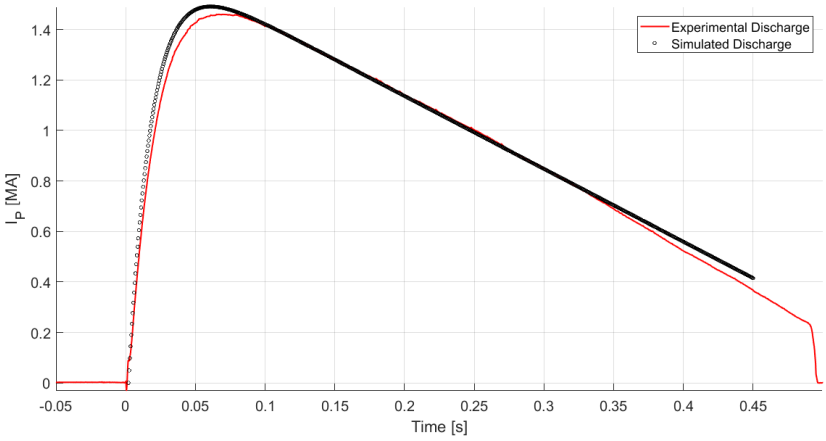

(a) Plasma current

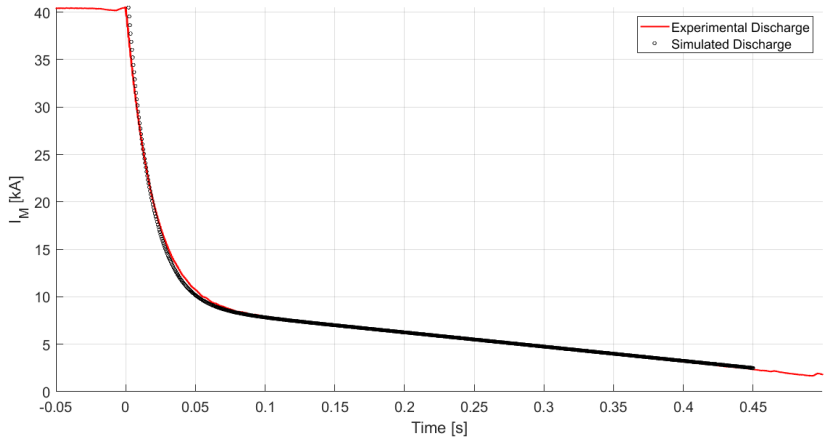

(b) OH winding current

Figure 6.3: Comparison of I_P and I_F with an experimental RFX-mod discharge

Whereas, by considering the numeration described in fig. 6.4 for the FS winding coils.

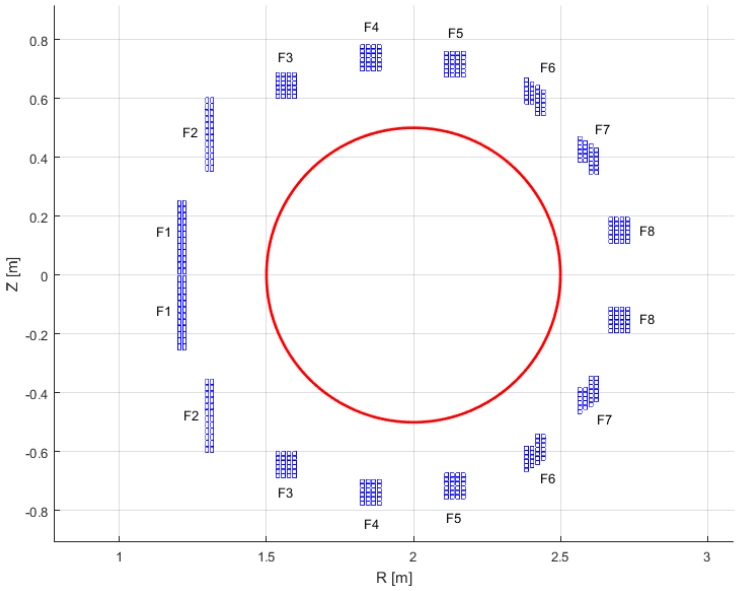

Figure 6.4: Numeration of the RFX-mod FS coils

We obtained the following I_F currents:

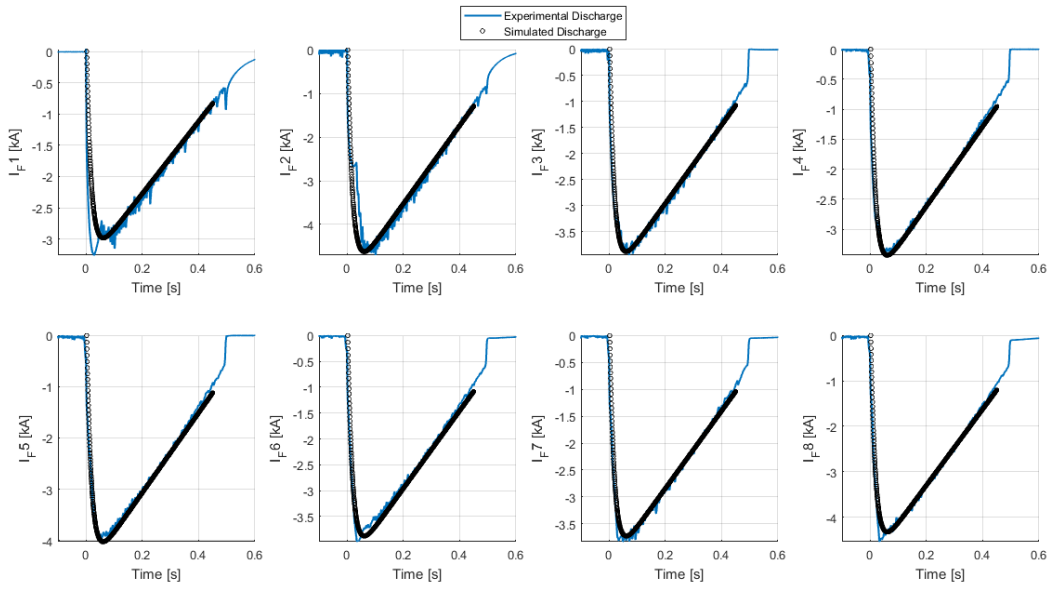

Figure 6.5: Comparison of I_F with an experimental RFX-mod discharge

6.2 Conceptual reactor numerical simulations

The basic operations of a RFP machine can be subdivided into three phases:

1. Ramp-up
2. Flat-top
3. Ramp-down

Unlike RFX-mod, the OH winding is not designed to be discharged through a transfer resistance during the Ramp-up phase; instead, after bringing the magnetizing current to the maximum value, a power supply with a reverse voltage will be connected to the OH winding, thus directly controlling the flux swing during the Ramp-up. This will result in high solicited power supplies and extreme performances requested from the solid state converters. This will be one of the main technological issues for this conceptual machine, but since it will probably be constructed not earlier than ten years from now, the current technological issues are not considered as excessive limitations or design constraints.

6.2.1 Initial conditions

As in the previous problem, the initial conditions to be defined are the plasma current and the magnetizing current at the beginning of the discharge. The initial conditions for each scaling have been established through iterations to guarantee both an effective exploitation of the machine and the achievement of a limited stray field. The results for each case will be described in the next chapter in terms of total Magneto-Motive Force (MMF).

The level of utilisation of the machine can be expressed in terms of the maximum field in the superconductive magnets. In fact, once the current density and the temperature are defined, the performances of the machine are limited by the critical magnetic field of the superconductor. In a superconductor, the magnetic field (B), the temperature (K) and the current density (J) must be maintained below the critical surface in order to retain superconductivity (fig. 6.6).

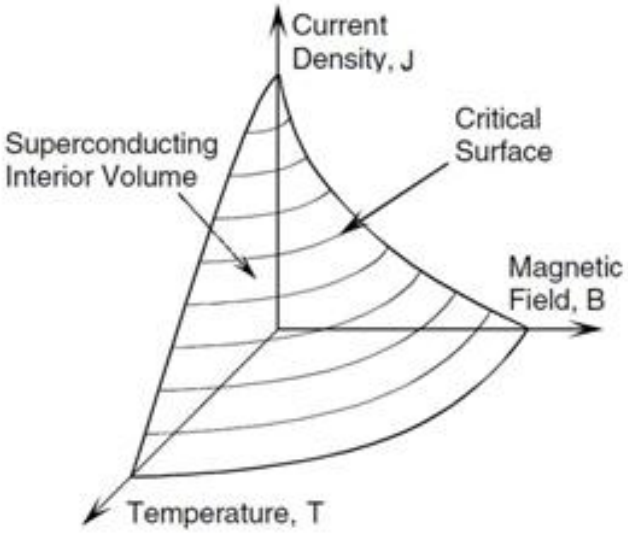

Figure 6.6: Superconductor critical surface

For preliminary considerations on this RFP machine, the superconductors considered are those constituting the ITER central solenoid. The operating conditions and the characteristics of these superconductive coils are resumed in tab. 6.1.

Table 6.1: Operating parameters of ITER central solenoid coils

Superconductor material	Nb_3Sn
Maximum field [T]	13
Temperature [K]	5
Maximum current density $[\frac{A}{mm^2}]$	15
Nominal current [kA]	45
Turns per module	535
Number of modules	6

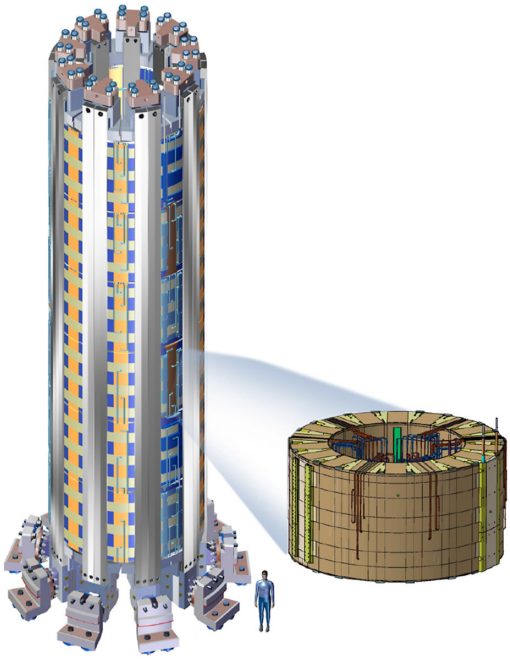

Figure 6.7: ITER central solenoid

So, the reference values for the current density, the temperature and the magnetic field for the RFP machine (tab. 6.2) have been chosen to be within the limits defined by ITER operating conditions.

Table 6.2: Operating limits of the RFP multi-mega Ampere machine

Superconductor material	Nb_3Sn
Maximum field [T]	13
Temperature [K]	5
Maximum current density $[\frac{A}{mm^2}]$	15

6.2.2 Sources

As mentioned before, the sources in this RFP machine are considered able to instantly follow the circuit dynamic by providing the desired voltage at any instant of the discharge. Of course this is an idealization, but as we mentioned, this technological issue will not be considered as a constraint at this stage of the machine analysis.

In this case, if we consider the eq. 6.5, we can see that both the V_M and the V_{LOOP} shall be defined.

$$\begin{bmatrix} L_M & M_{MP} \\ M_{PM} & L_P \end{bmatrix} \begin{bmatrix} \frac{di_M}{dt} \\ \frac{di_P}{dt} \end{bmatrix} = \begin{bmatrix} V_M \\ V_{LOOP} \end{bmatrix} \tag{6.5}$$

For the plasma resistive voltage drop, the same considerations of section 6.1.2 apply to this case. Thus, the V_{LOOP} can be considered constant during the whole discharge, but its value must be scaled considering the geometry of the configuration and the flat-top plasma current. In fig. 6.8, the experimental results obtained from the analysis of RFX-mod discharges are displayed.

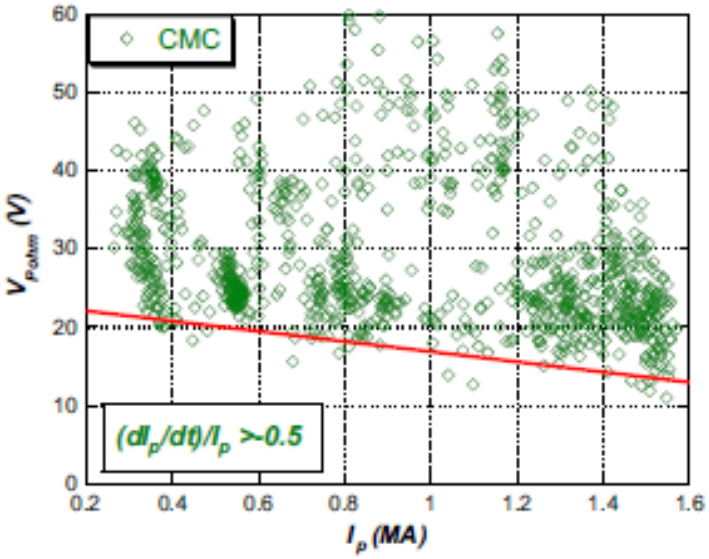

(a) V_{LOOP} scaling with current

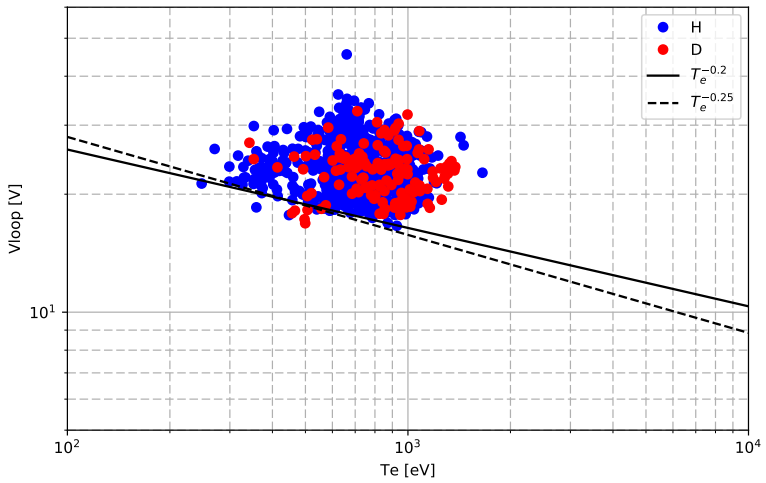

(b) V_{LOOP} scaling with temperature

Figure 6.8: Scaling of the V_{LOOP}

The results pictured in fig. 6.8, led to the following scaling of the resistive voltage drop of the plasma, with respect to the current:

$$V_{LOOP-SCAL} = V_{LOOP} \left(\frac{I_P}{I_{P-SCAL}} \right)^{\alpha} \tag{6.6}$$

This scaling has not been experimentally proven for a wide range of currents, since the maximum plasma current values explored for RFP machines are in fact the ones in RFX-mod. For this reason, two values of the exponent α have been extrapolated from the experimental results, in order to establish an optimistic and a pessimistic scaling:

- α = 0.2 pessimistic case
- α = 0.3 optimistic case

Similarly, we can also define a geometric scaling coefficient. For a toroidal configuration, the V_{LOOP} has been proved to change with a coefficient K_{GEOM}:

$$K_{GEOM} = \left(\frac{R_{0-SCAL}}{R_0}\right)\left(\frac{a}{a_{SCAL}}\right)^{1.5} \tag{6.7}$$

With these coefficients, we can evaluate the V_{LOOP} for a set of different geometries and flat-top currents.

For the voltage V_M applied to the magnetizing winding through power supplies, the following considerations can be made: if the discharge can be subdivided into the Ramp-up, the Flat-top and the Ramp-down, also the analysis of the current transient can be subdivided into three parts, by considering different initial conditions and sources:

1. Ramp-up: Application of a constant reverse V_M, with initial conditions defined in 6.2.1
2. Flat-top: Compensation of the plasma resistive voltage drop, with initial conditions defined when the desired flat-top plasma current is reached during the Ramp-up phase
3. Ramp-down: Depending on the desired duration of the ramp-down, during this phase the OH winding power supply may be removed, or a constant V_M may be applied to reduce the dwell-time. The initial conditions are established when the available magnetic flux reaches the lower limit.

Hence, the DAEs defined in 6.8 can be easily solved by splitting the problem into the aforementioned three parts.

1. Ramp-up

$$\begin{bmatrix} \frac{di_M}{dt}_{R-U} \\ \frac{di_P}{dt}_{R-U} \end{bmatrix} = \begin{bmatrix} M \end{bmatrix}^{-1} \begin{bmatrix} V_{M\,R-U} \\ V_{LOOP} \end{bmatrix} \tag{6.8}$$

With the derivatives we can define the Ramp-up time:

$$t_{R-U} = \frac{i_{P\,F-T}}{\frac{di_P}{dt}_{R-U}} \tag{6.9}$$

And the final i_M:

$$i_{M\,F-T} = i_{M0} + \frac{di_M}{dt}_{R-U} \cdot t_{R-U} \tag{6.10}$$

2. Flat-top

   During the flat-top, since $\frac{di_P}{dt} = 0$, eq. 6.5 can be rewritten as:

$$\begin{cases} V_M = L_M \frac{di_M}{dt} \\ V_{LOOP} = M_{PM} \frac{di_M}{dt} \end{cases} \tag{6.11}$$

   Hence:

$$\frac{di_M}{dt}_{F-T} = \frac{V_{LOOP}}{M_{PM}} \tag{6.12}$$

   If we consider to have a lower limit for the magnetizing current equal to the opposite of the i_{M0}, we can get the flat-top duration:

$$t_{F-T} = \frac{-i_{M0} - i_{M\,F-T}}{\frac{di_M}{dt}_{F-T}} \tag{6.13}$$

3. Ramp-down

$$\begin{bmatrix} \frac{di_M}{dt}_{R-D} \\ \frac{di_P}{dt}_{R-D} \end{bmatrix} = \begin{bmatrix} M \end{bmatrix}^{-1} \begin{bmatrix} V_{M\,R-D} \\ V_{LOOP} \end{bmatrix} \tag{6.14}$$

$$t_{R-D} = \frac{-i_{P\,F-T}}{\frac{di_P}{dt}_{R-D}} \tag{6.15}$$

With these parameters we can thus define the whole discharge evolution.

6.2.3 Plasma inductance

The plasma inductance can be divided into two terms:

- L_i: Plasma internal inductance
- L_e: Plasma external inductance

The internal inductance refers to the one correlated to the total magnetic field inside the plasma area, since the external toroidal magnetic field is extremely weak with respect to the one generated by the plasma itself. The plasma external inductance can be considered as the inductance of a thin wall cylindrical conductor with a superficial distribution of the current.

The Plasma external inductance can thus be calculated with the well known analytical formula:

$$L_e = \mu_0 R_0 \left[\log\left(8\frac{R_0}{a} \right) - 2 \right] \tag{6.16}$$

For the internal inductance, the Plasma current distribution must be defined.

Considering:

$$\mu = \mu_0 \overline{J} \cdot \frac{\overline{B}}{B^2} \tag{6.17}$$

And the pinch parameter:

$$\theta = \frac{B_\theta(a)}{\langle B_\phi \rangle} \tag{6.18}$$

Experimental distributions are well described by μ radial profiles of the form:

$$\mu(r) = \frac{2\theta_0}{a} \left[1 - \left(\frac{r}{a} \right)^\alpha \right] \tag{6.19}$$

The local parameter θ_0 is correlated to the on-axis current value:

$$\theta_0 = \mu_0 a \frac{J(0)}{B(0)} \tag{6.20}$$

Through these equations, the internal current profile can be defined by establishing the θ_0 and α parameters. For the SHAx states, these parameters are in the range:

- $\alpha = 5 \div 5.5$
- $\theta_0 = 1.45 \div 1.52$

Then, from MHD equations, the toroidal and poloidal magnetic field profiles can be obtained. Through these fields, we can calculate the total internal magnetic energy:

$$W_{TOT} = \frac{1}{2}\mu_0 \int_0^a \left(B_\theta^2 + B_\phi^2 \right) r \, dr \tag{6.21}$$

With the total internal magnetic energy, the internal inductance can be evaluated. Once defined the internal inductance for a certain geometry, it can be simply scaled to another one

by considering that:

$$L_{i-SCAL} = L_i \frac{R_{0-SCAL}}{R_0} \tag{6.22}$$

6.2.4 Geometric constraints

To provide an adequate space for a breeding blanket around the plasma region, the central solenoid of the OH winding must be kept at a certain distance, as in the example in fig. 6.9.

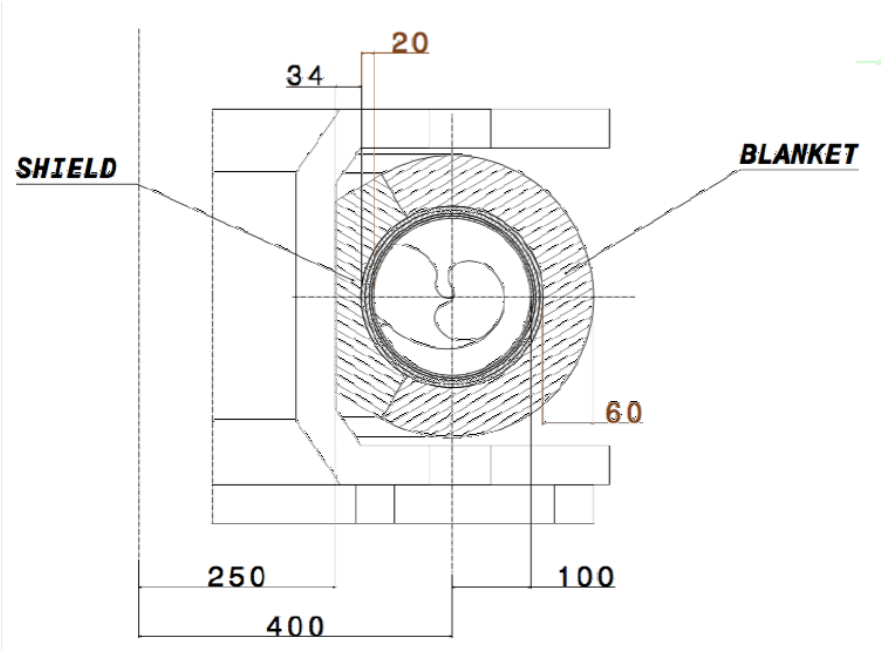

Figure 6.9: Possible configuration of a hybrid RFP reactor

Therefore, in order to satisfy this geometric constraint, the distance between the central solenoid and the external plasma boundary has been maintained at least at $0.5m$ for all the explored configurations.

6.2.5 Limitations for the stray field

The stray field, i.e. the vertical error field inside the plasma area, must be kept below a certain percentage of the equilibrium vertical field that the field shaping coil have to apply. This percentage is in a range of $10 \div 15\%$ of the equilibrium field B_V. Hence, to minimize the percentage of the stray field with respect to the vertical equilibrium field, it is necessary to calculate B_V for each configuration. The vertical equilibrium field can be written as:

$$B_V = \frac{\mu_0 i_{P\,F-T}}{4\pi R_0}\left[\log\left(\frac{8R_0}{a}\right) + \Lambda - 0.5\right] \tag{6.23}$$

Where the a-dimensional parameter Λ is:

$$\Lambda = \frac{l_i}{2} + \beta_\theta - 1 \tag{6.24}$$

β_θ is the ratio between the mean value of the kinetic pressure in the plasma and the poloidal term of the magnetic pressure:

$$\beta_\theta = \frac{\langle p \rangle}{\frac{B_\theta^2}{2\mu_0}} \tag{6.25}$$

and l_i the a-dimensional parameter:

$$l_i = \frac{\int B_\theta^2(r) r d\theta dr}{B_\theta^2(a)\pi a^2} \tag{6.26}$$

For the RFP configuration, the values of β_θ and l_i can be maintained constant for he different geometries:

- $\beta_\theta = 0.1$
- $l_i = 1.5$

But we can see from 6.23 that the equilibrium vertical field depends also on the plasma flat-top current $i_{P\,F-T}$ and on the geometric parameters of the configuration R_0 and a. Hence, the confrontation is made for every single configuration, depending on the geometry and the plasma flat-top current.

6.2.6 Optimization of the geometries

To determine the feasibility of a RFP reactor, a set of different geometries with various major radii R_0 and aspect ratios ξ have been explored. R_0 and a for the different geometries have been established from a scaling of RFX-mod. The range of R_0 varies from a minimum of $4m$ to a maximum of $6m$, whereas the aspect ratio ξ has been kept within the range $4 \div 9$.

Given these limits, the set of geometries that have been considered are:

- $R_0 = 4\,m,\ a = 0.5\,m$

- $R_0 = 4\,m,\ a = 1\,m$
- $R_0 = 6\,m,\ a = 1\,m$
- $R_0 = 6\,m,\ a = 1.5\,m$
- $R_0 = 9\,m,\ a = 1\,m$
- $R_0 = 9\,m,\ a = 1.5\,m$
- $R_0 = 9\,m,\ a = 2.25\,m$

For each case, the geometry and the MMF of each coil have been optimised to meet the geometrical constraints and the magnetic field constraints described in the previous sections. In the next figures, each optimised geometry is represented with the flux map and the peak values of both the stray field and the central solenoid field.

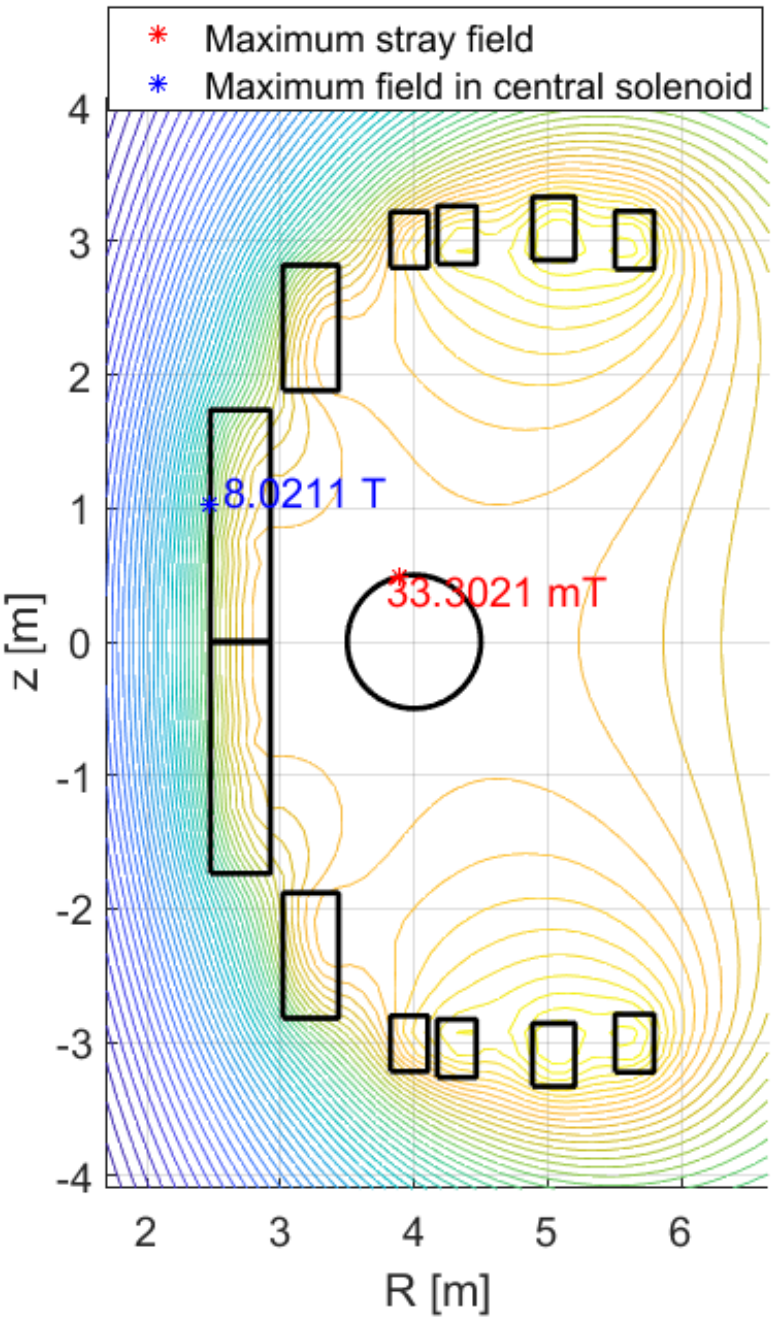

Figure 6.10: $R_0 = 4\,m,\ a = 0.5\,m$

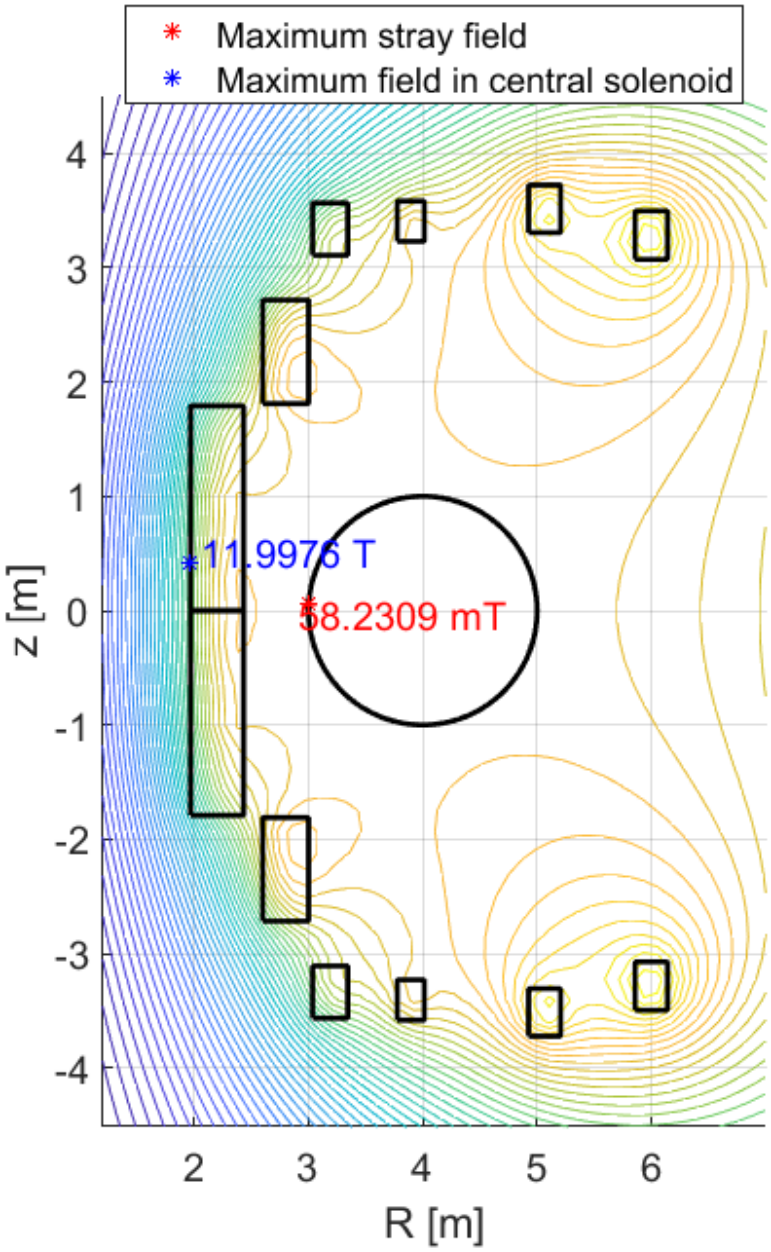

Figure 6.11: $R_0 = 4\ m,\ a = 1\ m$

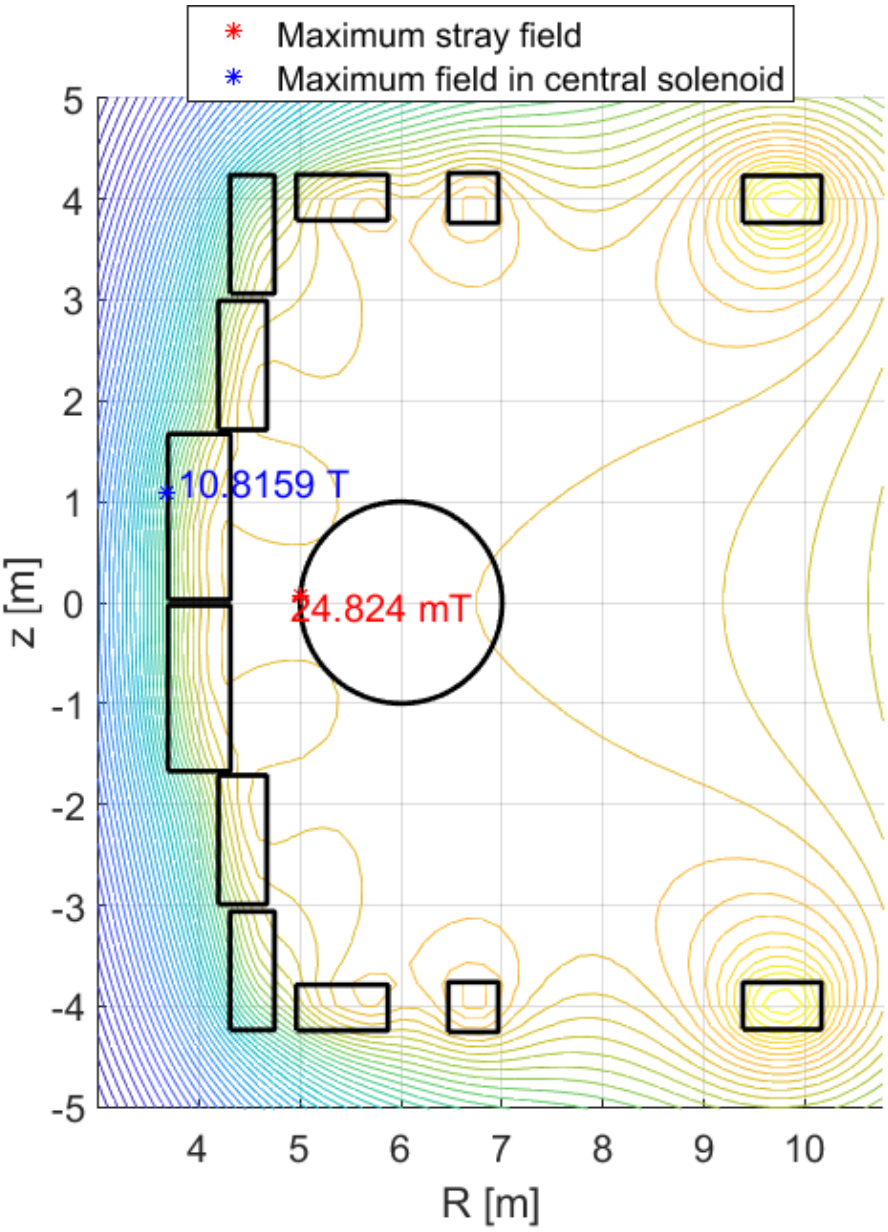

Figure 6.12: $R_0 = 4\,m,\ a = 1\,m$

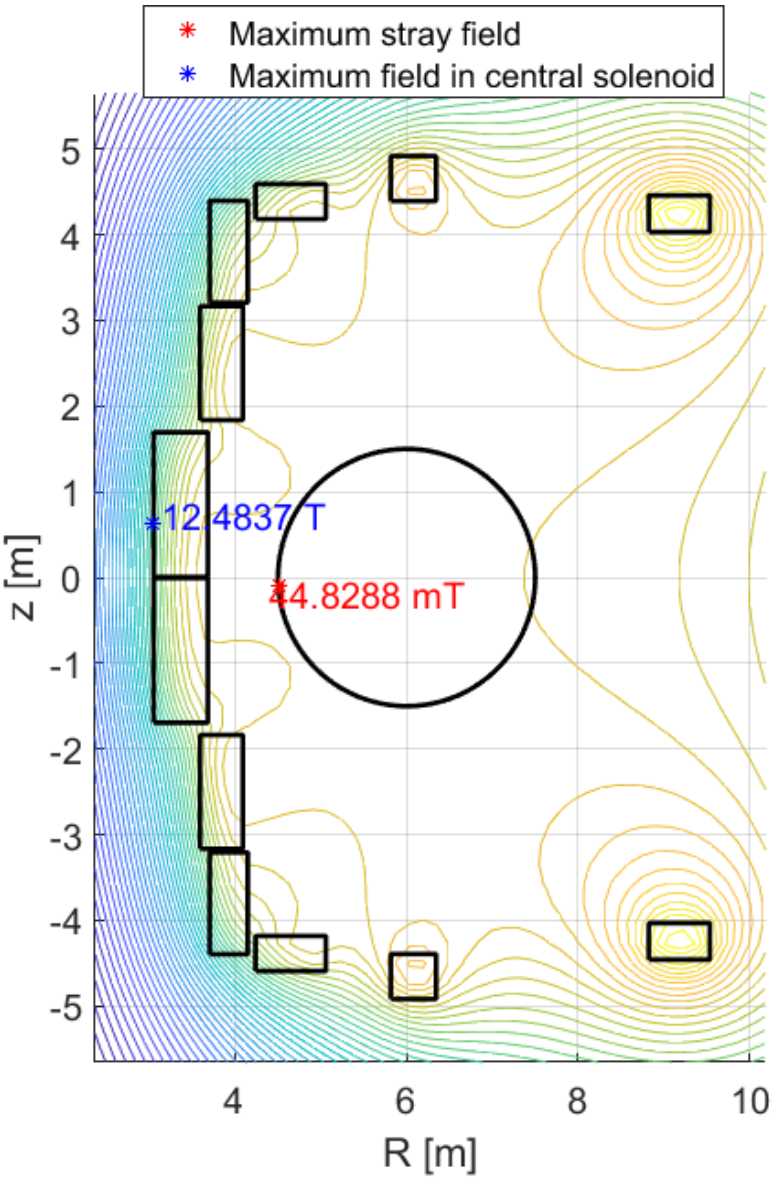

Figure 6.13: $R_0 = 6\ m,\ a = 1.5\ m$

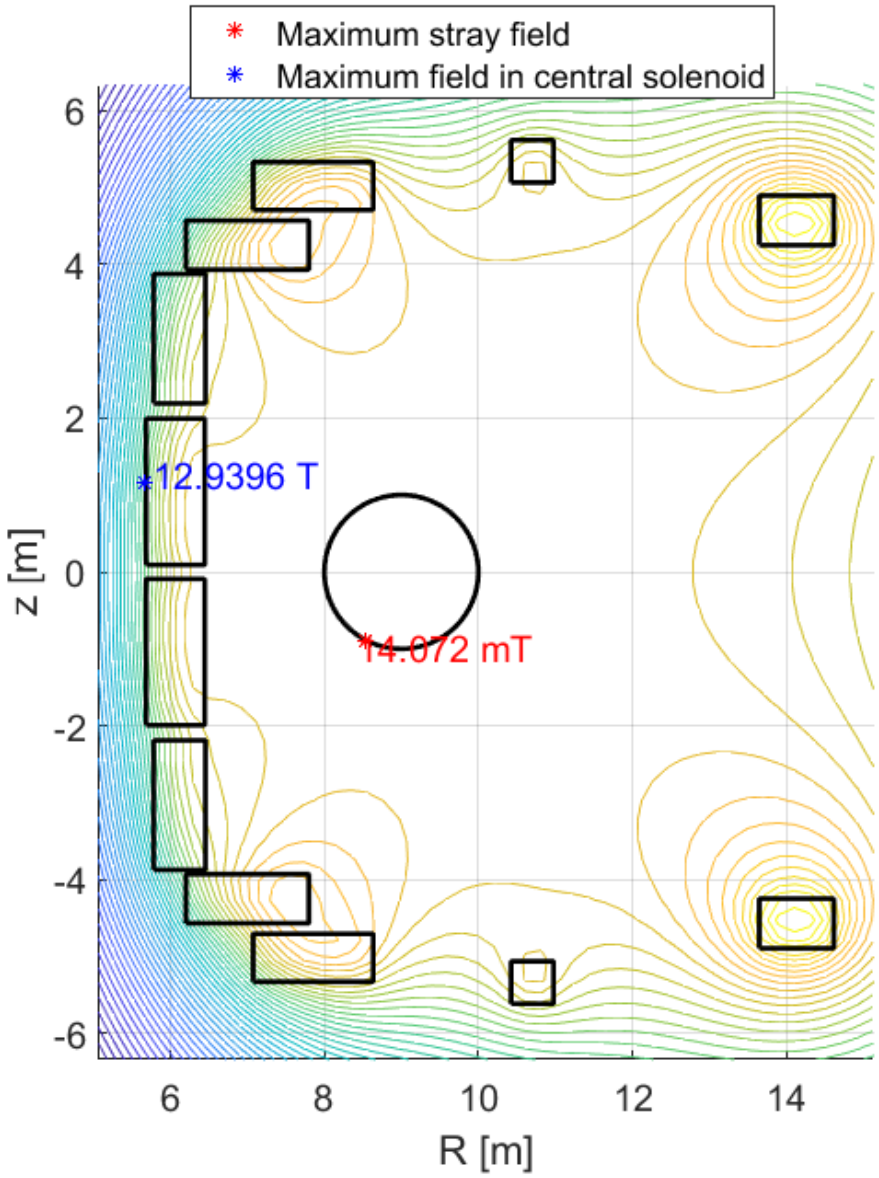

Figure 6.14: $R_0 = 9\,m,\ a = 1\,m$

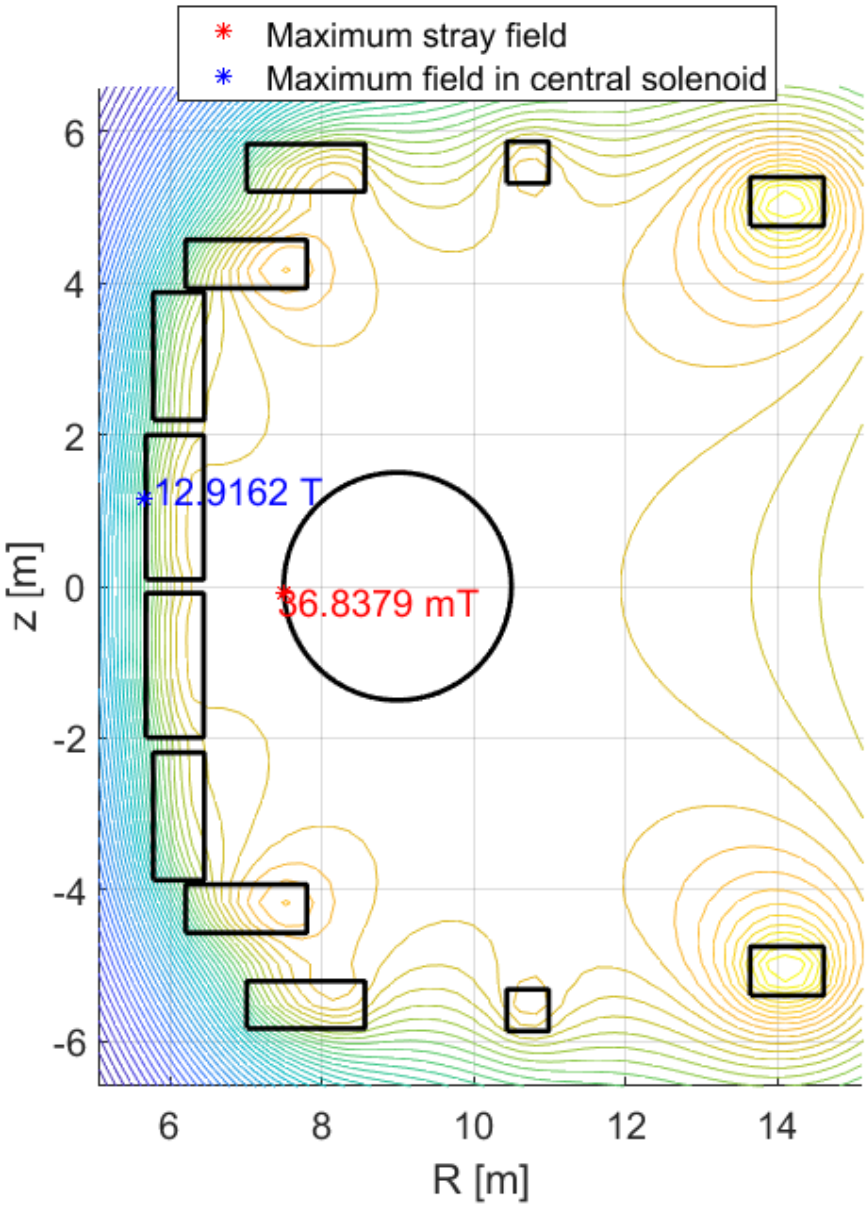

Figure 6.15: $R_0 = 9\ m,\ a = 1.5\ m$

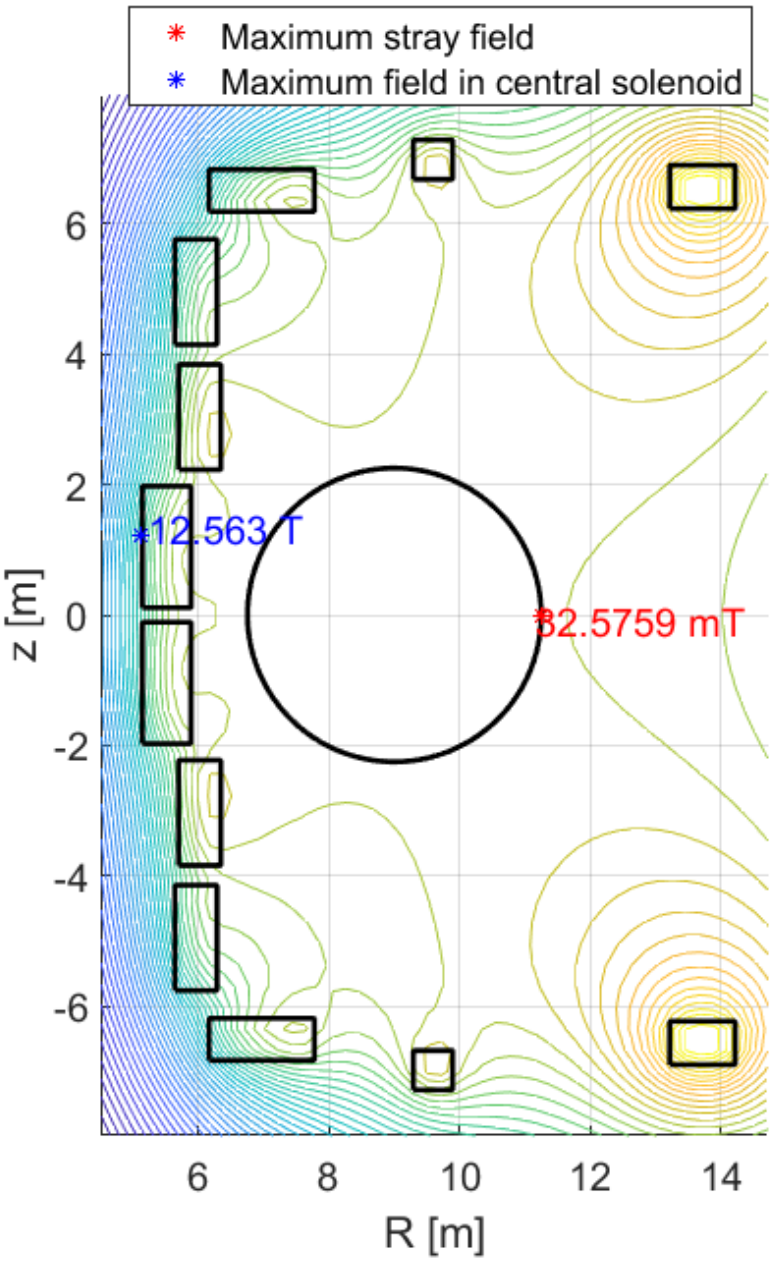

Figure 6.16: $R_0 = 9\ m,\ a = 2.25\ m$

The overall maximum field, an important parameter to define the superconductors operating conditions, didn't reach the established value of approximately $12T$ for each configuration, since a trade-off between the optimal use of the machine and the stray field has to be made. The values are resumed in the following figure:

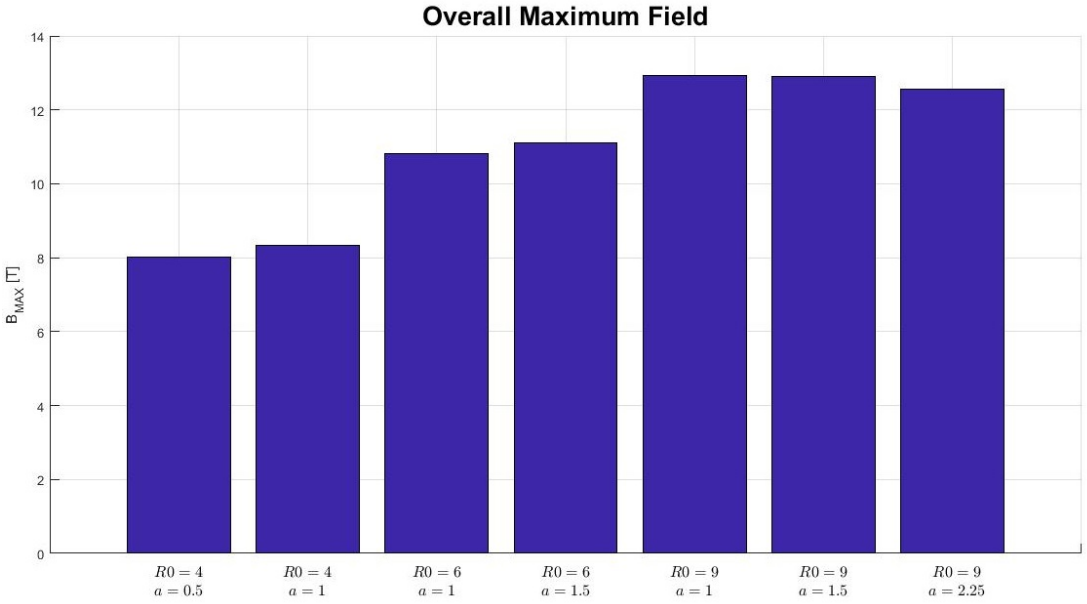

Figure 6.17: Overall maximum values of the magnetic field for each optimised configuration

To obtain information on the feasible configurations, also a set of flat-top currents has been considered for each geometry, to evaluate if the percentage of the stray field, with respect to the equilibrium vertical field, could be kept within the established range. The results for each geometry and for a set of $i_{PF-T} = 5MA - 10MA - 20MA$ are represented in fig. 6.18.

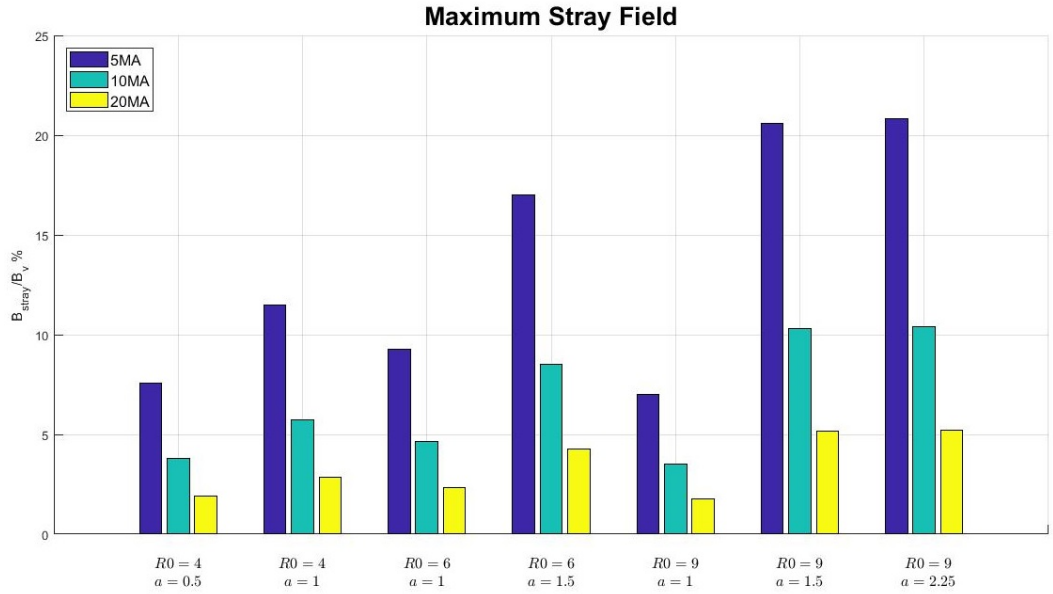

Figure 6.18: Overall maximum values of the magnetic field for each optimised configuration

As it can be seen, the value is not below the limit for certain configurations of geometry and current. This is due to the fact that, by considering a lower flat-top current in the same geometric configuration, the vertical equilibrium field decreases, whereas the stray field is maintained constant. So, of course, if the FS winding is in general able to correct the absolute value of the stray field for a certain geometry, it will be able to correct it for every flat-top current value. The limitation on the percentage value of the stray field with respect to the vertical equilibrium field, is more of a design criterion; in fact, if the FS winding and its power supply are designed for relatively low flat-top plasma currents, they won't be able to correct a strong stray field if it becomes relevant if compared with the vertical equilibrium field they need to provide. So, the graph in fig. 6.18, shows us the flat-top current reference for which it would be reasonable to design a machine with a given geometry. For example, machines with $R_0 = 6\,m,\ a = 1.5\,m$ and with $R_0 = 9\,m,\ a = 2.25\,m$ would not be designed with good criteria, if the maximum operating flat-top current is $5MA$.

6.2.7 Discharge simulations for the optimised geometries

With the optimised geometries, we were finally able to perform the discharge simulations in a wide range of V_{LOOP}, to evaluate which machines are the most viable choices for the development of RFP reactors. Basing on the pessimistic and optimistic scaling of the V_{LOOP},

the following values have been chosen to investigate the different configurations:

- $V_{LOOP} = 1V$
- $V_{LOOP} = 5V$
- $V_{LOOP} = 10V$

With the following results:

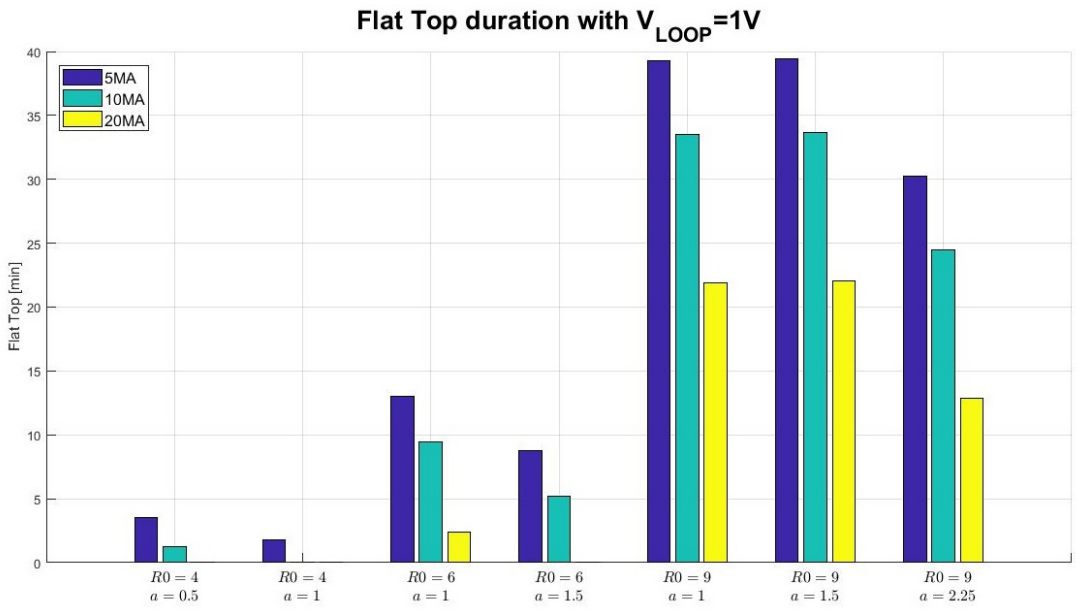

Figure 6.19: Flat-top duration for the optimised configurations with $V_{LOOP} = 1V$

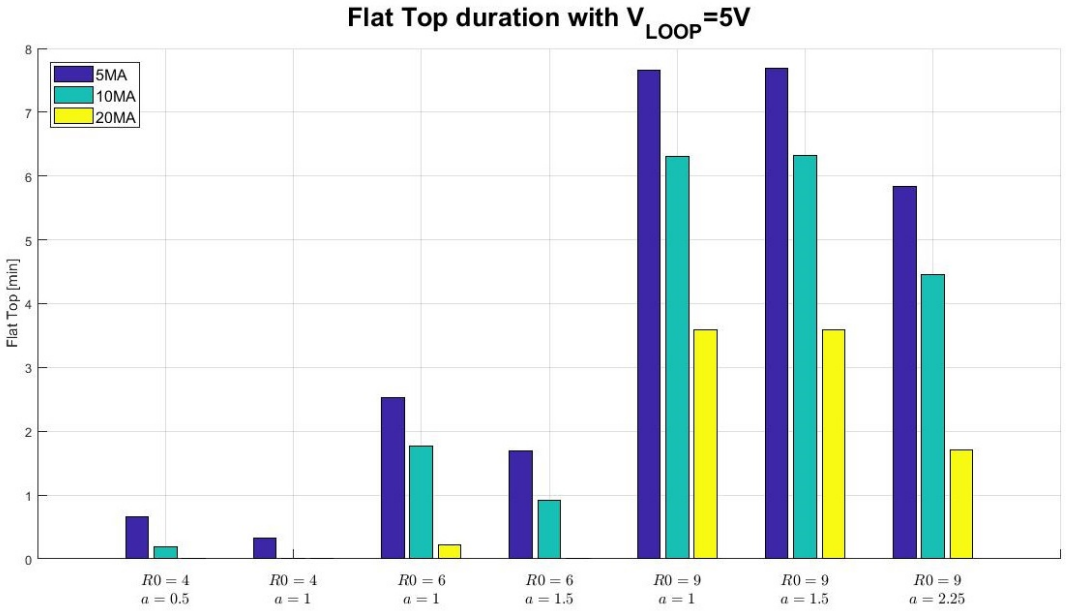

Figure 6.20: Flat-top duration for the optimised configurations with $V_{LOOP} = 5V$

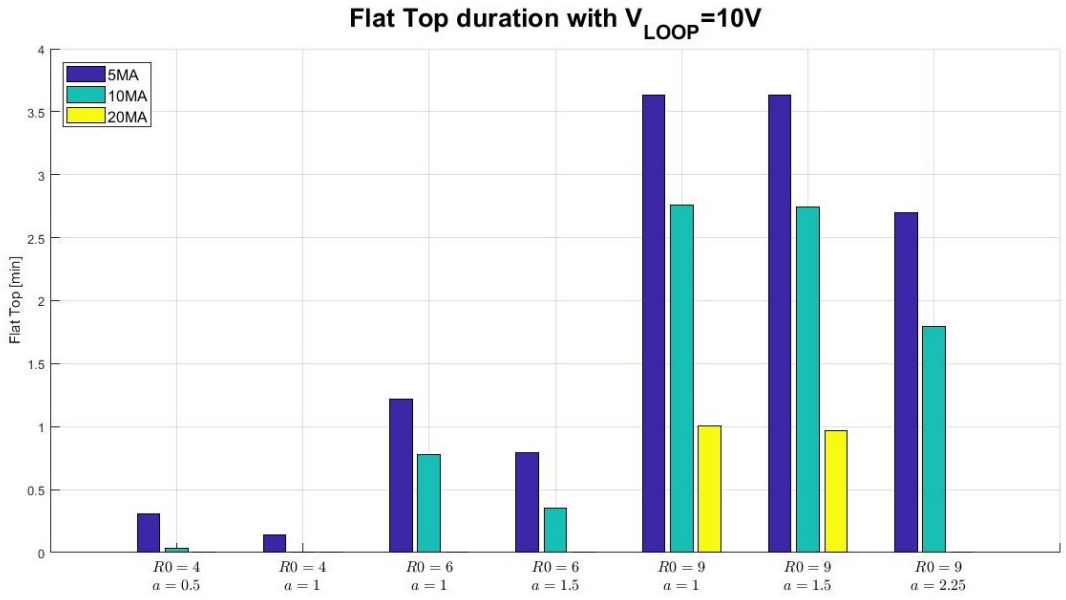

Figure 6.21: Flat-top duration for the optimised configurations with $V_{LOOP} = 10V$

The best results are obviously achieved with the bigger machines, with major radius $R_0 = 9\ m$. However,with the RFX-mod research team and director, it was concluded that the

bigger machines would be too expensive and technologically challenging in a short-to-mid range period of time. Then, since RFX-mod is a well studied machine and the considerations made for the aspect ratio $\xi = 4$ are experimentally supported, it has been decided to maintain this value of ξ also for the scaled machines. Therefore, the final choice was:

- $R_0 = 4\,m,\ a = 1\,m$
- $R_0 = 6\,m,\ a = 1.5\,m$

6.2.8 Follow-up on the chosen configurations

In this analysis, only the configurations $R_0 = 4\,m,\ a = 1\,m$ and $R_0 = 6\,m,\ a = 1.5\,m$ are considered, since they have been determined to be the most viable ones.

Given the scaling formulas defined in 6.6 and 6.7, more likely and targeted values of the V_{LOOP} can be defined, according to the following considerations:

Given the best case scenario for RFX-mod, with

- $V_{LOOP} = 15\,V$
- $i_{P\,F-T} = 1.5\,MA$

We can consider to scale the machine, in terms of flat-top plasma current, of a factor 10. Consequently, we can define:

$$V^*_{LOOP} = V_{LOOP} K_{SCAL} = V_{LOOP} \left(\frac{i_{P\,F-T}}{i^*_{P\,F-T}} \right)^{\alpha} = 15 \left(\frac{1}{10} \right)^{\alpha} \tag{6.27}$$

Considering the pessimistic and the optimistic scaling:

- α = 0.2 pessimistic case
- α = 0.3 optimistic case

We obtain two values for the current scaling coefficient:

- K_{CURR-P} = 0.631 pessimistic case
- K_{CURR-O} = 0.5012 optimistic case

Taking into account also the geometry scaling coefficient defined in 6.7

$$K_{GEOM} = \left(\frac{R_{0-SCAL}}{R_0}\right)\left(\frac{a}{a_{SCAL}}\right)^{1.5} \tag{6.28}$$

The final values of the V_{LOOP} can be determined for the two configurations as:

$$V_{LOOP-SCAL} = K_{CURR}K_{GEOM} \tag{6.29}$$

Obtaining:

Table 6.3: Scaling of the V_{LOOP} for the optimised geometries

Geometry	$V_{LOOP-SCAL}\ optimistic$	$V_{LOOP-SCAL}\ pessimistic$
$R_0 = 4m, a = 1m$	$5.3V$	$6.7V$
$R_0 = 6m, a = 1.5m$	$4.3V$	$5.5V$

Since some studies on the V_{LOOP} experimental trend led to a result of $\alpha = 0.5$, we considered also a third scenario, the "very-optimistic" case. The value $\alpha = 0.5$ has however been considered to be an excessive positive forecast, so an intermediate value of $\alpha = 0.4$ was considered for the very-optimistic scenario. Besides, this scaling presents major uncertainties, so it would be an unnecessary introduction of details to consider the precise values we calculated. Hence, we centred in the following values, with a tolerance of $\pm 1\ V$:

Table 6.4: V_{LOOP} values assumed for the conceptual design

Geometry	$V_{LOOP-SCAL}$
$R_0 = 4m, a = 1m$	$5 \pm 1\ V$
$R_0 = 6m, a = 1.5m$	$4 \pm 1\ V$

With these values, we were finally able to perform more simulations, gathering more plausible and detailed results for the chosen geometries.

For each configuration, three different values for the flat-top plasma current were considered:

- $10MA$
- $15MA$

- $20MA$

6.2.9 Analysis of the configuration $R_0 = 4m, a = 1m$

To meet the required operating conditions for the overall maximum field and the stray field, the total MMF has been further modified. Also, we tried to achieve an electric field of about $10\frac{V}{m}$ in the plasma region, an optimal value for the initiation of the discharge. This led to the following results, resumed in fig. 6.22 and tab. 6.5.

Abbreviations

- R_0 : major radius
- a : minor radius
- Φ : magnetic flux referred to the plasma cross section
- MMF_{OH} : ohmic heating winding total ampere-turns
- B_{MAX} : overall maximum magnetic field
- B_{STRAY} : maximum stray field in the plasma region
- V_{LOOP} : plasma electric potential
- I_P : flat-top plasma current
- t_{F-T} : flat-top duration
- E_{PLASMA} : electric field applied to the plasma

Table 6.5: OH winding parameters for $R_0 = 4m, a = 1m$

$MMF_{OH}\ [MAt]$	$\Phi(peak\ to\ peak)\ [Wb]$	$B_{MAX}\ [T]$	$B_{STRAY}\ [mT]$
71.5	350	12	58

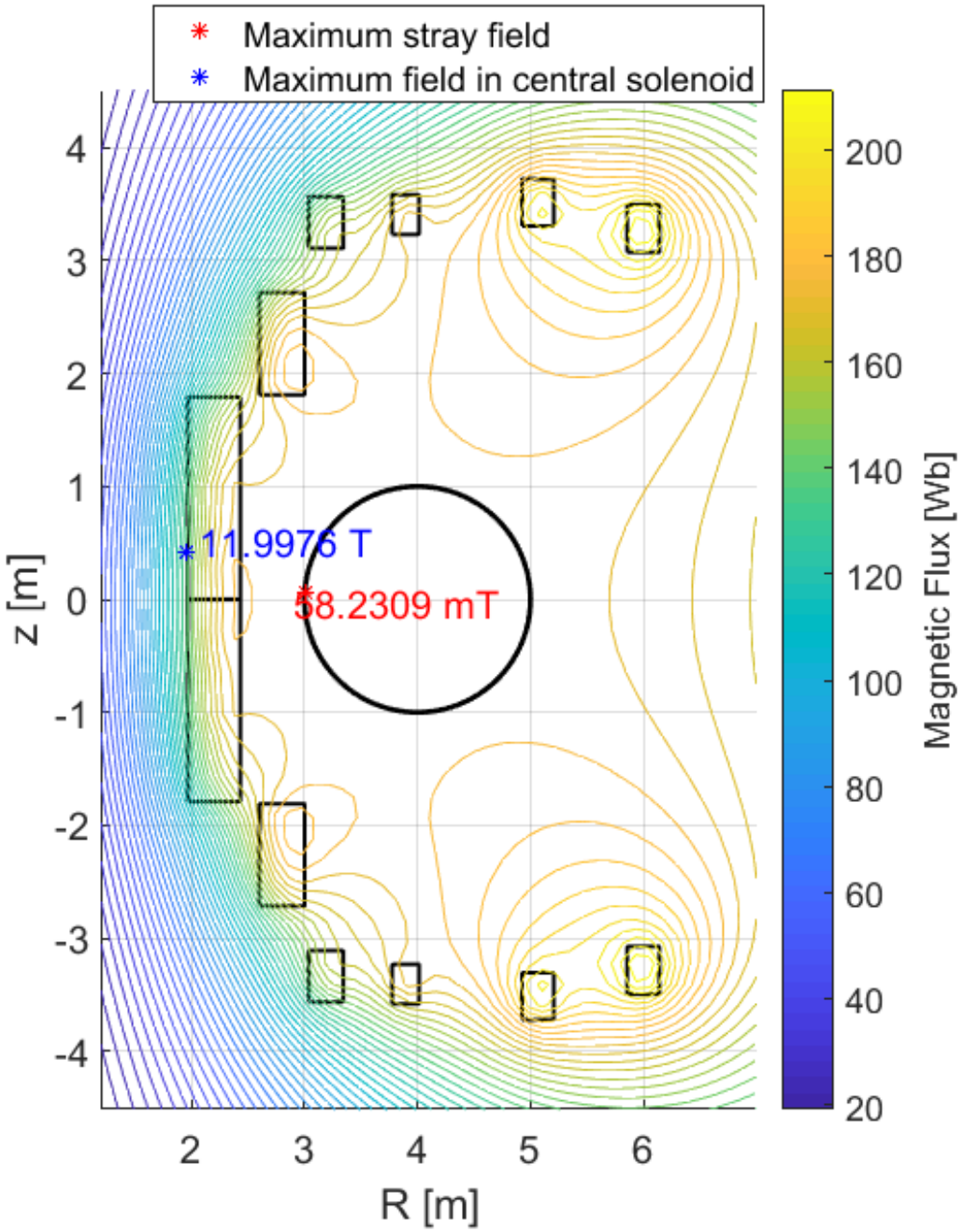

Figure 6.22: Flux map and maximum values of the constrained parameters for $R_0 = 4m, a = 1m$

As aforementioned, discharge simulations with three different values of the flat-top plasma current were performed, with the results resumed in tab. 6.6 and thoroughly analysed in the following sections.

Table 6.6: Plasma parameters for $R_0 = 4m, a = 1m$

$V_{LOOP}\,[V]$	$I_P\,[MA]$	$t_{F-T}\,[s]$	$E_{PLASMA}\,[\frac{V}{m}]$
6	10	32.9	10.2
5	10	39.6	10.2
4	10	49.8	10.2
6	15	20.2	10.2
5	15	24.5	10.2
4	15	30.9	10.2
6	20	7.4	10.2
5	20	9.3	10.2
4	20	12.1	10.2

Trends of the constrained magnetic field

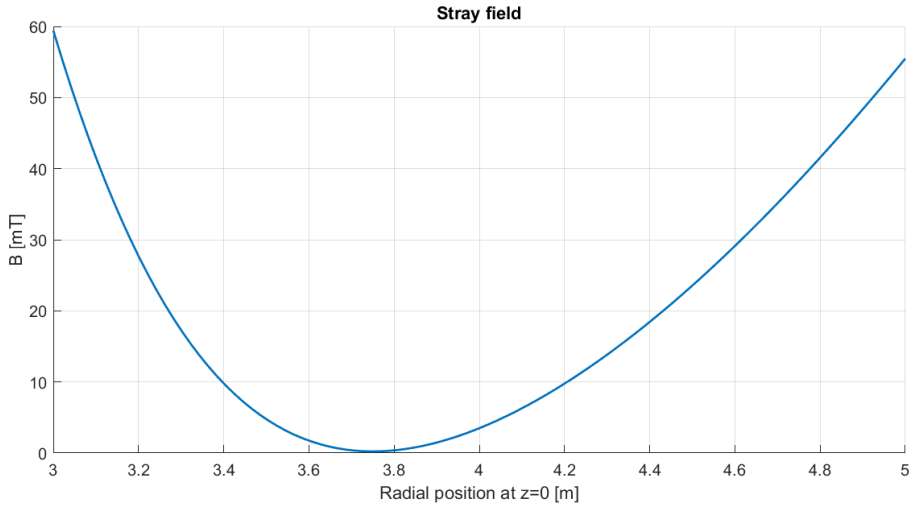

Figure 6.23: Trend of the stray field along a radial path, for $R_0 = 4m, a = 1m$

The stray field is always maintained below the 10% of B_V, inside the plasma area, but the fig. 6.23 also shows that it decreases towards the centre of the configuration; hence, since the greater interactions between the plasma and the stray field happen in the centre of the configuration, the error force that needs to be compensated is much more limited than the value which corresponds to the maximum stray field.

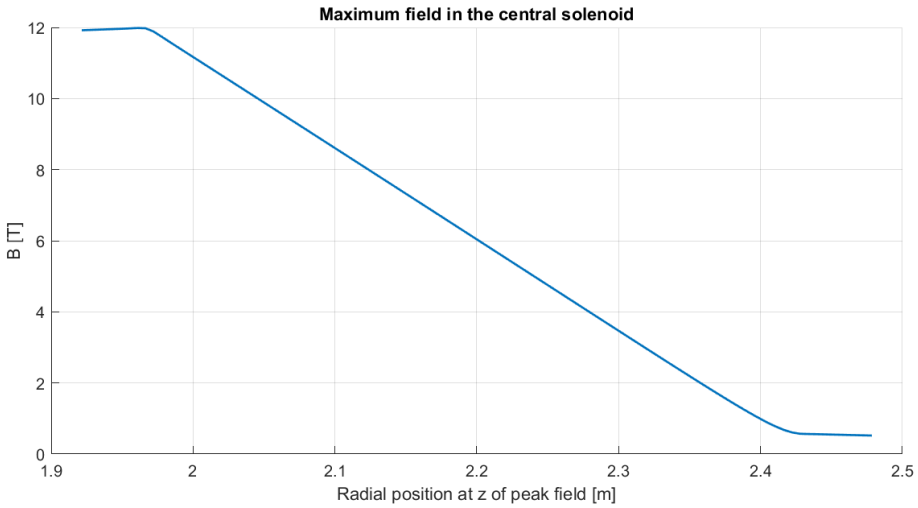

Figure 6.24: Trend of the overall maximum field along a radial path in the central solenoid, for $R_0 = 4m, a = 1m$

Case: $I_P = 10MA$

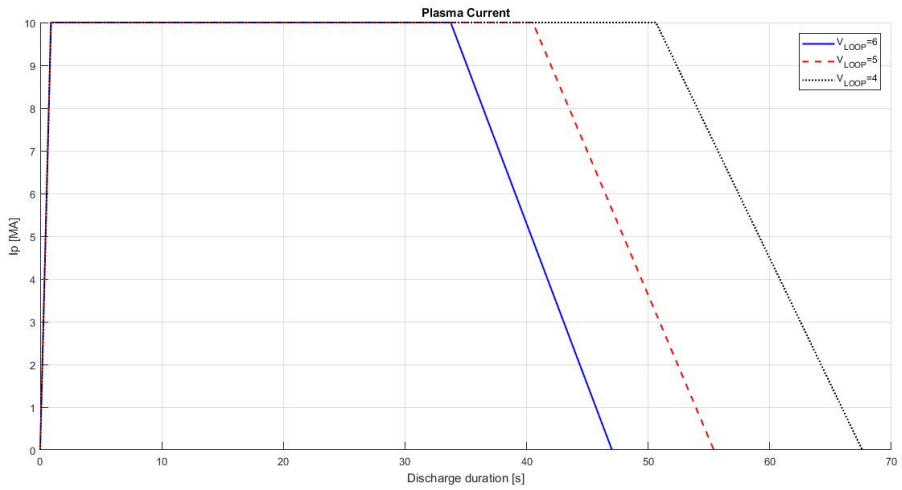

Figure 6.25: Plasma currents for $R_0 = 4m, a = 1m$

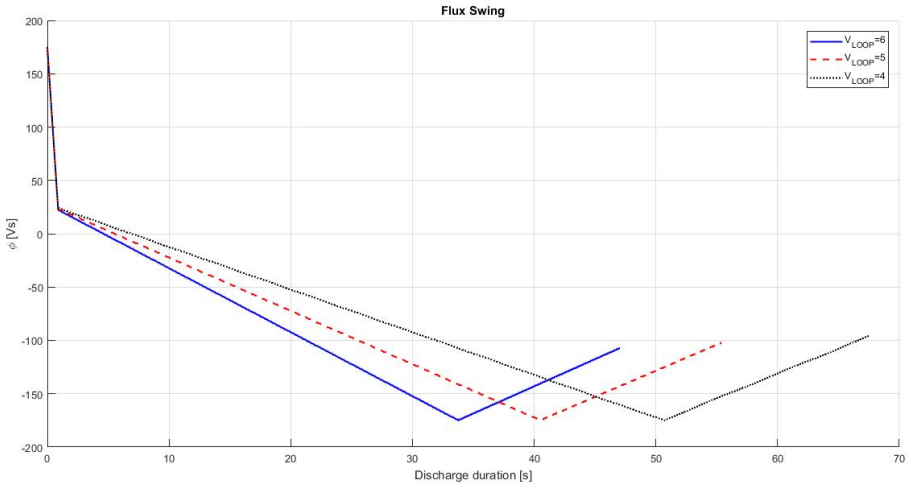

Figure 6.26: Flux swing for $R_0 = 4m, a = 1m$

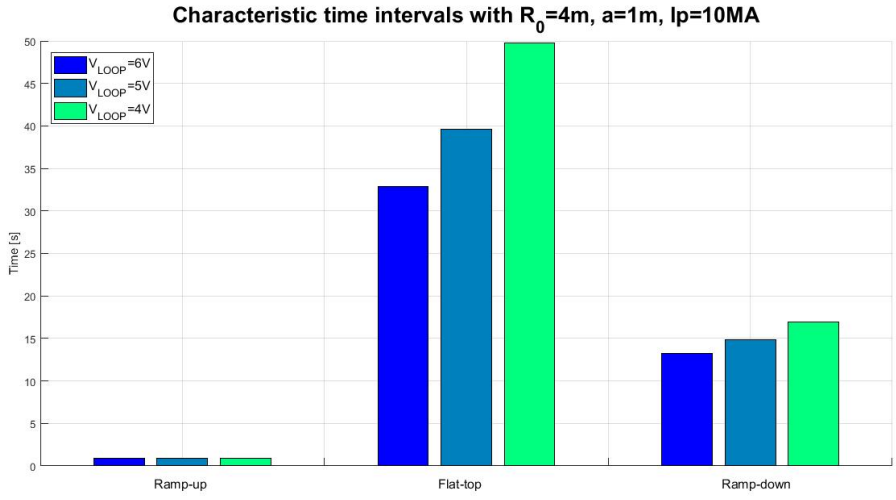

Figure 6.27: Characteristic time intervals for $R_0 = 4m, a = 1m$

CASE: $I_P = 15MA$

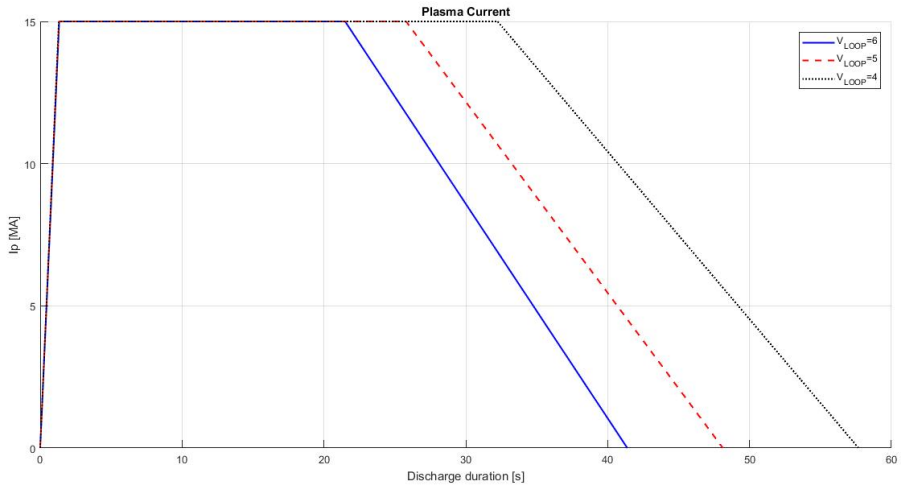

Figure 6.28: Plasma currents for $R_0 = 4m, a = 1m$

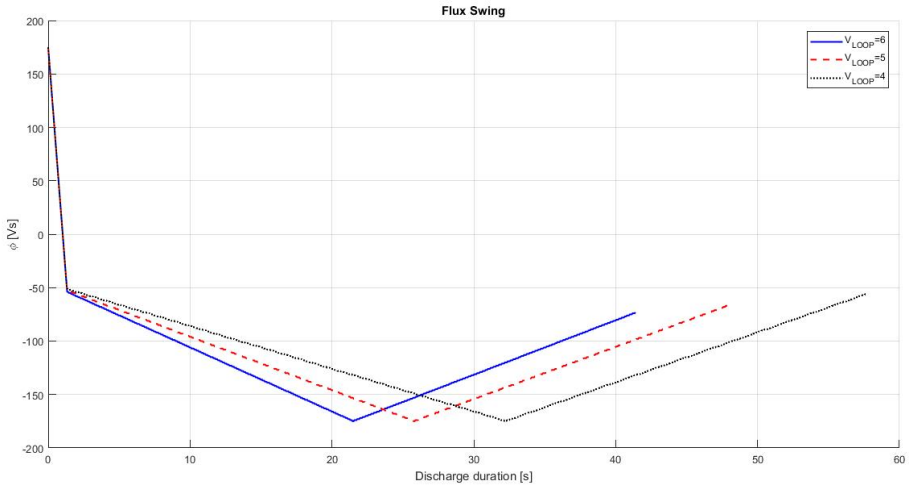

Figure 6.29: Flux swing for $R_0 = 4m, a = 1m$

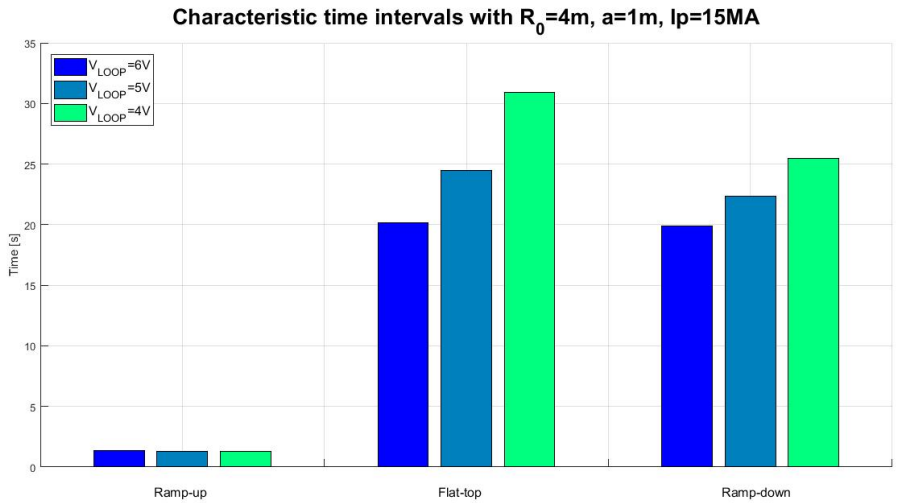

Figure 6.30: Characteristic time intervals for $R_0 = 4m, a = 1m$

CASE: $I_P = 20MA$

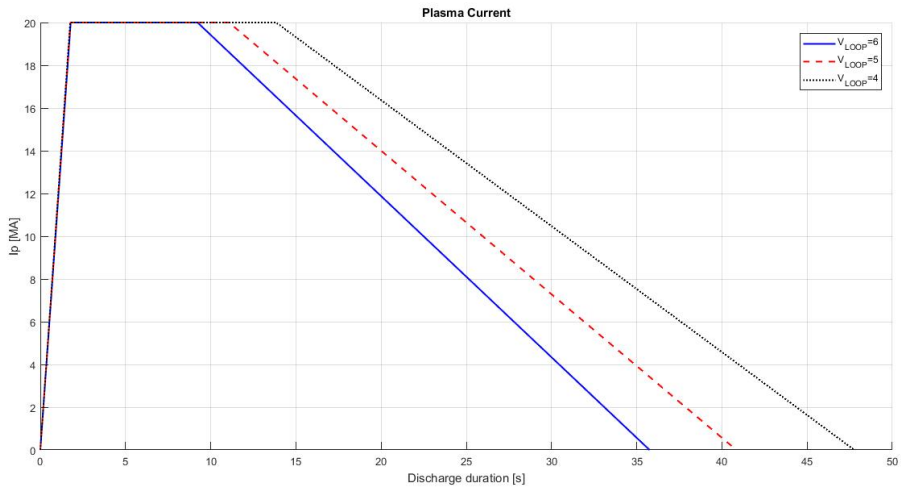

Figure 6.31: Plasma currents for $R_0 = 4m, a = 1m$

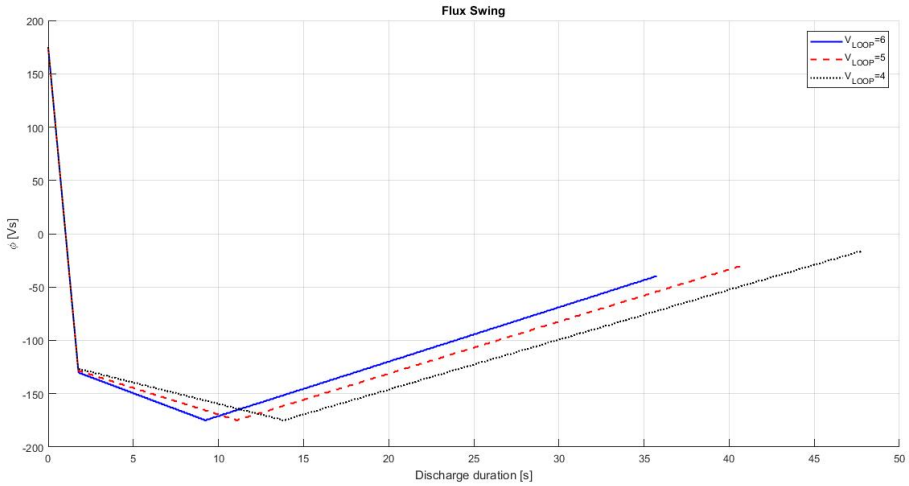

Figure 6.32: Flux swing for $R_0 = 4m, a = 1m$

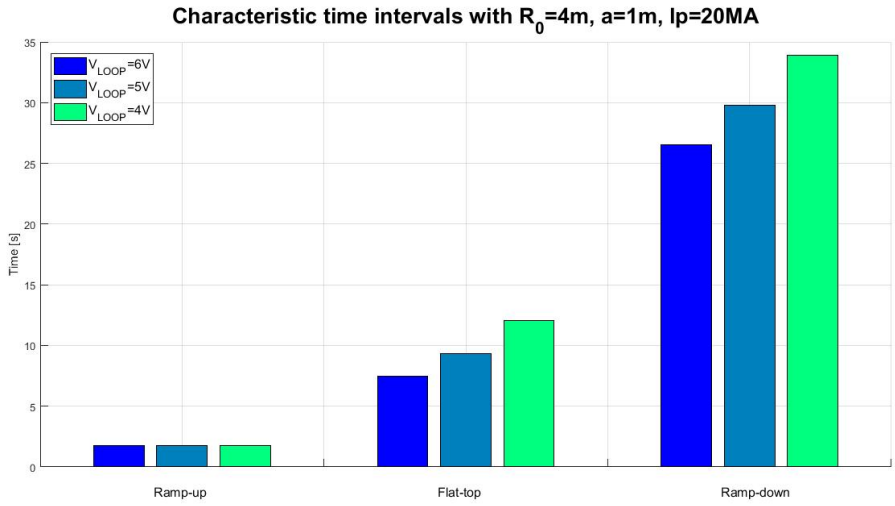

Figure 6.33: Characteristic time intervals for $R_0 = 4m, a = 1m$

For all the described cases, the magnetizing winding has been kept un-powered during the ramp-down.

6.2.10 Analysis of the configuration $R_0 = 6m, a = 1.5m$

The same was done for the case $R_0 = 6m, a = 1.5m$, with these results:

Table 6.7: OH winding parameters for $R_0 = 6m, a = 1.5m$

$MMF\ [MAt]$	$\Phi(peak\ to\ peak)\ [Wb]$	$B_{MAX}\ [T]$	$B_{STRAY}\ [mT]$
107.2	832	12.5	44.8

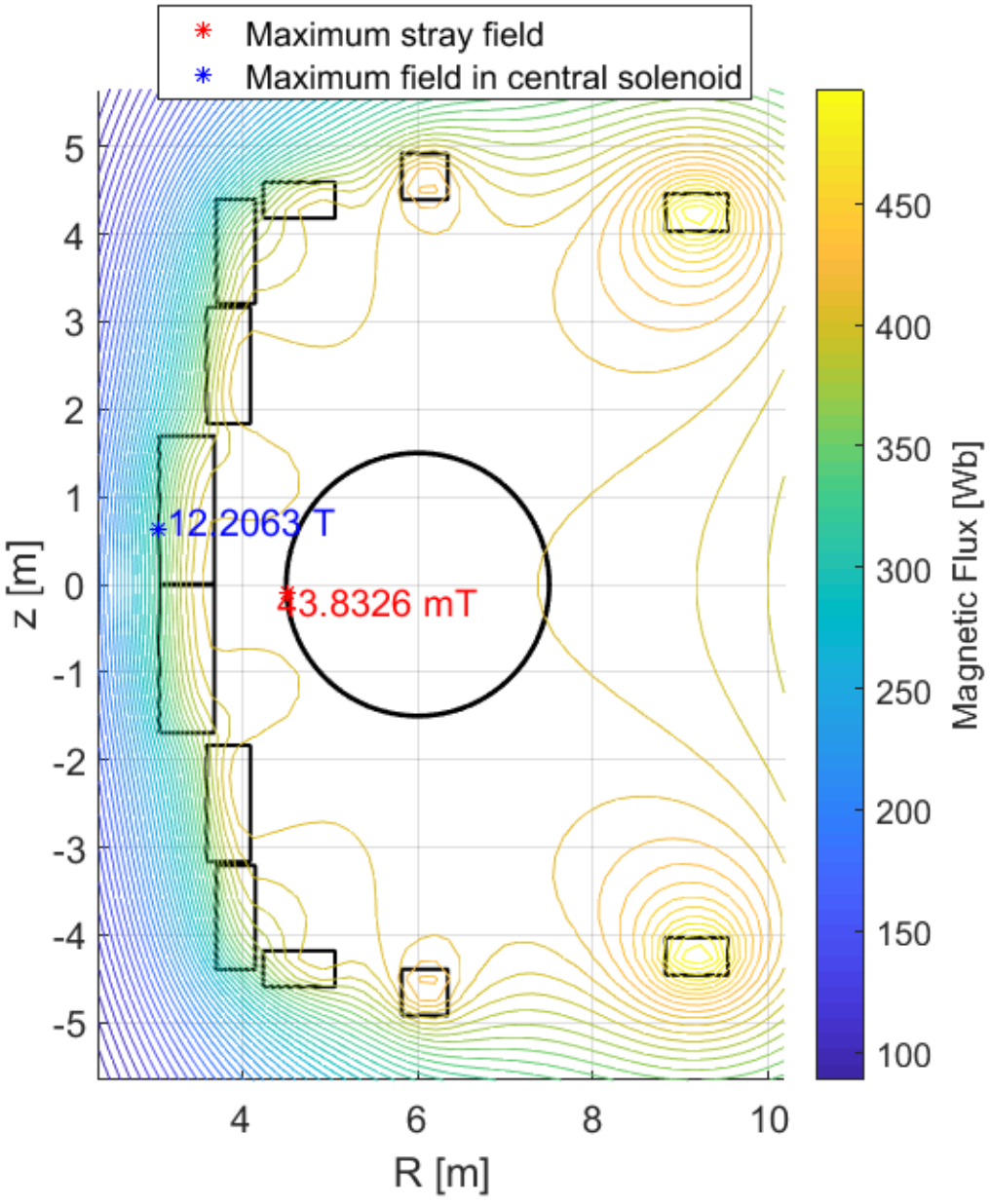

Figure 6.34: Flux map and maximum values of the constrained parameters for $R_0 = 6m, a = 1.5m$

Table 6.8: Plasma parameters for $R_0 = 6m, a = 1.5m$

$V_{LOOP}\,[V]$	$I_P\,[MA]$	$t_{F-T}\,[s]$	$E_{PLASMA}\,[\frac{V}{m}]$
5	10	117.5	10.6
4	10	147.1	10.6
3	10	196.5	10.6
5	15	95	10.6
4	15	119.1	10.6
3	15	159.2	10.6
5	20	72.5	10.6
4	20	91.1	10.6
3	20	122	10.6

Trends of the constrained magnetic field

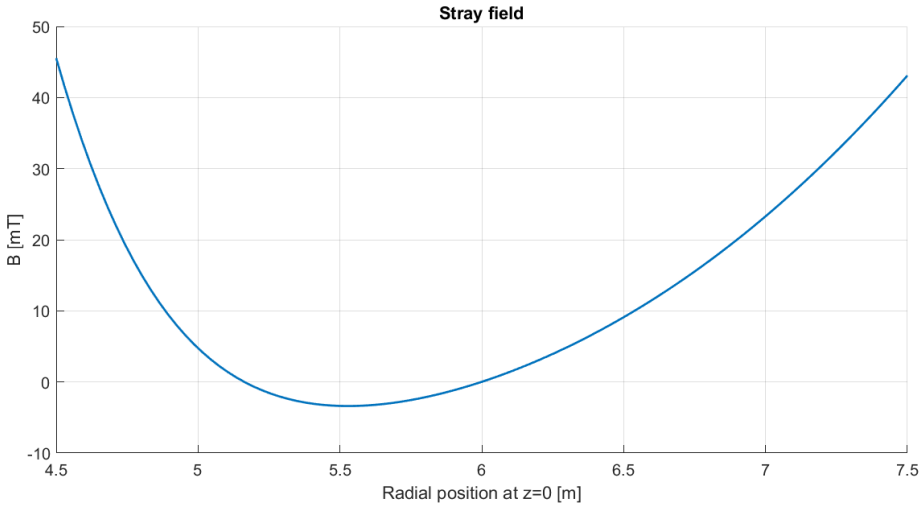

Figure 6.35: Trend of the stray field along a radial path, for $R_0 = 6m, a = 1.5m$

The same considerations made for the other geometry can be applied here.

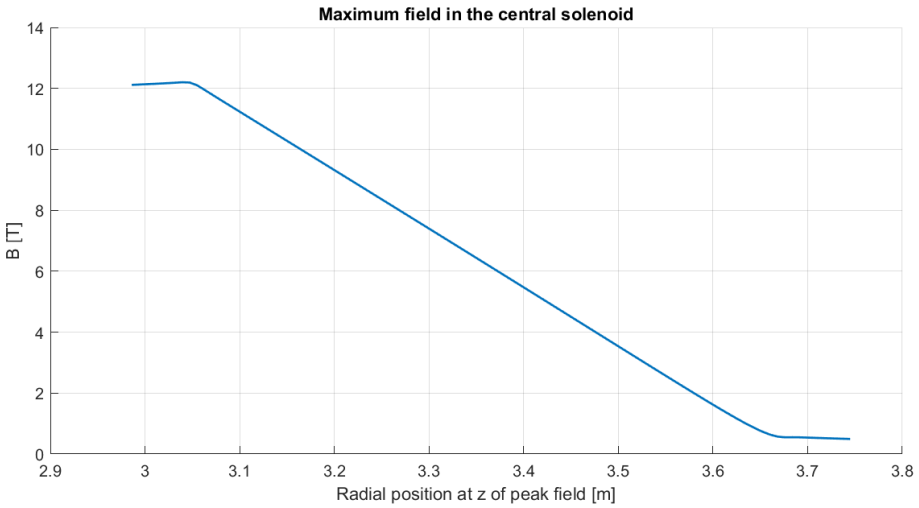

Figure 6.36: Trend of the overall maximum field along a radial path in the central solenoid, for $R_0 = 6m, a = 1.5m$

Case: $I_P = 10MA$

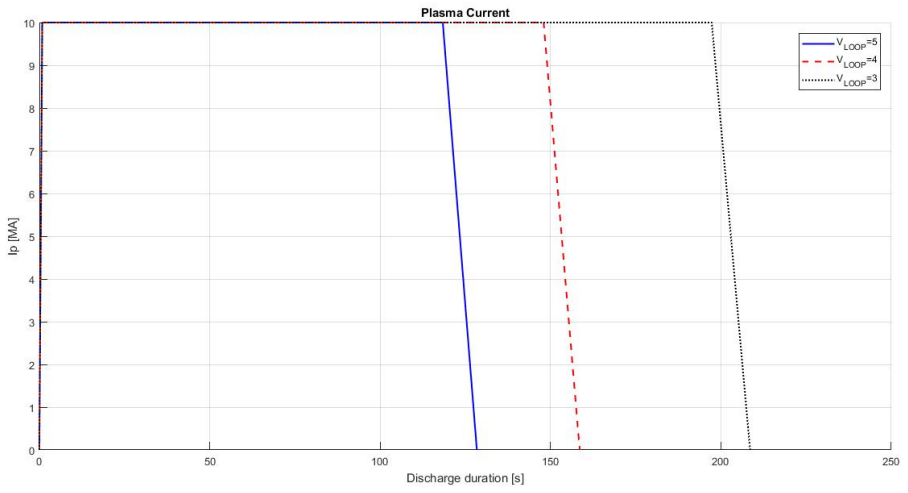

Figure 6.37: Plasma currents for $R_0 = 6m, a = 1.5m$

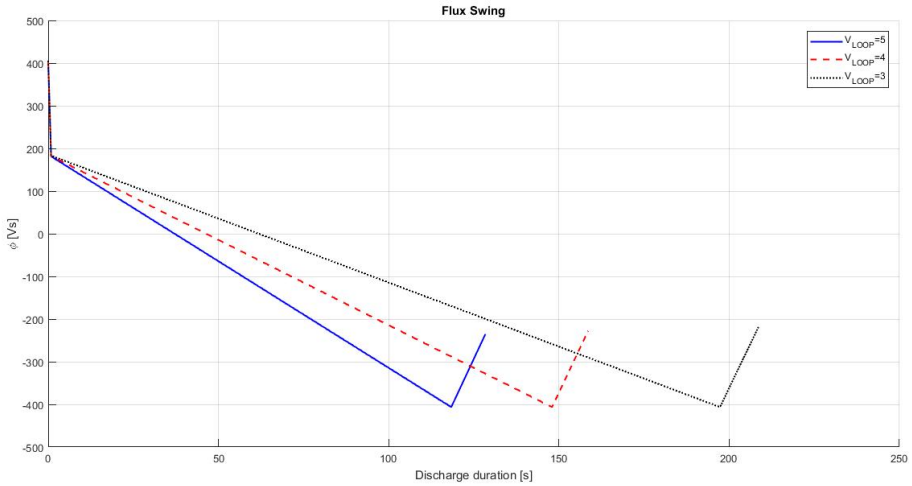

Figure 6.38: Flux swing for $R_0 = 6m, a = 1.5m$

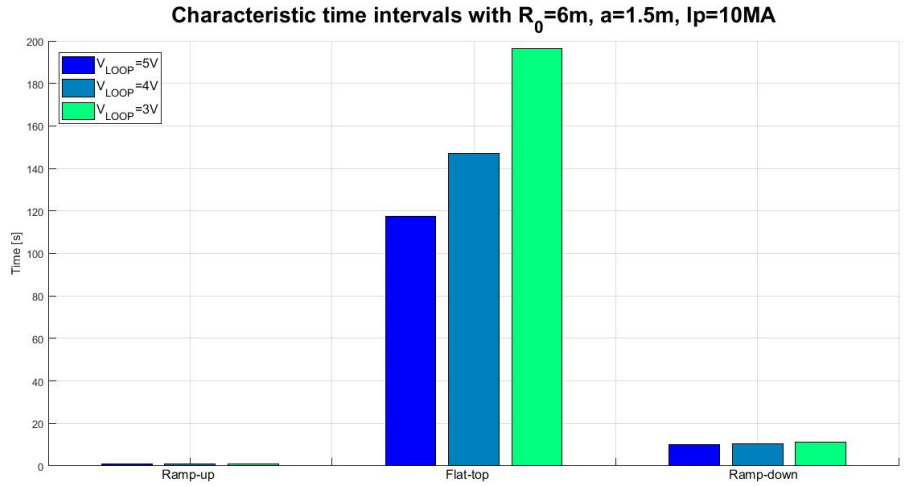

Figure 6.39: Characteristic time intervals for $R_0 = 6m, a = 1.5m$

CASE: $I_P = 15MA$

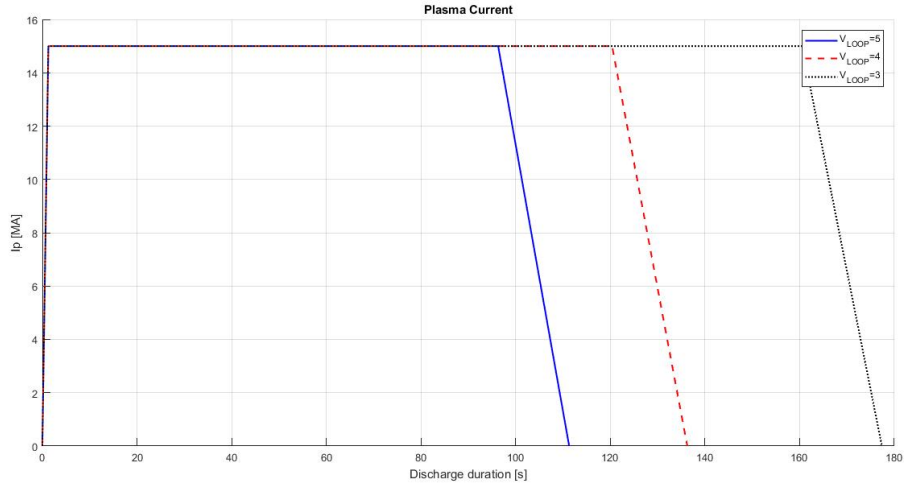

Figure 6.40: Plasma currents for $R_0 = 6m, a = 1.5m$

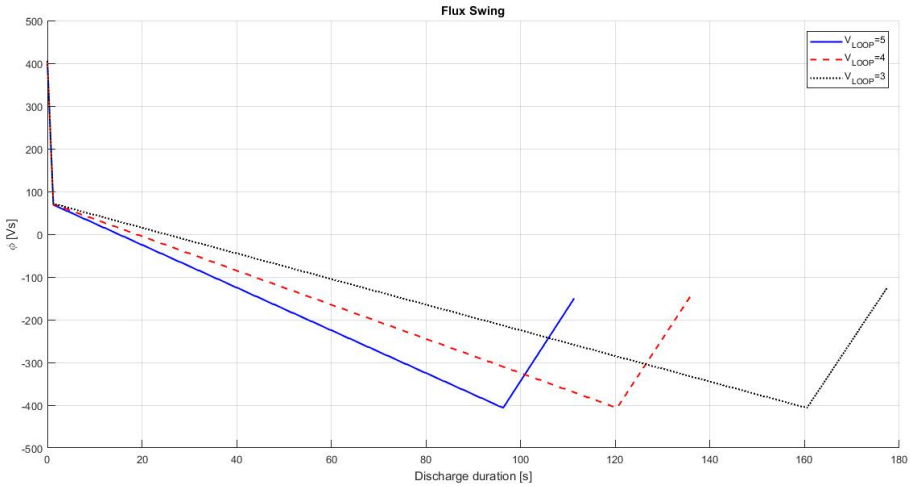

Figure 6.41: Flux swing for $R_0 = 6m, a = 1.5m$

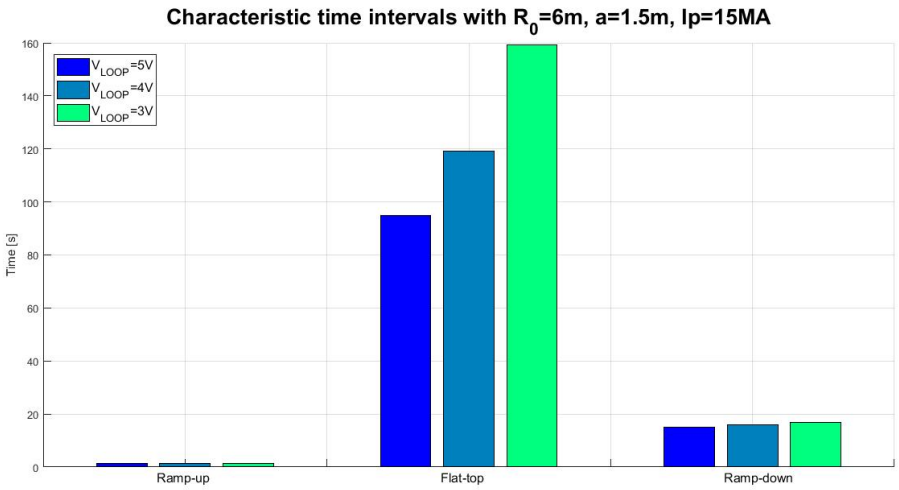

Figure 6.42: Characteristic time intervals for $R_0 = 6m, a = 1.5m$

CASE: $I_P = 20MA$

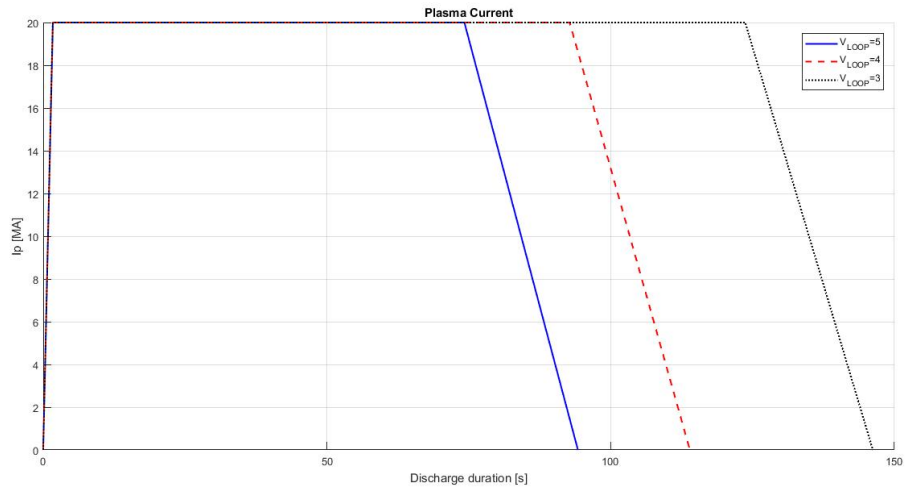

Figure 6.43: Plasma currents for $R_0 = 6m, a = 1.5m$

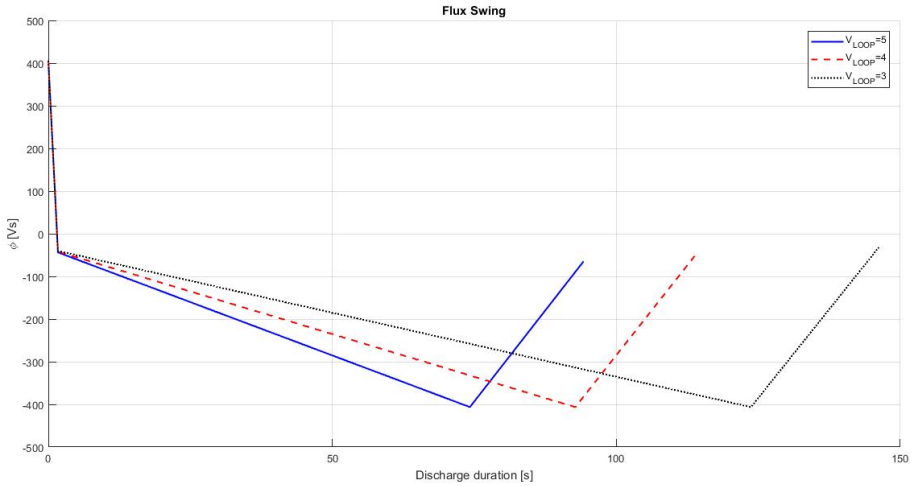

Figure 6.44: Flux swing for $R_0 = 6m, a = 1.5m$

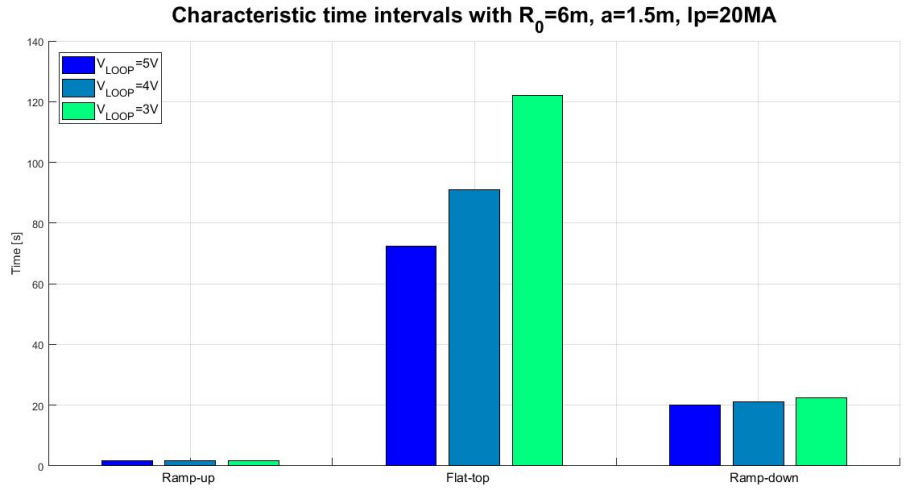

Figure 6.45: Characteristic time intervals for $R_0 = 6m, a = 1.5m$

For all the described cases, the magnetizing winding has been kept un-powered during the ramp-down.

7

Conclusion

This early-stage design of a RFP multi-mega Ampere machine has led to the choice of two potential solutions, which define a baseline for the development of RFP reactors.

As seen, the selection criteria has been:

- Compactness of the machine
- Limitation of the stray field in the plasma region within a value of $10\% B_V$
- Limitation of the maximum field inside the OH winding at a value of $12 \div 13 T$
- Achievement of an electric field of $10 \frac{V}{m}$ during the ramp-up flux swing
- Sustained duration of the flat-top phase

The chosen geometries are:

- $R_0 = 4\, m,\ a = 1\, m$
- $R_0 = 6\, m,\ a = 1.5\, m$

Explored in a range of different flat-top currents and V_{LOOP}, as it can be seen in fig. 7.1.

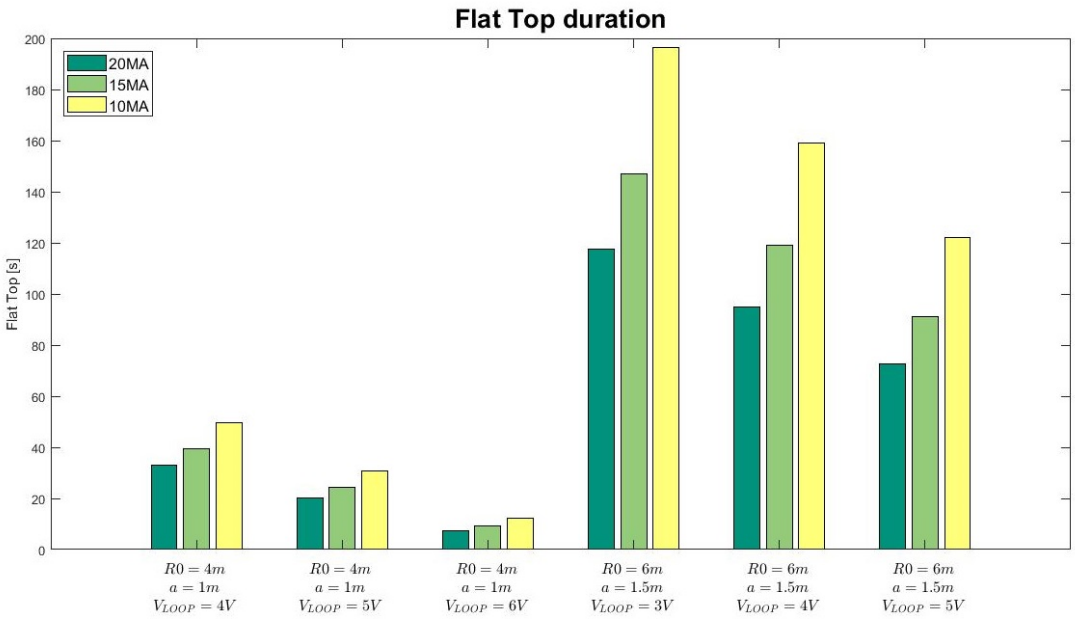

Figure 7.1: Flat top duration for all the studied cases

The flat-top duration is highly sensitive to the V_{LOOP}; hence, a crucial point in the feasibility study of RFP reactors, remains the plasma resistive voltage drop. Thus, a fundamental part in future researches should be entirely dedicated to the deepening of this parameter, as its precise knowledge is extremely important, even in early-stage designs.

Another consideration can be made on the duration of the operations. The duty cycle of such a machine should be high, hence the dwell time needs to be reduced as much as possible to guarantee a quasi-steady state operation with multiple swings. In fig. 7.2, an example of a double-swing operation is represented.

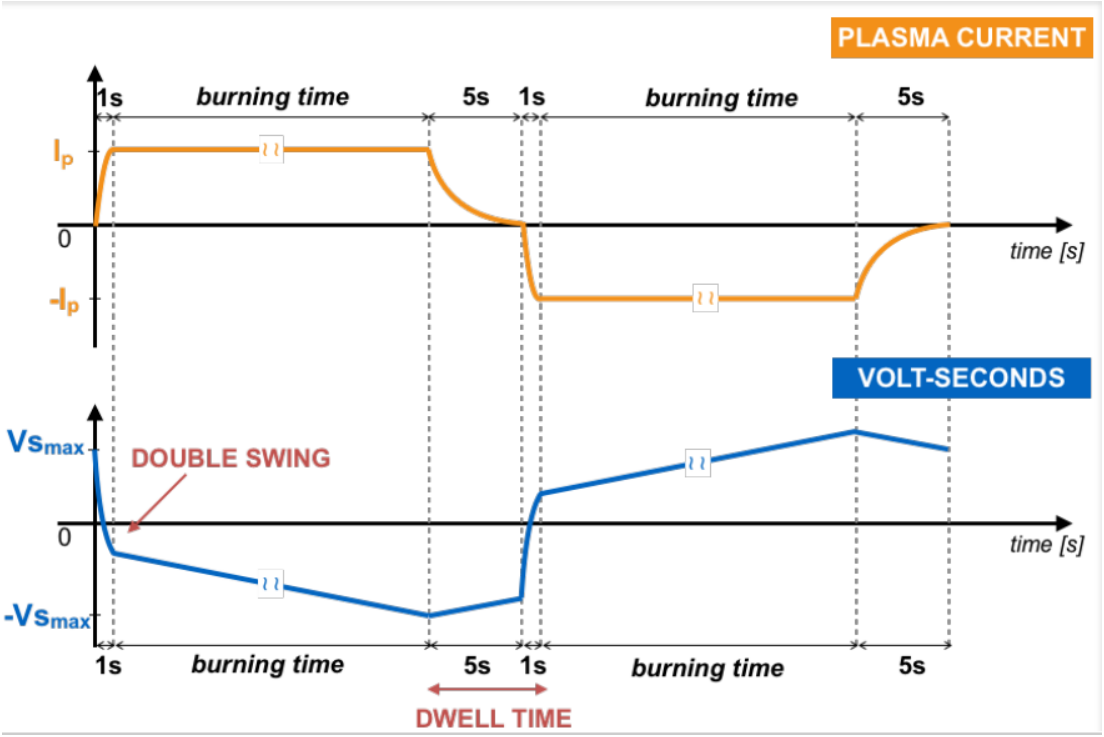

Figure 7.2: Double swing operation

In the discharged evaluated in the previous section, we can see that the available flux is consistently reduced during the ramp-down phase, even with a non-powered OH winding. To reduce the dwell time we can apply a voltage to the OH winding during the ramp-down phase. For example, with:

1. $V_{OH\,R-D} = 50\ kV$ for $R_0 = 4\ m,\ a = 1\ m$

2. $V_{OH\,R-D} = 100\ kV$ for $R_0 = 6\ m,\ a = 1.5\ m$

In fig. 7.3 and 7.4 can immediately see a consistent reduction of the dwell time, but also of the available flux.

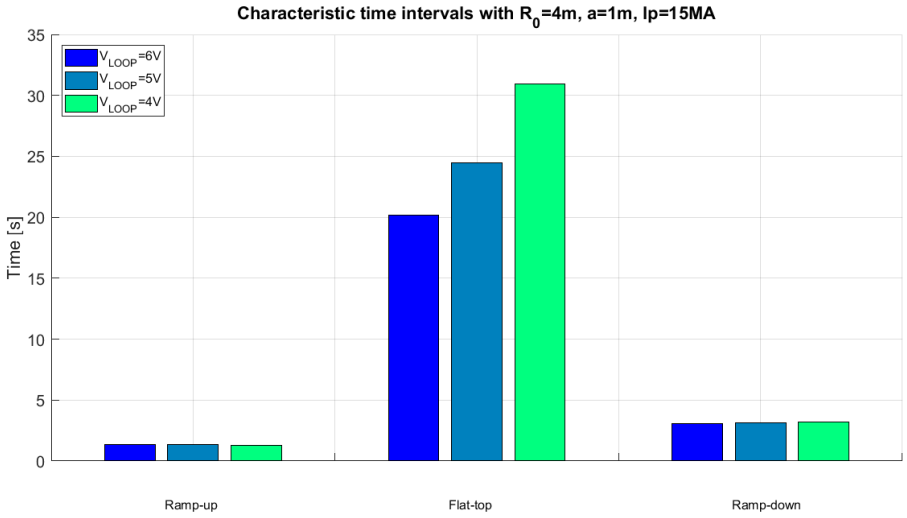

(a) Characteristic time intervals with $V_{OH\ R-D} = 50\ kV$

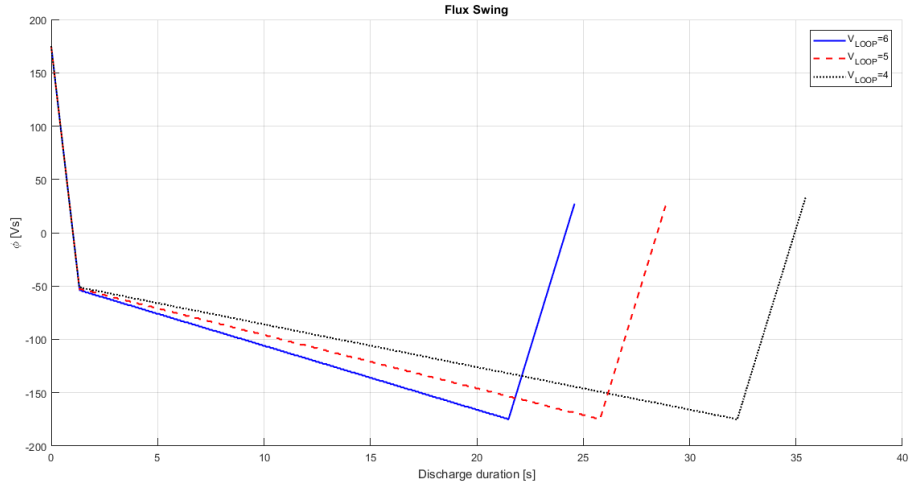

(b) Flux swing with $V_{OH\ R-D} = 50\ kV$

Figure 7.3: Reduction of the dwell time in the configuration with $R_0 = 4\ m,\ a = 1\ m$

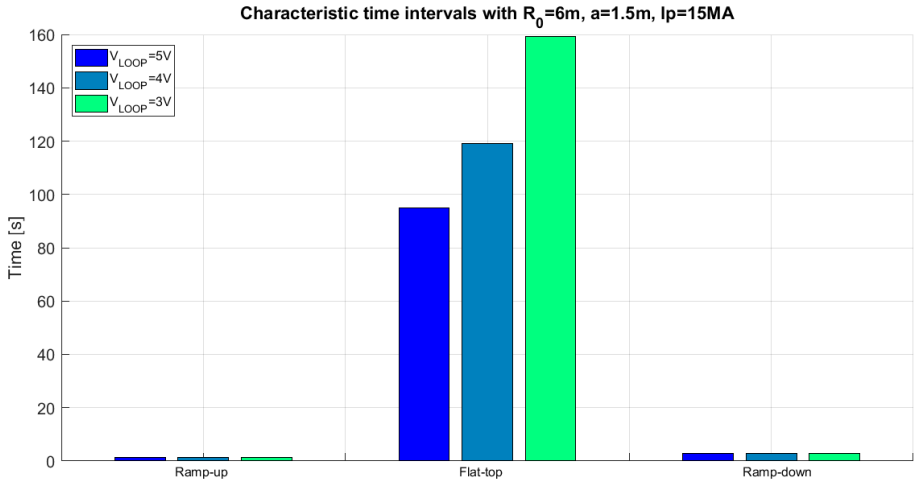

(a) Characteristic time intervals with $V_{OH\ R-D} = 100\ kV$

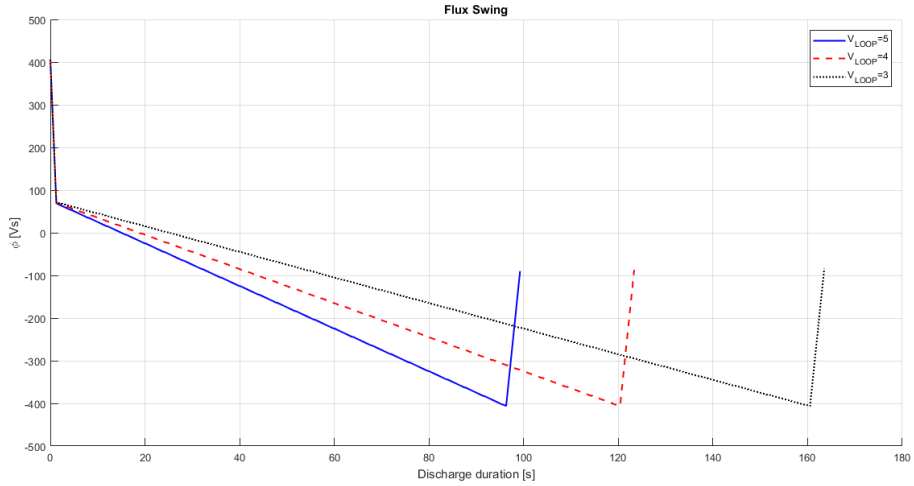

(b) Flux swing with $V_{OH\ R-D} = 100\ kV$

Figure 7.4: Reduction of the dwell time in the configuration with $R_0 = 6\ m,\ a = 1.5\ m$

As a consequence, a trade-off has to be made between the ramp-down duration and the available flux for the following discharge, if we want to achieve good performances in terms of duty cycle and number of consecutive discharges.

References

[1] R. Lorenzini, E. Martines, P. Piovesan, D. Terranova, P. Zanca, M. Zuin, A. Alfier, D. Bonfiglio, F. Bonomo, A. Canton *et al.*, "Self-organized helical equilibria as a new paradigm for ohmically heated fusion plasmas," *Nature Physics*, vol. 5, no. 8, p. 570, 2009.

[2] F. Waelbroeck, "Theory and observations of magnetic islands," *Nuclear Fusion*, vol. 49, no. 10, p. 104025, 2009.

[3] J. P. Freidberg and A. C. Kadak, "Fusion–fission hybrids revisited," *Nature Physics*, vol. 5, no. 6, pp. 370–372, 2009.

[4] J. R. Drake, J. Brzozowski, S. Mazur, and P. Nordlund, "Loop voltage and mhd activity during the start-up of an rfp," *Physica Scripta*, vol. 49, no. 2, p. 224, 1994. [Online]. Available: http://stacks.iop.org/1402-4896/49/i=2/a=015

[5] A. Stella, M. Guarnieri, F. Bellina, P. Campostrini, G. Chitarin, F. Trevisan, and P. Zaccaria, "The rfx magnet system," *Fusion Engineering and Design*, vol. 25, no. 4, pp. 373 – 399, 1995. [Online]. Available: http://www.sciencedirect.com/science/article/pii/092037969400281B

[6] F. Gnesotto, P. Sonato, W. Baker, A. Doria, F. Elio, M. Fauri, P. Fiorentin, G. Marchiori, and G. Zollino, "The plasma system of rfx," *Fusion Engineering and Design*, vol. 25, no. 4, pp. 335 – 372, 1995. [Online]. Available: http://www.sciencedirect.com/science/article/pii/092037969400280K

[7] A. Maschio, R. Piovan, I. Benfatto, P. Collarin, A. D. Lorenzi, L. Fellin, E. Gaio, J. Gray, M. Hood, and V. Toigo, "The power supply system of rfx," *Fusion Engineering and Design*, vol. 25, no. 4, pp. 401 – 424, 1995. [Online]. Available: http://www.sciencedirect.com/science/article/pii/092037969400282C

[8] J. Jin, *Electromagnetic analysis and design in magnetic resonance imaging*. CRC press, 1998, vol. 1.

[9] P. N. Swarztrauber, "On computing the points and weights for gauss–legendre quadrature," *SIAM Journal on Scientific Computing*, vol. 24, no. 3, pp. 945–954, 2003.

[10] Y. Oka and S. Koshizuka, "Conceptual design study of advanced power reactors," *Progress in Nuclear Energy*, vol. 32, no. 1-2, pp. 163–177, 1998.

[11] L. Urankar, "Vector potential and magnetic field of current-carying finite arc segment in analytical form, part ii: Thin sheet approximation," *IEEE Transactions on Magnetics*, vol. 18, no. 3, pp. 911–917, 1982.

[12] S. I. Babic and C. Akyel, "An improvement in the calculation of the magnetic field for an arbitrary geometry coil with rectangular cross section int. j. numer. model. 2005; 18 (6): 493–504," *International Journal of Numerical Modelling: Electronic Networks, Devices and Fields*, vol. 21, no. 3, pp. 220–221, 2008.

[13] S. Babic and C. Akyel, "Improvement in calculation of the self-and mutual inductance of thin-wall solenoids and disk coils," *IEEE Transactions on Magnetics*, vol. 36, no. 4, pp. 1970–1975, 2000.

[14] R. Bulirsch, "Numerical calculation of elliptic integrals and elliptic functions. iii," *Numerische Mathematik*, vol. 13, no. 4, pp. 305–315, 1969.

[15] A. Capelluto, M. Nervi, and P. Molfino, "Algorithm for the fast calculation of magnetic fields generated by arc-shaped conductors with rectangular cross section," *IEEE Transactions on Applied Superconductivity*, vol. 24, no. 6, pp. 1–5, 2014.

[16] M. Passarotto, "A volume integral formulation on polyhedral meshes for eddy current problems in fusion devices. formulazione integrale su mesh poliedriche per problemi di correnti indotte in macchine a confinamento magnetico," 2016.

[17] M. Fabbri, "Magnetic flux density and vector potential of uniform polyhedral sources," *IEEE Transactions on Magnetics*, vol. 44, no. 1, pp. 32–36, 2008.

[18] S. Liang and Y. Fang, "Analysis of inductance calculation of coaxial circular coils with rectangular cross section using inverse hyperbolic functions," *IEEE Transactions on Applied Superconductivity*, vol. 25, no. 4, pp. 1–9, 2015.

[19] S. I. Babic and C. Akyel, "New analytic-numerical solutions for the mutual inductance of two coaxial circular coils with rectangular cross section in air," *IEEE Transactions on Magnetics*, vol. 42, no. 6, pp. 1661–1669, 2006.

[20] T. Zupan, Z. Stih, and B. Trkulja, "Fast and precise method for inductance calculation of coaxial circular coils with rectangular cross section using the one-dimensional integration of elementary functions applicable to superconducting magnets," *IEEE transactions on applied superconductivity*, vol. 24, no. 2, pp. 81–89, 2014.

Ringraziamenti

Un primo sentito ringraziamento va al Professor Paolo Bettini e a Roberto Cavazzana, che mi hanno guidato nel delineare questa tesi, rendendomi pienamente partecipe nelle discussioni e fornendomi tutti i mezzi per poter apprezzare e comprendere questo settore, trasmettendomi inoltre la loro notevole dedizione e passione verso questo nobile argomento. Poi, un altro grande ringraziamento va a mia madre Donatella, a mio padre Giuliano e a mia sorella Silvia, che a modo loro e nonostante tutto hanno sempre supportato i percorsi che ho intrapreso, fornendomi i mezzi e la fiducia necessaria per mantenere la direzione scelta. Ringrazio inoltre tutta la mia famiglia, in particolare nonna Bertilla, nonno Mario, nonna Ada e nonno Alfredo, e con una lacrima dedico loro una canzone d'altri tempi, ma che Mario ha reso ben nota. Con affetto ringrazio anche tutti i coinquilini con cui abbiamo condiviso degli spezzoni di vita, qui a Padova e oltremanica; in particolare i compagni di stanza Momo, Steno e Michele. Ringrazio tutti gli amici che mi hanno aiutato a prendere consapevolezza dei percorsi e delle scelte da intraprendere, rivelandosi sempre preziosi alleati, e con i quali ho condiviso stupendi momenti che hanno plasmato l'infanzia, l'adolescenza e che stanno tuttora posando mattoni su mattoni. Ringrazio infinitamente Anna, Andrea e Lucio, quelli che per me sono i maggiori rappresentanti di Via Memmo e forse dell'intera Padova che ho vissuto in questi ultimi due anni. Un ringraziamento ai compagni di corso, ai ragazzi del team PACMAN e tutte le persone che per qualche attimo mi hanno accompagnato in questa grande esperienza. Ringrazio Rossella, che non smette mai di trasmettermi tutta la sua forza d'animo; Greta, che nonostante tutto è rimasta a vivere nella casa ai margini del bosco; Jolanda, che con la sua sensibilità e il suo affetto mi ha accompagnato in un momento complesso e cruciale della mia vita. Infine ringrazio Giacomo, che spero continuerà a dar vita a "grandi" opere culturali con me. Ringrazio chi riderà di questi ringraziamenti un po' bizzarri, ma che in fondo mi rappresentano bene e rappresentano bene le persone a cui voglio bene.